Georgi Paraskov

The influence of high speed collisions and gas flow on the formation of planetesimals

- 2006 -

Westfälische Wilhelms-Universität Münster
Institut für Planetologie

The influence of high speed collisions and gas flow on the formation of planetesimals

Inaugural-Dissertation
zur Erlangung des Doktorgrades der Naturwissenschaften
im Fachbereich Geowissenschaften
der Mathematisch-Naturwissenschaftlichen Fakultät
der Westfälischen Wilhelms-Universität Münster

vorgelegt von
Georgi Paraskov
aus Sliven
-2006-

Dekan: Prof. Dr. Hans Kerp

Erster Gutachter: Prof. Dr. Elmar Jessberger
Zweiter Gutachter: Prof. Dr. Jürgen Blum

Tag der mündlichen Prüfung: 10.11.2006
Tag der Promotion: 10.11.2006

CONTENTS

LIST OF FIGURES

CHAPTER 1

INTRODUCTION

The problem of planet formation is one of the most fundamental problems of science, and is one of the most active fields of research in astronomy, astrophysics, and planetology. In the last decade a lot of new information has been received, not only about our Solar System, but also about other stellar systems harboring extrasolar planets. Only a decade ago, in 1995 the first extrasolar planet around another star was detected (Mayor & Queloz 1995). In the meantime till today more than 190 such planets are known and their number is continuously growing (Extrasolar Planets Encyclopedia). We know now, that our Solar System is not an exception, but that planet formation takes place frequently in the universe. A closer investigation of those other planetary systems has only just begun, but the latest discoveries have already changed our view about planet formation and planetary diversity. The newly discovered planetary systems confirm some of the features predicted by standard theories of star and planet formation, but the systems with massive planets with very small orbital radii and large eccentricities, are common and were generally unexpected (Pepe et al. 2002; Da Silva et al. 2005). Although only the more massive planets can be detected at the present time it is clear that these newly-discovered stellar systems are different from our own Solar System and their discovery raises new issues about the way that our own system may have emerged.

Planet formation is strongly related to star formation. In the case of our Solar System, independent measurements of the age of the Sun and primitive meteorite show that they formed at the same time of $4.56 \cdot 10^{6}$ years ago (Lugmair & Shukolyukov 1998; Wadhwa & Russell 2000; Bonanno et al. 2002). Radioisotope dating of Moon's and Earth's rocks yields similar ages (Lee et al. 1997). All astronomical observations have shown undisputable that stars form within dense interstellar molecular clouds (Andre, Ward-Thompson, & Barsony 2000). At the beginning magnetic forces and turbulent motion lead to core formation within the cloud (Adams & Lin 1993). Under the influence of the gravitational force the cores begin to collapse. At the centre of the collapse forms a protostar. The remainder of the matter forms an accompanying circumstellar disk, surrounding the star (Adams & Lin 1993). This disk, also called "protoplanetary" disk, is considered to be the birthplace of the planets. Observations indicate that maybe half of the young stars in the universe (with ages less than 10 million years) are surrounded by dusty disks (Beckwith et al. 1990). Probably a large number of them form planetary systems. The images in Fig. 1.1 obtained in the year 1995 using the Hubble Space Telescope (HST) confirms in impressive way the existence of protoplanetary disks.

The protoplanetary disks consist up to ~99% of gas, primarily hydrogen and helium. Only about one percent of the disk mass is in dust particles. The dust material consists of surviving interstellar grains and stellar nebula condensates, and is composed mostly of the heavier elements. Astronomical observations of sun-like stars suggest that the lifetime of the disks around these objects are less than 10^{7} years (Beckwitt et al. 1990; Haisch, Lada, & Lada 2001). Therefore an upper limit for the formation of the planets is given by the disk's lifetime.

Protoplanetary Disks
Orion Nebula
HST · WFPC2

PRC95-45b · ST ScI OPO · November 20, 1995
M. J. McCaughrean (MPIA), C. R. O'Dell (Rice University), NASA
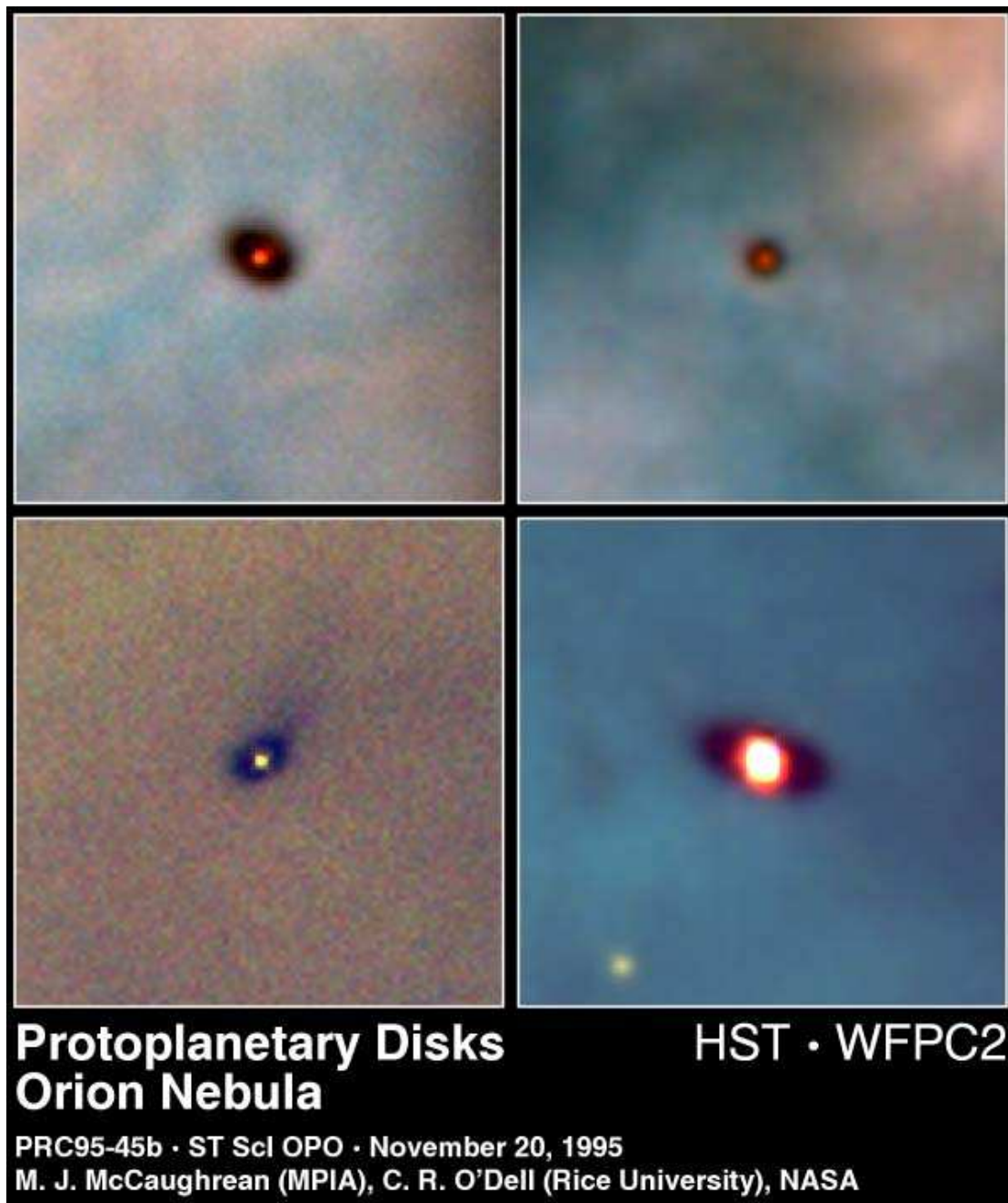
Fig. 1.1 HST images of protoplanetary disks taken towards the Orion star formation region. The silhouettes of the disks are visible due to absorption of the background light by the dust in the disks.The central bright spot (easily seen in the lower right panel) is light from the protostar leaking out through the disk. The elliptical disks with length scales of 100's to 1000's of AU will eventually trapped inside macroscopic bodies like comets and planets.

No serious model has been proposed so far for the formation of the terrestrial planets, which is not connected to protoplanetary disks. According to the "standard" model of terrestrial planet formation at the beginning dust particles collide in the disk and stick together (Dominik et al. 2006). As more and more stick together, objects several meters and kilometres across form (Beckwith, Henning, & Nakagawa 2000), but this process is uncertain. These objects, called planetesimals, are the "building

blocks" of planets. In further collisions the numerous planetesimals build a smaller number of still larger bodies, called planetary embryos (Wetherill & Stewart 1989). Eventually, a few planetary embryos will have dominated in size and accreted most of the other bodies in their regions of the disk. After all the material in those regions had been exhausted, eventually the planetary embryos collide to form planets (Kokubo & Ida 2002). Usually two regimes in this growth scenario are separated, the growth of *km*-sized planetesimals and the growth of even larger planetary embryos, which evolve into planets. The separation is based on the fact that motion and growth of objects smaller than approximately 1*km* in size are mostly determined by the interaction of these objects with the gas in the disk (Weidenschilling 1977). The sticking of the dust particles and the growth of larger aggregates in this first stage is due to interparticular surface forces (Blum 2004). Once *km*-sized planetesimals formed, the gas gets less important for the growth and the self-gravity of the bodies gets important to keep a body together.

This work focuses on the early stage of planet formation and discusses the problems of the planetesimal growth. The experiments and models described in the following chapters simulate processes, as they take place in protoplanetary disks and took place in the Solar Nebula as a precursor of our Solar System.

CHAPTER 2

DUST, GAS, AND COLLISIONAL GROWTH

2.1 The very first stage in planetesimal growth

As mentioned in the introduction it is common belief that the precursors of terrestrial planets are *km*-sized bodies, the so called planetesimals (Wetherill & Stewart 1989; Beckwith et al. 2000; Kokubo & Ida 2002). It is still an open question, how this objects form. The „standard" model of planetesimal formation is based on the mechanism of sticking collisions of small dust particles, which form larger aggregates and eventually leads to the growth of planetesimals (Weidenschilling & Cuzzi 1993; Weidenschilling 1997; Beckwith et al. 2000). Analysis of interplanetary dust particles (IDPs) and primitive meteorites suggest an initial dust grain size of 0.1-10μm (Kerridge & Chang 1993; Kerridge 1993). Therefore many numerical models and experiments on planetesimal formation start with micrometer size (Weidenschilling 2000). In the beginning these micrometer dust particles are more or less homogeneously distributed throughout the protoplanetary disk, because there is no working concentration mechanism at this time. The very first growth of larger aggregates is determined by the Brownian motion. The relative velocity between two particles is given by (Blum et al. 1996) as

$$V_B = \sqrt{\frac{8kT}{\pi\mu}} \, , \tag{2.1}$$

where k is the Boltzman constant, T is the temperature, and μ is the reduced mass of the particles. In typical numbers V_B is equal to 10mm/s in protoplanetary disks. Laboratory experiments show that at the given velocities, individual colliding particles will stick together due to the surface forces (Poppe, Blum, & Henning 2000) and form larger aggregates (Blum et al. 2000, Krause & Blum 2004, Paszun & Dominik 2006). Sticking will work up to collision velocities of about 1m/s. Because the collisions due to Brownian motion are always below this threshold, sticking will always occur. Another set of experiments shows that these aggregates continue to stick together at collision velocities up to 1m/s (Blum & Wurm 2000). Larger aggregates will form. The morphology of the growing aggregates is of prime importance for the next steps of growth. To see this, a more detailed look at the gas-grain friction time τ_f is needed. This is the timescale for a particle to react to a change in gas flow. For dust aggregates in a free molecular regime τ_f is given by (Blum et al. 1996) as

$$\tau_f = \varepsilon \, \frac{m}{\sigma_a} \, \frac{1}{\rho_g \, v_m} \, . \tag{2.2}$$

Here, m is the mass of the aggregate, σ_a is the geometrical cross section of the aggregate, ρ_g is the gas density, v_m is the mean termal velocity of the gas molecules, and $\varepsilon = 0.58$ is an empirical factor. If the gas parameters are kept constant, τ_f only depends on the mass to surface ratio of the aggregate. The question thus is, how this ratio changes as the particles grow to larger aggregate. The Cosmic Dust Aggregation Experiment (CODAG) carried out onboard the Space Shuttle in 1998 showed that

aggregation due to Brownian motion is a cluster-cluster aggregation (CCA) (Blum et al. 2000). This process is defined by two clusters of same size colliding with and sticking to each other. The CODAG experiment found that the CCA leads to growth of very fluffy almost chain-like aggregates as seen in Fig. 2.1.

Fig 2.1 *Three-dimensional reconstructions of agglomerates consisting of SiO₂ spheres with 0.95μm monomer radius. In the CODAG experiment, stereo images were obtained which allowed to reconstructing the precise agglomerate morphologies (Wurm 2003; Blum et al. 2000).*

The growth of these aggregates in many cases can be described in terms of fractal behaviour (Meakin 1991). One consequence is that mass as well as cross section scale with size by the power laws

$$m \propto R^{D_{Mf}}, \qquad (2.3)$$
$$\sigma_a \propto R^{D_{Af}}. \qquad (2.4)$$

D_{Mf} and D_{Af} are called fractal dimensions. The CODAG experiment yields for the growing aggregates $D_{Mf} = 1.3$ to 1.4 (Blum et al. 2002, Krause & Blum 2004). (Ossenkopf 1993) showed that for CCA aggregates with a $D_{Mf} \leq 2$ mass and cross section scale with approximately the same fractal dimension or $D_{Mf} = D_{Af}$. The equality between mass and cross section fractal dimensions results in an almost constant gas-grain friction time τ_f during the growth. Therefore, independent of size, the evolving aggregates always react to the gas in the same way. As far as the sedimentation of the particles to the midplane of the disk is concerned, which determines the next growth stage, the sedimentation velocity is given by

$$v_s = g_z \cdot \tau_f . \qquad (2.5)$$

If the gas-grain friction time τ_f remains constant so does the sedemintation velocity. This means that neither during the Brownian growth no afterwards significant sedimentation to the midplane occurs and the sedimentation velocities are very low. How fast the Brownian motion driven growth will proceed is still an open question,

but experiments show that it is rather rapid, compared to the timescale of planet formation (Blum et al. 2000; Krause & Blum 2004).

The significance of Brownian motion decreases with evolving aggregate size, since at constant thermal energy the random thermal velocities decrease with mass. The next stage in the planetesimal growth can be described with concentrating of dust to the midplane of the disk, as the sedimentation is the most prominent mechanism proposed for this (Lissauer 1993). During the sedimentation the dust aggregates initially collide very gently at low velocities due to statistical variations in the gas-grain coupling times which lead to differential sedimentation. They continue to form larger CCA aggregates, as seen in experiments and simulations (Dominik & Tielens 1997; Blum & Wurm 2000). The fractal dimention D_{Mf} is still smaller than 2 (Sablotny 1996; Wurm & Blum 1998). This means that the sedimentation velocities for the larger fractal aggregates are still almost as low as for the initial grains. The sedimentation velocities depend on the individual friction times, but a typical number for aggregates of 1*mm* in size and smaller is 0.1*mm/s* (Blum & Wurm 2000).

As the aggregates grow larger, their mass increases. The higher mass is accompanied by a higher energy in a collision. Dominik & Tielens (1997) and Blum & Wurm (2000) showed that above certain impact energy deformations and relocations of individual grains in the aggregates are possible due to rolling or sliding of the constituents. The aggregates get more compact and the mass to surface ratio increases with size. This further means that they sediment faster, can pick up smaller particles, grow larger and get even faster (Weidenschilling & Cuzzi 1993). So eventually, at sizes of some *cm*, the rainout and the concentration of dust in the midplane of the disk is guaranteed. Over the last decade a number of experiments have been carried out to verify the growth of *cm* dust bodies (Wurm & Blum 1998; Blum & Wurm 2000; Blum et al. 2000). They show that this process in general can be understood in terms of the binary collision model. This was also found to be in agreement with theoretical studies of collisions of dust aggregates (Dominik & Tielens 1997; Kempf, Pfalzner, & Henning 1999). The numerical calculations carried out by (Nakagawa et al. 1981) showed that in the Earth zone, a thin dust layer composed of *cm*-sized grains is formed in about 3 x 10^3 years after the beginning of sedimentation. (Weidenschiling 1980) obtained similar results concerning the duration of the sedimentation stage.

2.2 Collisional growth in the midplane

After 10^3 years of sedimentation the amount of dust in the midplane of the disk is sufficient to provide in the next few million years the growth of *m* and *km* dusty bodies – the planetesimals. In the past, gravitational instability of the dense dust layer in the midplane of the disk has been the paradigm of their formation (Goldreich & Ward 1973). The idea is that after particles concentrate in the midplane to a critical density, part of the dust sub-disk gets gravitational instable and collapses. Problems came up with this idea, as it became clear that the shear between the dense sub-disk and the less dense upper layers would generate turbulence, which would not allow the critical density to be reached (Weidenschilling, Donn, & Meakin 1989). There is ongoing work with respect to this branch of the problem (Youdin & Shu 2002). Youdin and Shu (2002) suggested that under certain conditions instability might be possible but only after several million years. While this might be just in time before disks on average dissolve, gravitational conditions might not be reachable in time if conditions are less perfect than assumed (Haisch, Lada, & Lada 2001; Garaud & Lin

2004). Another more recent idea is that eddies, which might develop in protoplanetary disks, might collect small bodies in their center, which might then grow to planetesimals or larger (Klahr & Bodenheimer 2003). It has to be waited for if more detailed versions of this model might explain the formation of the planetesimals.

However, probably the idea that is currently favoured most for planetesimal formation is based again on the mechanism of sticking collisions of the smaller bodies in the midplane of the disk. Once particles reach the midplane, other mechanisms than differential sedimentation for generating relative velocities and therefore collisions get important. Because the gas disk is pressure gradient supported and rotates slower than Kepplerian, the dust bodies moving on a Kepplerian orbit are subject to a gas drag. The gas drag is based on the individual friction times of the particles and aggregates, and leads to different radial and transversal velocities. These two velocity components for particles of different size are shown in Fig. 2.2.

The difference in the relative velocities results in high collision velocities for particles of different size. For example, a body of $1m$ might collide with smaller bodies, which move with the gas, at velocities of $50\text{-}60m/s$ (Weidenschilling & Cuzzi 1993; Sekiya & Takeda 2003).
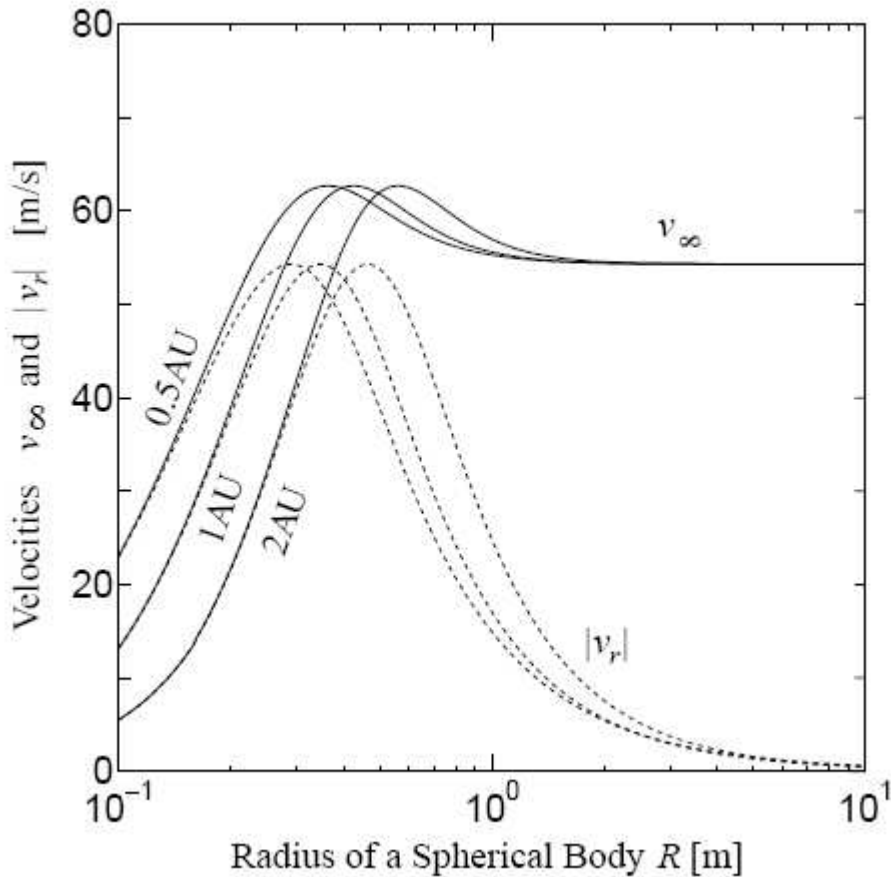
Fig. 2.2 *The velocity of a solid sphere with radius R for r = 0.5, 1, and 2AU. The solid curves show the absolute value of the velocity relative to the gas, v_∞, and the dashed curves show the radial infall velocity toward the sun, $|v_r|$. Taken from (Sekiya & Takeda 2003).*

So far impact experiments on *mm*-or smaller sized dust aggregates only

resulted in fragmentation at impact velocities higher than a few *m/s* (Blum & Münch 1993; Blum & Wurm 2000). In addition impact experiments have been carried out with *cm*-sized ice pendulums. Collisions result in sticking only below *cm/s* collision velocity (Supulver et al. 1997). Impacts of *cm*-sized marbles into regolith yield threshold velocities for sticking up to 20*cm/s* (Colwell 2003). The presence of organic material in the aggregates might increase the sticking probability, for example for *mm* particles up to 5*m/s* (Kouchi et al. 2002), but the growth of larger particles at even higher velocities can not be explained by this. In all past experiments not a single collision between two bodies at typical collision velocities in protoplanetary disks above 10*m/s* has ever resulted in sticking or growth of a larger body. Therefore, it has been an open question, if a mechanism exists, by which high speed collisions can lead to a net growth, and which will corroborate the collisional growth theory.

One of the most significant parameter, which determines the outcome of a collision between two bodies, is their structure. Many experiments were carried out so far with compact projectiles (impacting body) - steel balls, regolith, etc. Relating to planetesimal growth, this does not correspond to the logical growth sequence. The first formed *cm*-sizes bodies are namely very porous fluffy dust aggregates, which hold together only by the surface forces between the single *μm*-sized dust particles. In this manner it is more significant to carry out collision experiments with similar aggregates. In addition, also it is very important to carry out the impact experiments at the expected high velocities. The experimental results reported in the literature so far are not applicable to larger bodies consisting of strongly cohesive dust colliding at high velocities. We therefore carried out experiments with centimetre-sized porous projectiles impacting at high velocity a very porous centimetre-sized target, where both bodies are agglomerates of *μm*-sized dust particles. The experiments and the results are described in detail in Chapter 3 of this work (Section 3.2).

However, this might not be the only scenario for collisions between pre-planetesimals. It cannot be decided yet how the larger bodies really evolve self consistently after many collisions. It is possible that impacts lead to a more compact body on average. Therefore, a question worth asking is what happens in a collision between a projectile and a target where the dust sample is packed rather densely. In Chapter 3 (Section 3.3) we try to answer this question, as we present another series of experiments with more compact dust aggregates.

2.3 Gas flow and planetesimal growth

In recent experiments Wurm, Blum, & Colwell (2001a, 2001b) showed that the result of a collision, which is initially eroding, can still lead to net growth if the gas in the protoplanetary disk and its motion relative to the colliding bodies is considered. The underlying mechanism is based on the gas drag agin. The larger of two colliding bodies in a protoplanetary disk, which moves on a Kepplerian orbit faster than the gas, is experiencing a head wind. The smaller body on the other hand couples very well to the gas and follows its motion. Entrained in this head wind the smaller body collides with the larger one. If the collision between both bodies result in erosion and fragments are ejected from the impact place, the head wind can return the fragments to the large body under certain conditions. For that purpose the fragments must be small enough to couple well to the gas, and slow enough not to be carried away too far. Then the particles (fragments) collide a second time with the surface of the larger body, and this time the collision velocity is much lower. At this low velocity the particles stick to the larger body due to surface forces. If these secondary collisions

return more material to the large body than was eroded by the primary collision, net growth results. The idea of this mechanism is illustrated in Fig. 2.3.
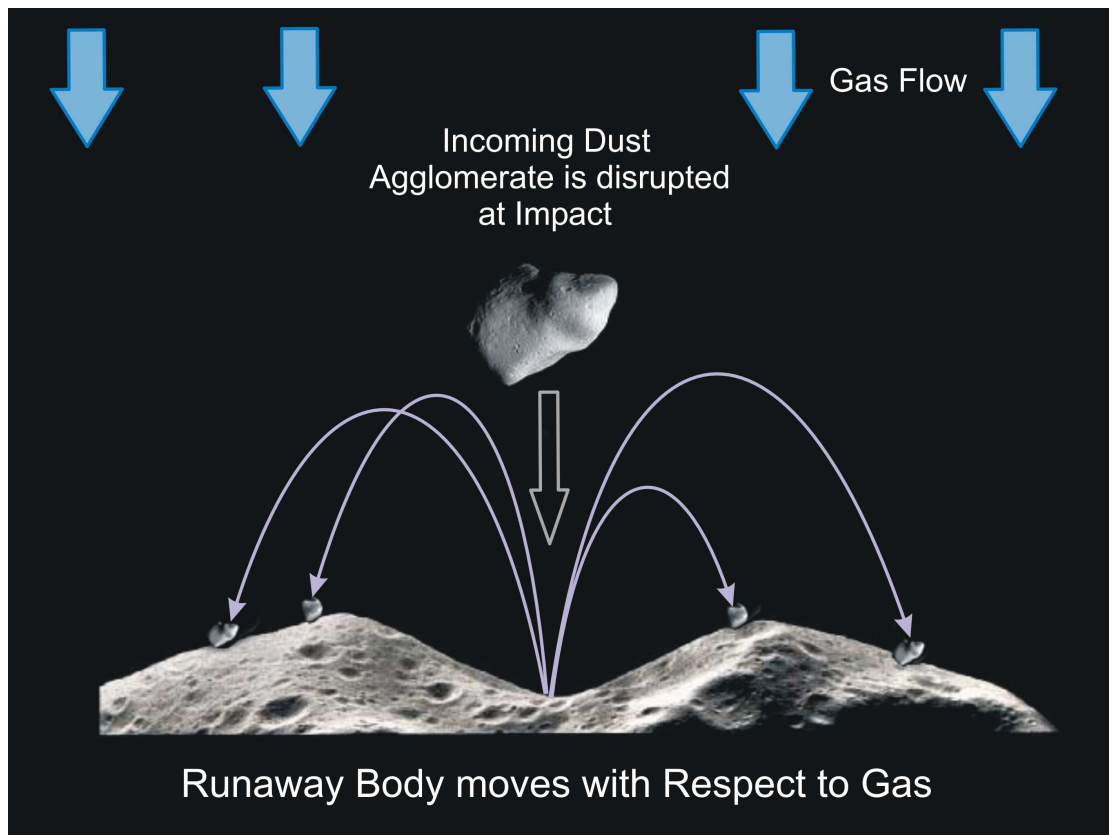
Fig. 2.3 *Net growth by secondary collisions induced by a head wind. Taken from (Wurm 2003). A target eroded by an impacting projectile can reaccrete ejecta if the collision takes place in a gas flow. The secondary, slower collisions of fragments can add mass again and eventually lead to net growth. The efficiency of this mechanism depends on the porosity of the body, the gas parameters, and the size and velocity of the ejected particles (fragments).*

Experiments prove this mechanism to work (Wurm, Blum & Colwell 2001a, 2001b). If small CCA aggregates, embedded in a gas beam, collide with a target up to velocities of 12*m/s*, they fragment into the constituents – individual *μm*-sized grains. These grains can return to the target as seen in Fig. 2.4.

The threshold velocity for reaccretion depends on the Knudsen number, which is given as

$$Kn = \frac{\lambda}{r_p}, \qquad (2.6)$$

where λ is the mean free path length of the gas molecules and r_p is the radius of the target body.
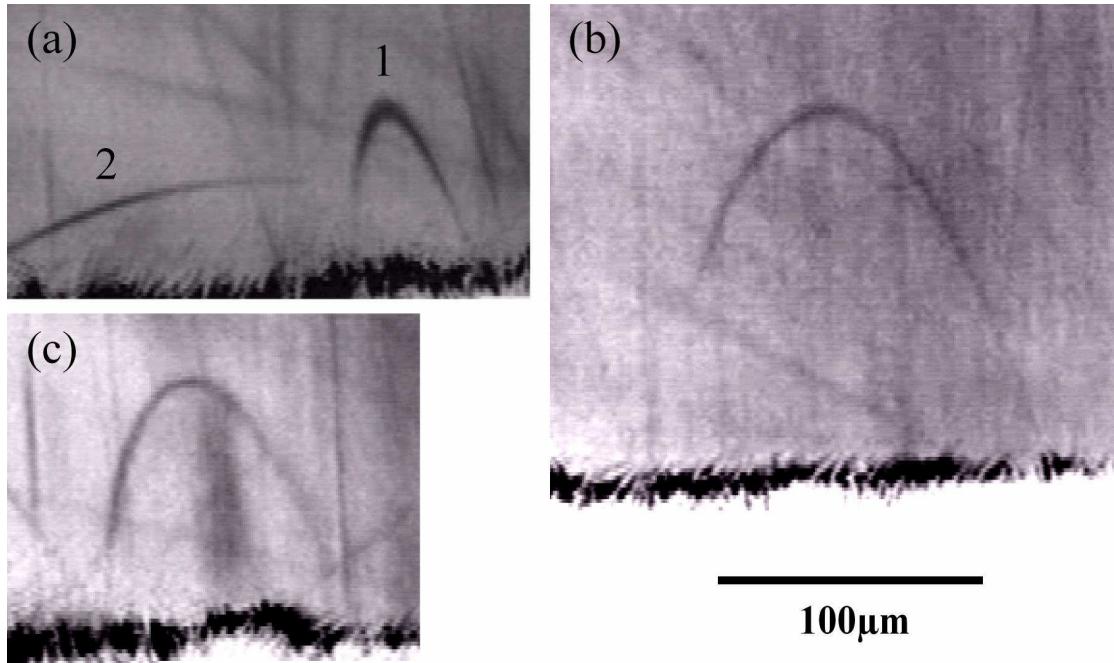
Fig. 2.4 *Trajectories of dust grains bouncing of a target as fragments of a collision but being bend back to the target by the gas flow (Wurm, Blum & Colwell 2001b).*

The experiments (Wurm, Blum & Colwell 2001a, 2001b) did not provide the lowest Knudsen number to which this growth mechanism might work. Thus far, the experiment conditions have considered the free molecular flow regime, in which the gas flow is essentially undisturbed by the larger body (target) and flow lines end straight on the target surface. This changes once the body has grown sufficiently and continuum flow takes over from free molecular flow. Streamlines are then surrounding the body, and fragments entrained in the gas flow might be carried away rather than being returned to the target after a collision. This situation has been analyzed in a paper by Sekiya & Takeda (2003). They considered the gas flow in more detail and came to the result that in the inner region of protoplanetary disks (< 5*AU*) this mechanism of gas aided growth might work for solid (non porous) bodies of a few *m* in size. They conclude that a change in the gas flow regime from free molecular to continuum flow then leads to transport of fragments around a body rather than back to its surface. While this is true for a solid non-porous body we will show in Chapter 4 of this work that even in continuum regime reaccretion of fragments can still occur if the eroded body is highly porous (Wurm, Paraskov, & Krauss 2004).

2.4 Erosional potential of the gas flow

We discussed in the previous sections that the growth in sticking collisions is widely regarded as the fundamental process to form *km*-size planetesimals. Even though the growth model is not without problems, experiments and simulation, given below, show that under many circumstances the model can probably work. The current view is that on a rather short timescale of 10^4 years after begin of the sedimentation larger planetesimals of *km* or more in size might form (Hayashi, Nakazawa, & Nakagawa 1993). As the planetesimals have grown, the further growth is more and more determined by self-gravity of the bodies.

Even if self gravity gets important and even if gas drag no longer dominates the dynamics of planetesimals, these objects still move through the gas. This sets the stage for a large number of basic problems. On one hand, we have seen in the previous section that the gas drag in the protoplanetary disks might promote the planetesimal growth. On the other hand, if the gas flow is strong enough to be considered an effective force on dust particles, it might be asked if gas drag could also destroy larger objects. If a dusty body moves through the gas, the gas imposes a shear force on the top layers of the dust. If this force is larger than the cohesive force (and gravity) particles will be removed and the body loses mass merely by moving through the gas disk. The effect might roughly be compared to eolian erosion on Earth or Mars. The pressure at the surface of Mars e.g. is less than 10mbar. Dense models of protoplanetary disks have comparable inner gas pressures (Wood 2000). Wind speeds to start erosion on Mars can be as low as 20m/s (Greeley et al. 1980). Headwind velocities of small bodies moving on circular orbits in protoplanetary disks are ~60m/s (Sekiya & Takeda 2003; Weidenschilling & Cuzzi 1993). This comparison shows that conditions in protoplanetary disks are similar to threshold conditions for erosion on Mars and should be considered in more detail.

The possibility of gas erosion is even more likely, if eccentric orbits are considered. Close encounters with larger protoplanets can stir the planetesimals up to eccentric orbits (Hood 1998). For these objects the relative velocities with the gas might strongly increase and easily get supersonic then which leads to bow shocks in front of the planetesimals (Hood 1998). At pericenter the difference in velocity between a body moving on an eccentric orbit with v_{per} and eccentricity e compared to a circular orbit v_{circ} is (Murray & Dermott 1999)

$$ v_{per} - v_{circ} = v_{circ}\left(\sqrt{\frac{1+e}{1-e}} - 1 \right). \qquad (2.7) $$

This assumes that both bodies move with the same mean motion (average angular velocity). It is interesting to note that Earth with an eccentricity of only $e = 0.017$ would move at about 500m/s relative to the gas at perihelion. Then for a planetesimal with even a small eccentricity, relative velocities from 500m/s or more can be expected. Gas flow relative to the moving solid is faster in that case and the shear forces at the surface are stronger. In addition on a very eccentric orbit the dusty body traverses the inner dense part of the disk, where the gas pressure and respectively the erosion potential are sufficiently higher.

In contrast to Mars and Earth material lifted from a planetesimal does not return and is lost for the planetesimal. If planetesimals are loose aggregates of dust and if eolian erosion is a significant process, it eventually destroys planetesimals. It is also worth noting that the erosion of a large object might bring older material back to the disk. This old material can then be mixed more homogeneously with younger solids. It has recently been discussed by Krauss & Wurm (2005) and Wurm & Krauss (2006) that photophoresis can concentrate solids in belts around young stars. Eolian erosion might be one way of providing material for such redistribution at later times. It might thus be important for the formation of comets, Kuiper belt objects, and primitive asteroids.

In order to study the interaction between gas flow and dust bodies, and the erosion potential of the flow we carried out a series of wind tunnel experiments. In addition we simulated the same processes numerically (Paraskov et al. 2006). The

results from the laboratory experiments, the numerical calculations, and the importance of planetesimal eccentricities for the planet formation are discussed in Chapter 5.

CHAPTER 3

IMPACT EXPERIMENTS

We carried out impact experiments with cm-sized porous dust aggregates consisting of µm-sized dust particles and impacting with velocities up to 38*m/s*. The purpose was to study the outcome of a collision and the interaction between projectile, target, and ejecta under conditions simulating protoplanetary disks. Impacts of cm-sized dusty bodies at several tens of *m/s* are supposed to be typical in the early phase of planet formation, as outlined in Chapter 2. Therefore our results are directly applicable to the process of planetesimal formation.

We study two different kinds of targets in collisions: highly porous and highly compact dust aggregates, as extreme candidates for collisions. In Section 3.2 of this Chapter we describe the results of a set of impact experiments with the highly porous targets (up to 88% porosity). As porosity we define:

$$P = \frac{V_{void}}{V_{total}}, \quad (3.1)$$

where V_{void} is the volume of the void space within the target not occupied by dust and V_{total} is the total volume of the target (target tray). The void space V_{void} is $V_{total} - V_{dust}$, where V_{dust} is the volume filled by solid material. The dust aggregates that we use have a very fluffy structure and might resemble the *cm*-sized dust bodies in the protoplanetary disks during the early collision phases.

Because we can not decide yet how the larger bodies really evolve after many collisions, we are ready to suppose that the impacts lead to a more compact body on average. Therefore we carried out a second set of experiments with highly compact targets, where the dust sample was packed rather densely. The porosity of the aggregates was still 65.7%, and this, as will be later explaned, is a limit at least as static compression is concerned. The results are reported in Section 3.3.

3.1 Experiment description

3.1.1 Experimental set-up

The experimental set-up, as seen in Fig. 3.1, was specially developed for these experiments. The set-up is composed of three principal segments – a circular closed wind tunnel, an impact chamber (part of the tunnel) and a roots pump. The gas flow of the wind tunnel was used only rudimentary so far for the experiments reported in this chapter. I will therefore only describe the impact part of the setup here. The impact takes place in the impact chamber (32*cm* in diameter). The chamber is evacuated prior to the impact to a pressure below 0.01*mbar*. The low gas pressure results in high friction times for the dust projectile, so that the gas in the chamber does not influence the impacts. A schematic sketch of the experiments is shown in Fig. 3.2. The target is an aluminum tray with 6*cm* diameter and 5*cm* depth filled with dust and centered in the middle of the chamber. In accordance with the aim of the experiment we used two types of targets. Details of the target preparation will be given later.

Fig. 3.1 *Photo of the experimental set-up. The set-up is composed of a wind tunnel, an impact chamber (front right), and a roots pump (back). The tunnel is circular closed and has an inside diameter from 32cm. It is 200cm high and 150cm wide. The vacuum chamber, where the experiments take place, is part of the tunnel and has flanges for observation and measuring instruments. The roots pump is used to produce gas flow (see Chapter 5). The maximum wind speed can range up to 100m/s. A vacuum pump is used to evacuate the tunnel. The pressure can be adjusted from about 10^{-3}mbar to 10mbar.*

As projectile we used the same dust as in the target filled in a cylindrical holder turned upside down. An aluminum foil was used to prevent the dust from falling out while hanging upside down. The foil only compensates the weight of the dust but easily bends during launch, allowing the projectile to pass. We developed two types of launchers. At the beginning we used pressurized air to accelerate the projectile holder (and the projectile within). It proved too leaky though resulting in a rather high increase in gas pressure within the vacuum chamber. The dust projectile in this case would not move undisturbed by the gas. If the sealing was improved, the holder got stuck. No measurements were taken with this launcher. Because the increase in pressure influenced the experimental procedure negatively, we developed a second

17

launcher, based on a compressed spring that launched the projectile holder.
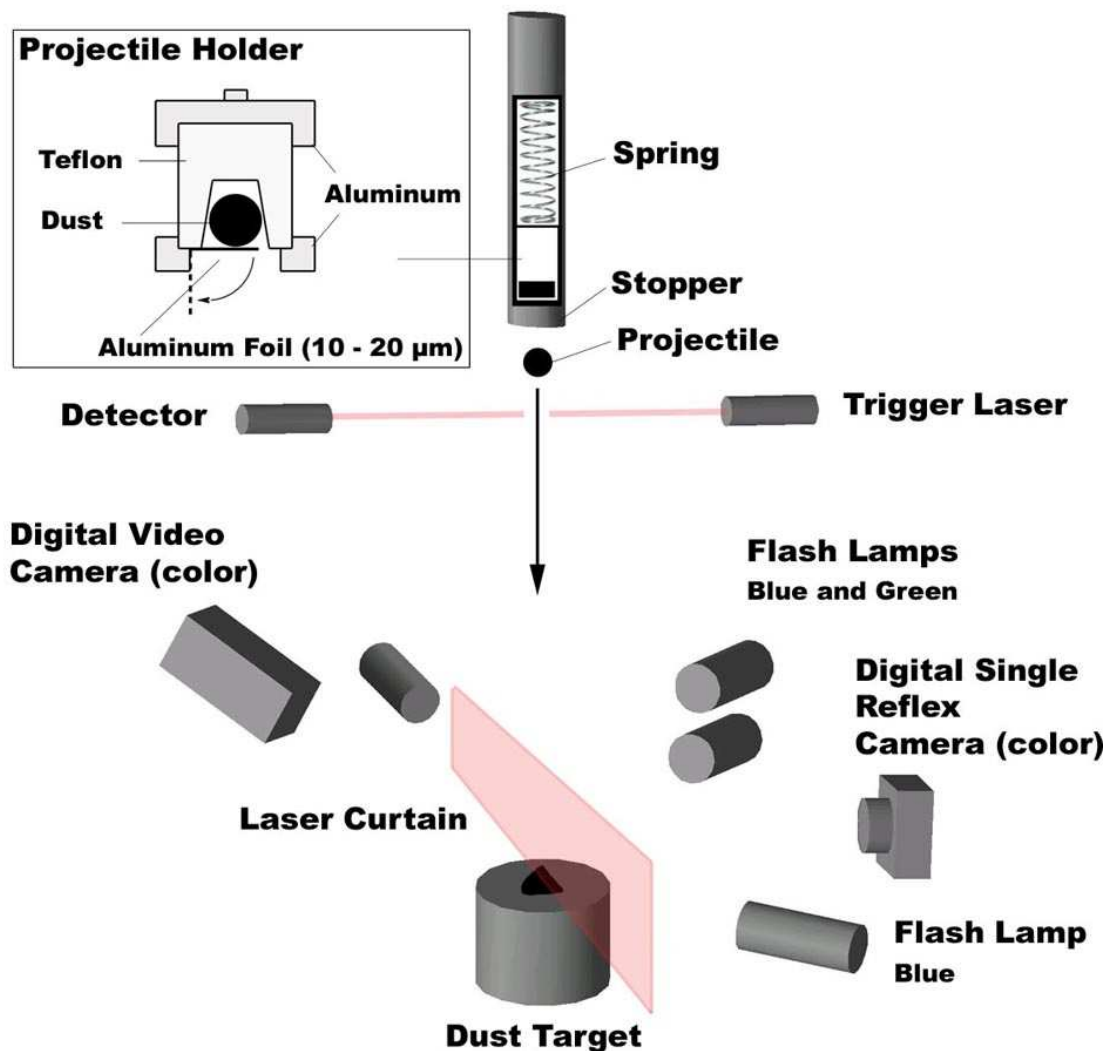
Fig. 3.2 *Sketch of the experiment taken from (Wurm, Paraskov, & Krauss 2005). A dust projectile is launched onto a dust target after its holder is abruptly stopped. The holder itself is accelerated by a spring. An aluminum foil of only 10–20µm thickness is fixed on one side of the bottom of the holder. It prevents the dust from falling out while hanging upside down. It essentially covers the whole opening but easily bends inelastically at its fixation point under a load slightly exceeding the weight of the dust projectile. Thus it is easily pushed out of the way by the dust projectile during launch. The load applied to the dust projectile by the foil is insignificant and has no influence on the launched projectile. A light barrier triggers a sequence of flashes in different colors, which result in one frame of the single reflex camera containing information of different times before and during the impact. The images are in reflected light. In addition, a laser curtain in the focal plane of the single reflex camera gives information on slower particles in a thin sheet. The aperture of the digital single reflex camera is open for several seconds. The digital video camera is running at a standard frame rate. The dust target is weighed before and after an impact. All experiments are carried out under vacuum.*

To launch the projectile the holder is pulled upwards by a chain drive against the force of the spring with an electric motor. The projectile holder is connected to the chain drive by a rated break point. Once the spring is fully compressed further pull will lead to a force exceeding the force tolerated by the contact and the contact will break. The projectile is then accelerated by the spring. With this launcher we reached impact velocities up to 38*m/s*. But this launcher had other disadvantages. On the one hand the chain drive was not stable enough and cracked many times during the experiments. On the other hand, with the chain we could not vary the launch velocities. Also the timing for launch was very variable. Therefore we used this launcher only for the first series of experiments. Later we exchanged the chain drive with a string drive. The spring was pulled upwards by a string with electric motor or manually. Once the spring is compressed to the wanted tension, a switchblade cuts the string and the projectile holder (and the projectile within) is accelerated by the spring. The projectile holder moves within a guide tube to approximately 15*cm* above the target. A stopper at its end abruptly decelerates the holder. Due to inertia, the dust moves on through the central hole of the stopper. Thus a dust projectile is launched at the dust target. The impact is imaged by a digital color single reflex camera and a digital video camera. Light for the cameras is provided by three flash lamps in two colors (blue and green). Different positions of the light sources have been used during the experiments. A red laser was used to provide a laser sheet perpendicular to the target.

3.1.2 Dust

As dust sample we used a commercial SiO_2 powder with a broad size distribution.
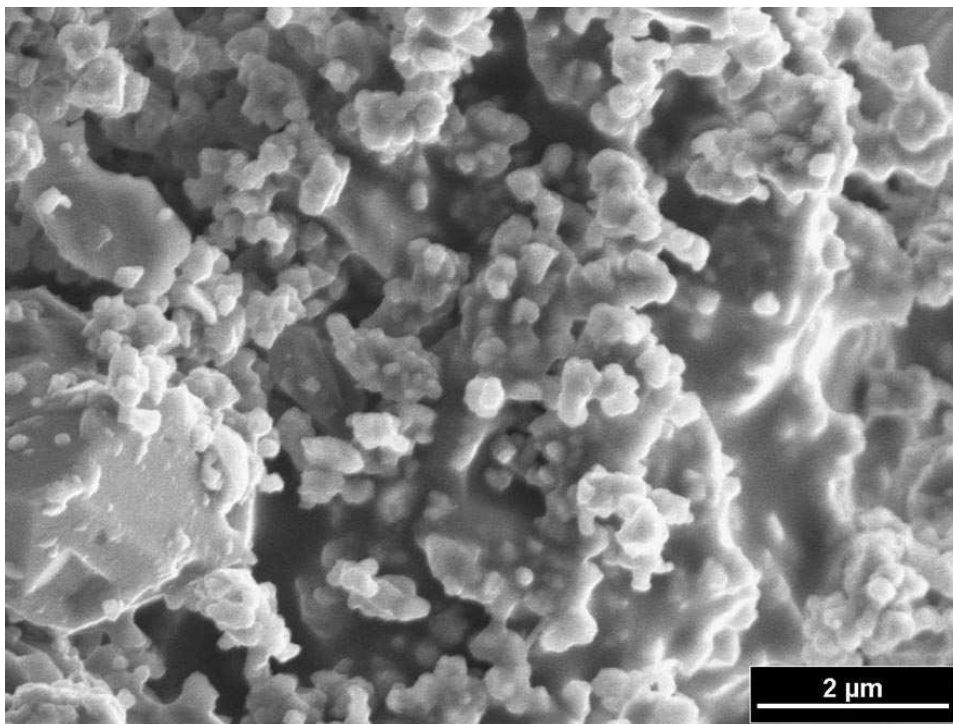
Fig. 3.3 *Scanning electron microscope (SEM) image of the SiO_2 dust particles. The dust sample that we used throughout all experiments is a mixture of particles with broad size distribution (0.1-10μm).*

Particle sizes are between $0.1\mu m$ and $10\mu m$ with 80% of the particle mass within particles of $1\mu m$ to $5\mu m$ in size (specification by manufacturer). The particles have irregular shapes. The density of the bulk material is $2.6g/cm^3$. A scanning electron microscopy image of the dust is shown in Fig. 3.3. Earlier experiments showed that the chemical composition of the material is probably of minor importance for sticking of dust particles at least as similar materials like silicates are considered (Blum & Wurm 2000). Thus we regard our dust as one possible analog material to model the larger fraction of particles in protoplanetary disks and the solar nebula.

3.1.3 Projectile

For most experiments we used slightly cone shaped Teflon reservoirs, which we filled with dust (Fig. 3.4). The reservoir has an $8mm$ diameter opening on the bottom (open end), a $7mm$ diameter at the top, and a length of $10mm$. The projectile was prepared in several ways. For some experiments we filled the reservoir with dust compacted manually. This dust usually does not leave the holder as one unit but breaks up into a large number of smaller dust clumps. We also inserted dust projectiles into the holder, which were compacted outside the holder and inserted without force. This reduced the sticking of dust to the Teflon so that the dust gets out easier. Friction is less likely to disrupt the projectile mass and less mass is left within the holder after the experiment.
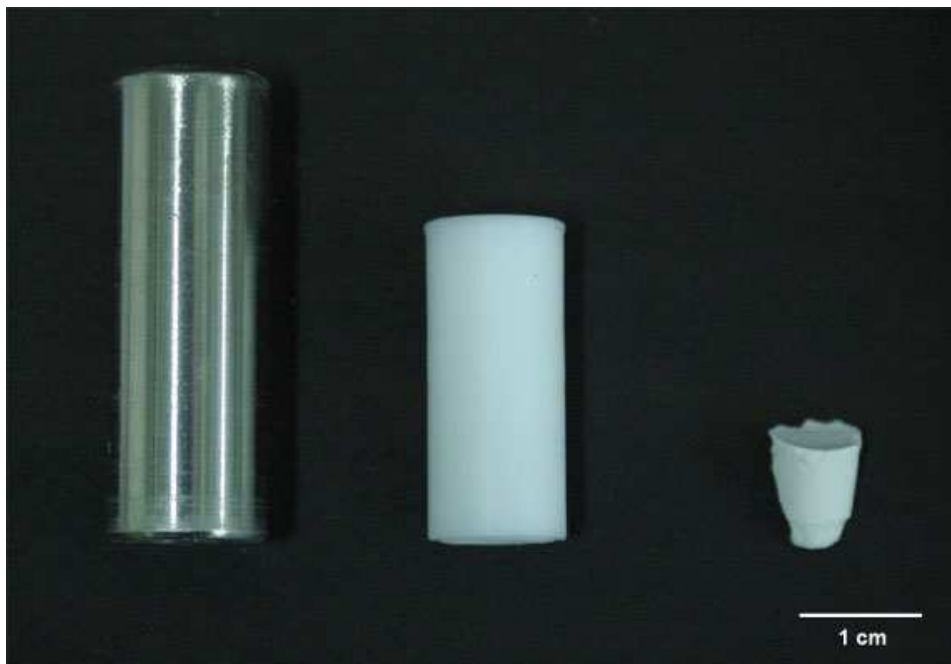
Fig. 3.4 Metal and Teflon reservoirs, and dust projectile. In our first experiments we used metal holders. To reduce the friction and to reach higher launch velocities we used Teflon holders later. The projectile is a compact dust aggregate, approximately 5-10mm in size.

Due to the uneven acceleration by the spring and friction while it leaves the holder the projectile might break up. A small cloud of smaller fragments as seen in Fig. 3.5 accompanies usually one large dominant fragment during the flight. Since the extend of the dominant fragment is comparable to the original projectile size we assume that the launch and a small degree of fragmentation is not important for the impact. It has

to be noted though that the impacts are individual events with slightly different sized and different shaped dust aggregate projectiles of a typical size of 5-10*mm*, weights of about 0.2 *g* and an initial porosity of 66% ± 2%. The original projectile and the holders can be seen in Fig. 3.4. A projectile during the flight is shown in Fig. 3.5.

3.1.4 General description of the experiments

In general an individual experiment might be described as follows: A target, which has been under predefined low humidity conditions for a few hours, is weighed and then placed into the vacuum chamber. The chamber is slowly evacuated to a pressure on the order of $p < 0.01mbar$. A weighed projectile is launched as described above to the center of the target. A few *cm* above the target the projectile passes a light barrier and triggers a sequence of colored flashes. The camera is directed horizontally to the target surface and is operated in long duration exposure mode (4 seconds open aperture) so that just one color frame is taken for each impact. During this time the flash lamps light up at different times.
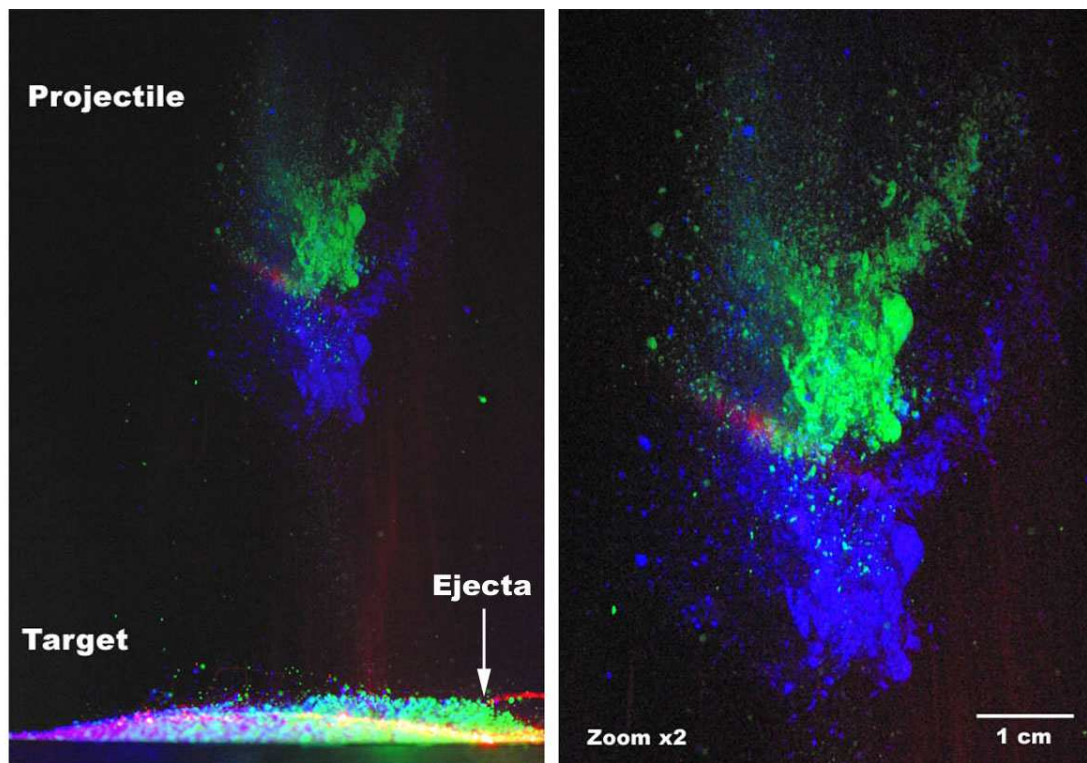
Fig. 3.5 Impact imaging. Projectile and target in reflected light. Together with the trigger the green flash lamp is firing once. This results in an image of the incoming projectile in reflected light at a certain distance (5cm) above the target. At a time 0.5ms after trigger the blue flash lamp is firing. This results in a second image of the incoming projectile. 18ms and 20ms after the trigger the flash lamps are firing again in green and blue. This results in two images of ejected fragments from the target surface. Due to the color separation different information can be extracted from the image. The first two flashes for example reveal the size and shape of the incoming projectile, and its velocity. The next two flashes give more information about the consequences of the impact, the ejected material, their flight directions and velocities.

The impact itself elapses in a few milliseconds. In total a sequence of four flashes (in blue and green) is used to illuminate the projectile and target, which are imaged on the same frame. Thus a single color frame of the camera is used as high-speed photography. We extract different images corresponding to different times from the different color channels of this one frame. Due to the color separation, different information can be obtained, for example the projectile impact velocity, the fragment velocity, the size and the shape of the projectile and the ejecta. A typical example can be seen in Fig. 3.5. Sometimes the projectiles look rather diffuse in reflected light. The impact is also recorded with a video camera that uses the green flash for bright field illumination. The video camera reveals an optically thick projectile, though sometimes with a diffuse rim (Fig. 3.10). Probably a rim of small dust particles leads to self-shadowing in reflected light. In addition a red laser sheet is used to image the trajectories of fragments in a fixed plane perpendicular to the target. After an impact the chamber is slowly filled with air again. The target is weighed a second time, after spending a few hours under the same low humidity conditions as before the experiment.

The experiments carried out so far can be divided in 2 classes. Both groups differ from each other only in the target type. The next section presents the results from a series of experiments with very porous dust targets. Section 3.3 describes experiments with more compact targets.

3.2 Experiments with porous dust targets

3.2.1 Target

The target is an aluminum tray with $6cm$ diameter and $5cm$ depth filled with dust. The dust sample is sieved into the target tray to get a highly porous target. For most experiments we used a mesh with $0.5mm$ openings for sieving. In this case the surface is consisting of individual dust clumps up to $0.5mm$ in size, which can be rather compact, but loosely stick to other dust clumps.

Fig. 3.6 *Porous target. A porous target prepared by sieving powder with a 0.5mm mesh. The sieving results in a granular structure of the surface. The individual grains are up to 0.5mm in size.*

A target image can be seen in Fig. 3.6. The granular morphology of the surface due to the sieving is clearly visible. For some experiments we also used meshes with 0.09mm and 0.025mm openings. This corresponded to smaller dust granules.

The target porosities varied between $P = 74\%$ and $P = 88\%$. With the dust mass measured and with the bulk density of the dust known ($2.6g/cm^3$) V_{dust} can be determined according to equation 3.1 and thus the porosity is given. Individual errors are typically $\pm$ 0.5% resulting from the determination of the average height of the target.

In some experiments the impact leads to a collapse of the target of a few mm over the whole width of the target. In this work, in analogy to geology, this collapse will be called – surface subsidence. The surface subsidence can be attributed to the vibrations (elastic waves) during the impact that are sufficient to compact the highly porous target slightly after the impact in combination with gravity.
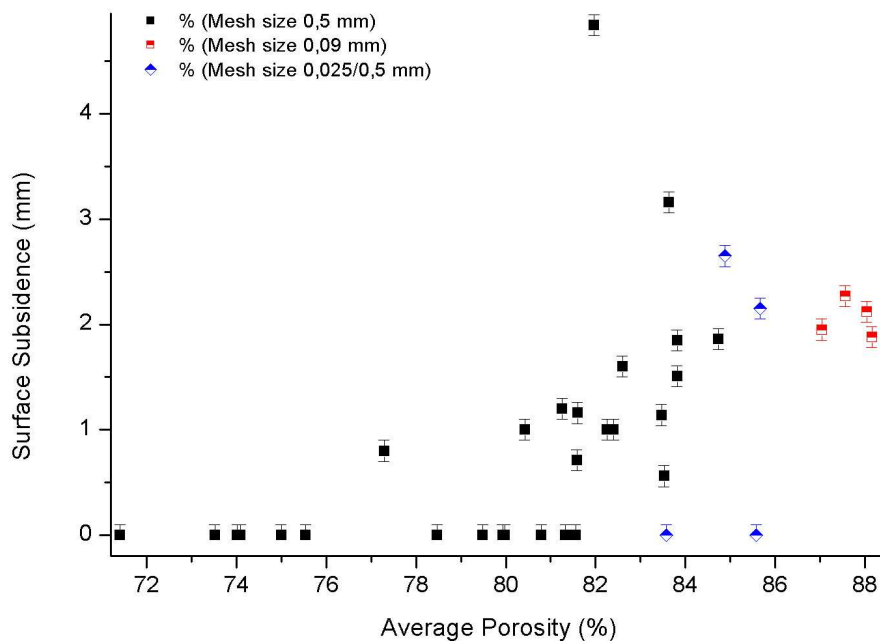
Fig. 3.7 Surface subsidence over target porosity taken from (Wurm, Paraskov, & Krauss 2005a). The subsidence of the target surface after an impact as a function of the average porosity of the target. The uncertainties in porosity are typically 0.5%. The bulk of the experiments were carried out with targets sieved through a 0.5mm mesh. There is a tendency of increasing subsidence with increasing porosity. Approximately below 80% porosity the impact does not lead to a structural collapse within the target. The experiments with targets sieved through a 0.09mm mesh resulted in higher average porosities and a rather well defined subsidence height. A few experiments have been carried out with a surface layer (~10mm) of dust sieved through a 0.025mm mesh onto a target otherwise prepared with a 0.5mm mesh. With respect to subsidence these targets more or less behaved like targets only sieved with a 0.5mm mesh.

This effect can be separated though from the immediate response of the target to the impact, which is visible on the surface on a much smaller timescale. Furthermore collapse of the target is restricted to targets that initially had a very high porosity

approximately above $P = 80\%$. Fig. 3.7 shows the tendency for more porous targets to collapse more strongly. The most porous targets were prepared by sieving through a 0.09mm mesh. Thus the granules on the surface are smaller. Some of these targets started to collapse before the impact of the projectile. In these cases the launch vibrations, which couple to the target via support structures, were already sufficient to initiate the collapse. But for most experiments the collapse does not start before the impact. In these cases the effect of the impact is dominating and responsible for the outcome of the collisions as described below. This holds as far as crater formation or ejection of particles is concerned. However, the collapse shows that an impact has the ability to mobilize particles throughout the target (Wurm, Paraskov, & Krauss 2005a).

For a series of targets the change of the porosity within the target before an impact was measured. For these measurements the usual target was prepared and a piston was used to push the dust upward in 5mm steps. Then the dust above the target holder was removed and the mass of the remaining target was measured, and so on. It might be assumed that the most porous layers are on top of the target. Indeed this is found as shown in Fig. 3.8.
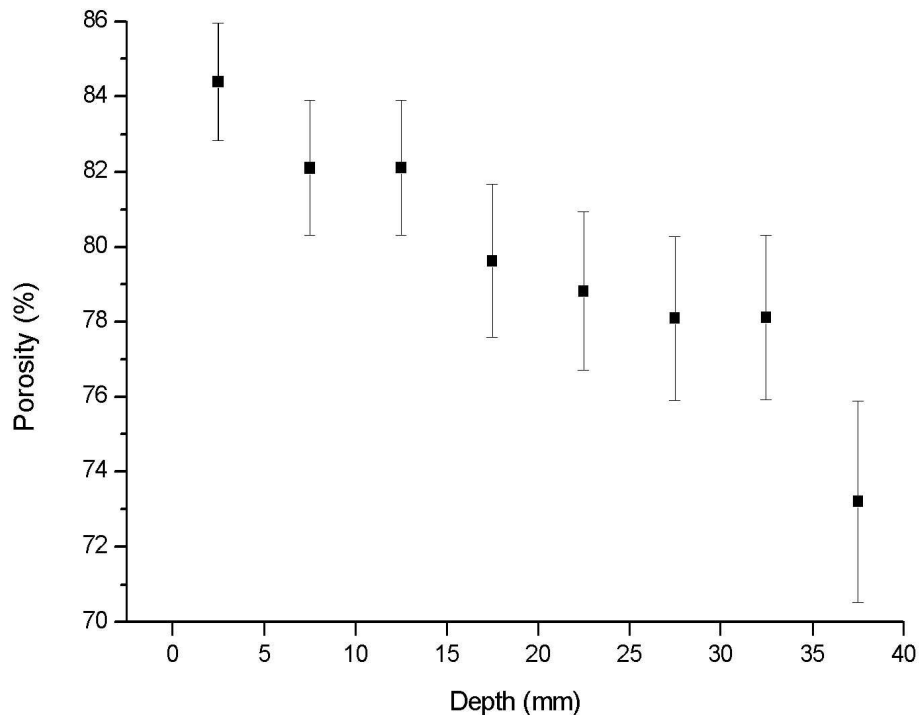
Fig. 3.8 Target porosity over target depth. Target porosity dependence on the vertical position in the targets, as typically used during the experiments. Marked as error bars is the standard deviation. The data is consistent with a linear dependence of porosity on the load (gravity of target material above a given position). If so this target would be much more compressed by load than the targets prepared by Blum (2004). To avoid too much subsidence during an impact the target was manually slightly vibrated approximately after 2/3 of filling and before the top layer was filled in. The steps at 5mm and 15mm depth might thus be real and due to this process.

On average there is a slight decrease of porosity from the top layers to the bottom layers. Individual local porosities might significantly deviate from this mean curve

though (marked as error bars). If this is important for the outcome of a collision is not clear yet. If the decrease of porosity is due to the mass load by upper layers then the effect is stronger for the targets that we prepared, compared to the dusty bodies generated by Blum (2004), where no effect should be visible due to the small weight of the dust mass. However as seen before, due to gravity, the surface of the target moves down during an impact as the vibrations lead to a compaction. To avoid subsidence during impact the target was vibrated manually approximately after 2/3 of filling and before the top layer was filled in. The steps at 5*mm* and 15*mm* depth in Fig. 3.8 might thus be real and due to this process. In any case vibrations induce subsidence as well as the impacts do. This suggests that the effect of a collision might be more pronounced than a quasi-static compression because a larger part of the target particles are mobilized first.

For most experiments, the target is built up from granules that are typically 0.5*mm* in size, which themselves are rather compact consisting of (sub)-*μm*-sized dust. These are two size scales, which might be of importance. A compacted layered body (chess board) of contacting spheres of the same size would have a porosity of approximately P = 50%. Therefore, if the dust within the granules is densely packed and if the granules are also densely packed in the target the overall porosity would be on the order of 75%. This is comparable to the porosities of the targets in our experiments. If during an impact mostly the larger granules as units are interacting, it might be of importance that they are packed rather densely even though the overall porosity looks high. One might easily think of targets with similar porosity but completely different morphology. Thus, impacts into targets of the same porosity could have different outcomes e.g. with respect to ejecta and ejecta velocities, but this remains to be seen.

3.2.2 General description of the impacts

We carried out a total of 46 experiments with porous targets (Table 1 Appendix). The impacts into highly porous targets resulted in craters of several *mm* depth and 2-3*cm* width. An example can be seen in Fig. 3.9.
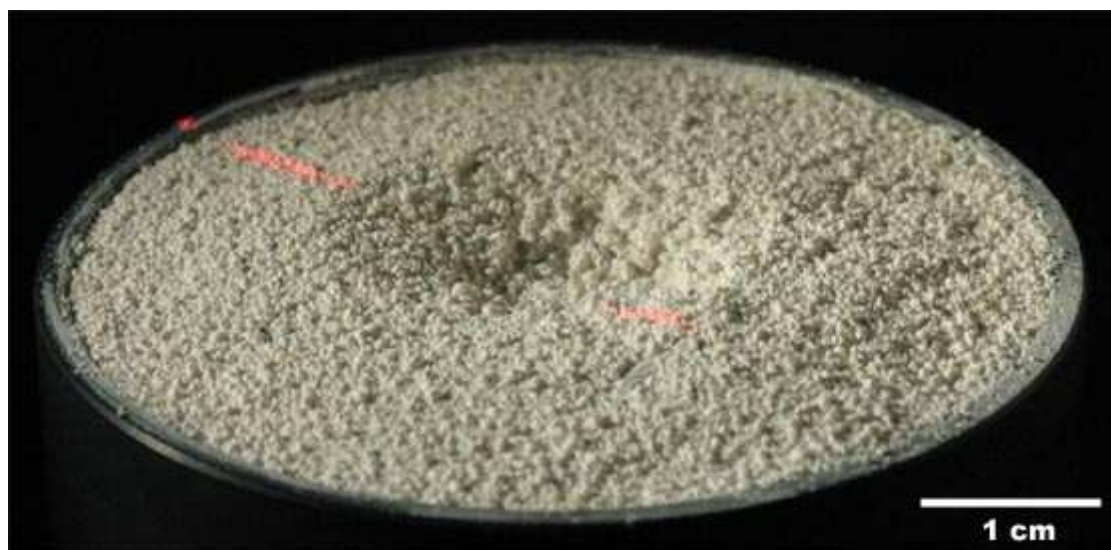
Fig. 3.9 Impact with porous target at 25m/s. The impacts at these velocities resulted in a crater formation. The diameter of the crater is ~ 2-3cm.

If the craters form by compaction due to projectile impact right on the spot of the impacting projectile, different projectile configurations (fragment distributions) should create quite different craters. This is essentially what the experiments show. For one impact a projectile was stroboscopicly illuminated, which was fragmented to a large degree. The light level on the image is a measure of the spatial distribution of the projectile fragments. They fit well with the crater profile in that experiment, measured by scale paper slicing the crater. This suggests that the depth of the crater at a given position is proportional to the impacting mass. Within the small velocity range studied and the uncertain mass densities, a correlation between impact speed and crater depth cannot be given yet (Wurm, Paraskov, & Krauss 2005a).

Sometimes the bottom of the crater qualitatively seems to consist of a number of slightly larger dust units compared to the original target. This might be larger fragments from the projectile but so far it was not possible to distinguish target particles from projectile particles. The fragmentation of the projectile certainly depends on the impact velocity. Two experiments were carried out, where dust projectiles impact very slowly, at about $2m/s$. In these cases the original projectile could easily and unambiguously be reclaimed from the target. The projectile survived the impact and was buried in the target like an iceberg for 2/3 of its height.

In Fig. 3.10 two typical snapshots from an experiment are shown. The left image is taken a few milliseconds before the impact and shows the projectile during the flight. In the right image we can see the crater forming after the impact.
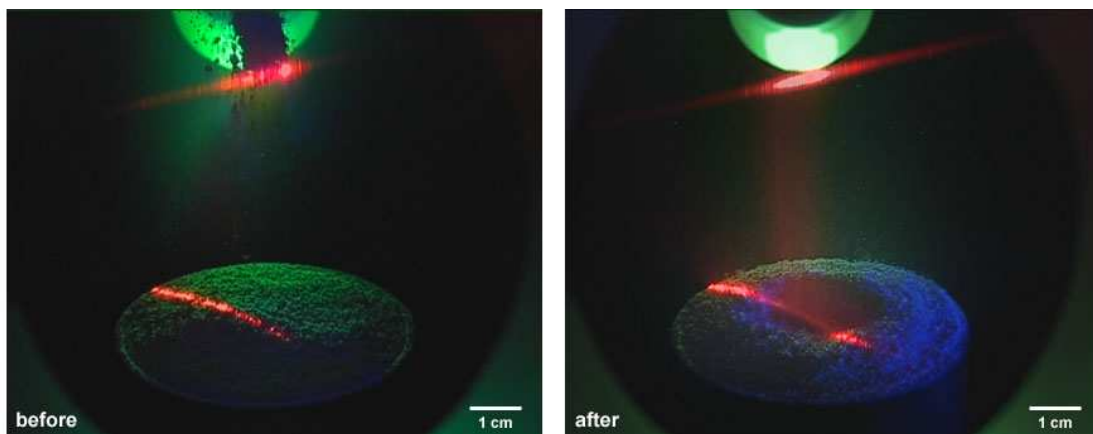
Fig. 3.10 *Video camera images. The left image shows the projectile during the flight few milliseconds before the impact. The projectile (~1cm in size) viewed with the video camera in bright field illumination is optically thick. The right image shows the crater after the impact.*

3.2.3 Accretion efficiency

One quantitative measure of the impact is the transfer of mass from the projectile to the target. We define *accretion efficiency* as the mass added to the target relative to the impacting projectile mass (not the target mass). Thus the overall mass of the target is not important here but only the fraction of mass it might loose or gain due to the impact. Fig. 3.11 shows the accretion efficiency as a function of porosity of the target. This also includes data of very fragmented projectiles.
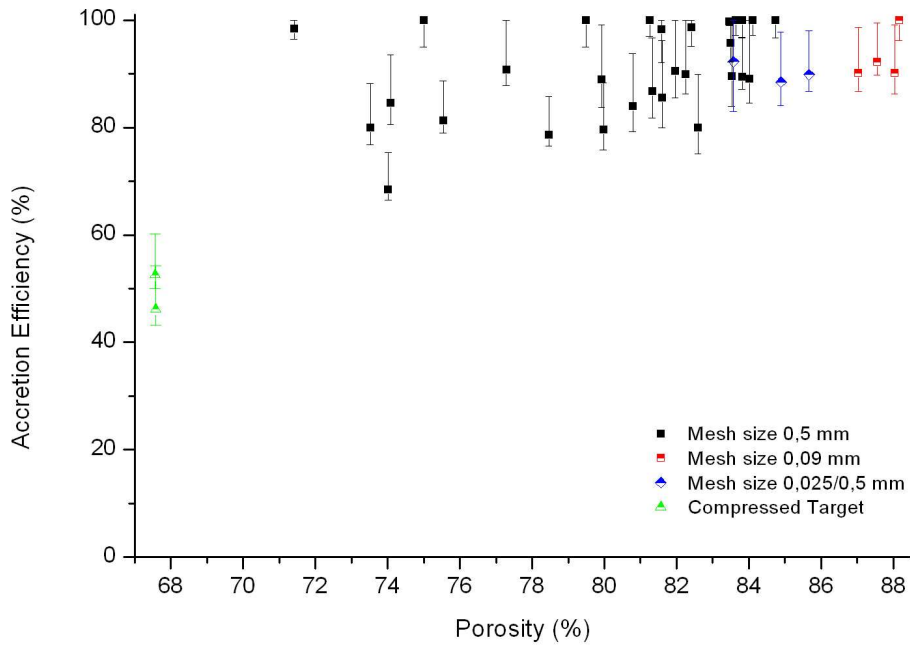
Fig. 3.11 Accretion efficiency over target porosity. The accretion efficiency of the target with respect to the projectile mass as function of the porosity of the target. The uncertainties in porosity are typically 0.5%. Accretion efficiency is defined as mass added to the target relative to the impacting projectile mass. The uncertainties in mass gain are mostly due to the uncertainties in determination of the projectile mass impacting the target. With each impact being individual the estimation of the uncertainties results in asymmetric error bars. The most porous targets were sieved with a different mesh size than the average target. Essentially the mass of the projectile is always added to the target. Also shown are two experiments into compressed targets at the lowest porosity described later, which show a significant decrease in accretion efficiency. The experiments with compact targets are described in detailed in the next section.

The accretion efficiency shows no dependence on the impact velocity. A factor of 2 in impact speed does not show any influence on the amount of mass added to the target. This indicates that fragments are very slow and any variation in fragment speed is insignificant with respect to the escape velocity of the target (in our earthbound laboratory). This measure of accretion efficiency is not to be confused with accretion efficiency a target would have under microgravity conditions, which would depend on the target size and the ejecta mass. Due to gravity the ejecta in our experiments return to the target where they were ejected. Here the accretion efficiency is to underline that most of the projectile is added to the target. Besides from any imaging these measurements allow to determine an upper limit for the rebound velocities of fragments. Under vacuum a particle originating in the center of the target can reach the edge and is lost if it is faster than approximately 0.5*m/s* (assuming a rebound angle of 45°). This upper limit is only important for the smaller particles of up to several micrometers in size, which cannot be imaged individually. For the larger particles the estimate of rebound speed is much better confined by the images as described in the next subsection. Thus, the mass gain here is to show that we are not missing any

ejecta, which are fast but too small to be imaged. However, in addition to the accretion efficiency measurements we further exclude a larger fraction of smaller particles. They would create a diffuse background on the images, which is typical for impacts into compact targets, but not here.

3.2.4 Fragments

We usually observed a certain amount of fragments rebounding from the target after a collision (Fig. 3.5 left image). Particles that lift off approximately 0.1*mm* from the surface can be detected. Due to gravity the minimum detectable velocity is thus about 50*mm/s*. If originating inside a crater, velocities have to be higher for a particle to be imaged. E.g. at 5*mm* crater depth the detection limit would be 0.3*m/s*. We have two different measures of rebounding particles. First, the flashlamps give a snapshot at a predetermined time after impact. They are thus directly related to the impact. Second the laser sheet shows particles, which pass a thin (<1*mm*) layer perpendicular to the target surface.

We see no fragments, which can unambiguously be traced back to the crater itself. In very few cases we observe a small amount of ejected fragments localized somewhere on the surface. We think that these might be the result of somewhat slower impacts of small individual projectile fragments. Estimates based on the images suggest that only a few *%* of the total incoming projectile mass (if any) is within these rebounding fragments. Their velocities are between 0.4*m/s* and 0.8*m/s*. Since they only account for a very small fraction of mass with respect to the projectile, we do not consider them to be of significance here.
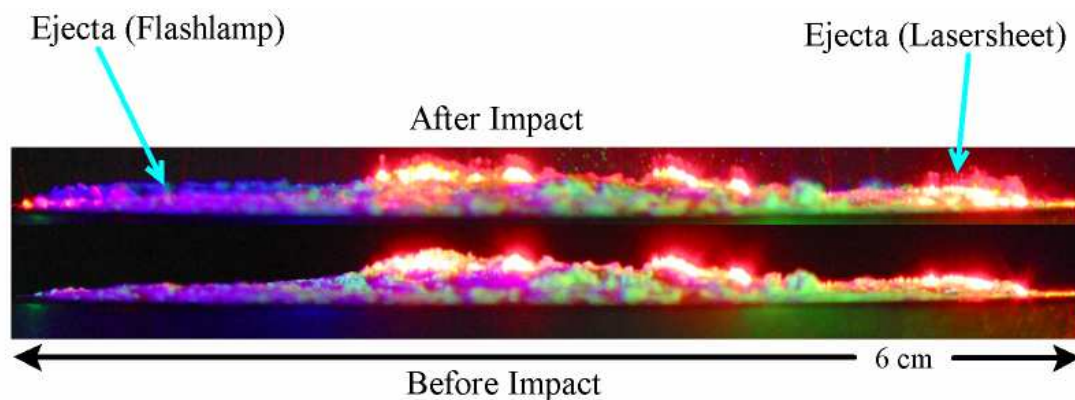
Fig. 3.12 Ejected particles after an impact. The image shows a target before (bottom) and shortly after (top) a collision with a projectile. Two flashes (blue and green) and a red laser were used to illuminate the target surface. The target has a 1cm surface layer sieved by a 25µm mesh on top of a target sieved by a 0.5mm mesh. Ejecta can be seen in the blue flash on the left as well as in the laser curtain on the right. They show a constant maximum height for fragments all over the target surface.

A large amount of dust is ejected, which is not correlated to the impact site, but can be seen to emerge from the whole surface. These particles are all in a comparable height above the target even tracing the "skyline" of the target surface as can be seen in Fig. 3.12. Due to possible shadowing the size of the imaged ejected granules does not always have to be the true size but a typical ejected particle has a size comparable to the sieve mesh size of 0.5*mm*. In support of this, large parts of the

target surface qualitatively look almost unchanged after an impact. The surface keeps its granular structure. Thus it is very likely that the size of the ejecta is identical to the size of the topmost layer of granules.

There is remarkably little scatter in the maximum height of ejected particles. While we cannot exclude slower or smaller fragments hidden, the sharp line of ejecta suggests rather steep upper cut-offs for rebound velocities for particles ejected in a direction opposite to the impact direction. No significant component perpendicular to the impact direction can be found.

The amount of ejecta is larger than the projectile mass. From the images it might be estimated that at least half of the surface lifts off. If all ejected dust units are $0.5mm$ granules the ejected volume is about $10cm^3$. Thus about 10 times the mass of the projectile can be ejected. Since the low velocity of the ejecta is close to the limit detectable in a ground based experiment no further sampling of the mass can be done. In recent microgravity experiments Wurm, Paraskov and Krauss (unpublished data) show that an impact at the same impact conditions (targets, projectiles and projectile velocity) can have a very destructive outcome and the target can losse much more mass in comparison with our ground based experiments.
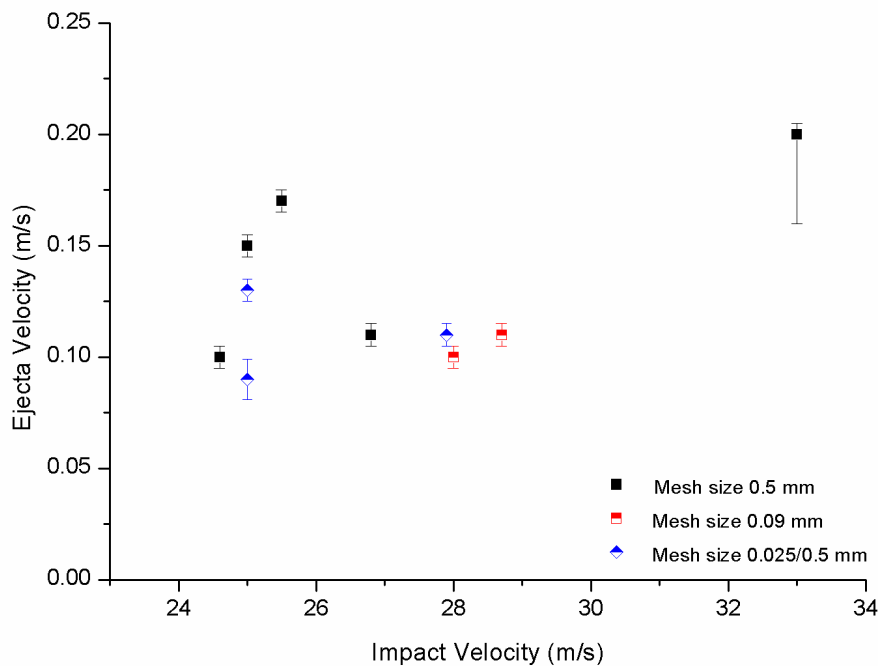
Fig 3.13 Ejecta velocity over impact velocity. Velocities of particles ejected on the whole surface. Only experiments with a well confined projectile and an unambiguous image of ejecta have been selected from the whole sample of experiments. An exception is the impact at 33m/s where the main part of the projectile (which we assume to be well confined in this case) was not imaged, which results in a timing uncertainty giving different error bars. Taken from (Wurm, Paraskov, & Krauss 2005a).

Within our impact velocity range there is no significant dependence of the fragment speed on the impact velocity as seen in Fig 3.13. While the impacts that were used to analyze the ejected particles are similar, projectile mass, size, and shape always vary

slightly. Thus we cannot determine or exclude a dependency on impact energy or energy density (with respect to the projectile size) within our range of data.

An important quantity for an impact is the *coefficient of restitution R,* which we define here as

$$R = \frac{v_{eject}}{v_{imp}} \tag{3.2}$$

with v_{eject} being the speed of a particle ejected from the target after a collision and v_{imp} is the impact velocity of the projectile. Within our impact velocity range the coefficient of restitution is $R = 0.005 \pm 0.001$, which is very low.

The experiments imply that elastic waves are launched during the impact and that part of the top most layer of the target is lifted at the arrival of this wave. This requires sufficiently high momentum transfer as well as sufficiently low sticking of the top layer. The individual 0.5*mm* dust units are only weakly bound by a small number of contacts via surface forces between dust particles. They easily roll down small slopes. Thus they can easily be ejected. In one experiment we vibrated the target slightly before the impact and the loose clumps rolled down to the base of a dust pile in the center to the outer target surface. During the impact essentially these particles lifted off. The particles that were bonded more strongly to their surrounding on the dust pile and that did not move due to the vibrations did not come off as numerous during the impact.

Since the lift height of the target surface does not significantly depend on the position on the surface, the waves seem to be well dispersed before reaching the surface. Thus this effect is probably not caused by waves travelling on straight lines from the crater to the surface since the strength should vary noticeable with distance. The responsible momentum transfer is most likely opposite to the impact direction, since otherwise no preferred rebound direction of individual fragments at a given position on the surface should be found (Fig. 3.12). A wave reflected from the bottom of the target tray might be plausible though further studies are needed to confirm this. We measured the speed of sound in the targets to be between 45*m/s* and 50*m/s*. Since our targets were about 50*mm* in height we account for 2*ms* between impact and fragment ejection at arrival of the wave in Fig. 3.13. Thus, we assume that a reflected wave is responsible for ejection.

Ejection itself might take up a significant part of the energy of the elastic wave. With 10 times the projectile mass at 0.5% of the impact velocity a fraction of 2.5 x 10^{-4} of the impact energy is distributed to the fragments. For an $m = 0.3g$ projectile at approximately $v_{imp} = 25m/s$ the impact energy is about $E_{imp} = 0.1$ J. In addition some energy is used to break up the contacts. To estimate the amount of energy needed to break up contacts, we first estimate the number of contacts to support a granule. We will base our estimation of the number of contacts on geometrical arguments. As discussed above we assume that the ejected particles are the compact granules, which we have sieved as last layer onto the surface of the target. We regard these 0.5*mm* aggregates at the top essentially as individual solid spherical masses for simplicity here. However, each granule has a certain contact area with the granules below, in which sticking of individual dust particles occurs. As radius of the contacting dust particles we take 1*μm*. A compact granule thus has a "surface roughness" of about 1*μm*. On one side if a granule would have individual parts sticking out further from its surface before contact these would easily be compressed first (Blum & Wurm 2000). On the other side compression beyond the

rim thickness is not possible for a compact granule. Therefore, in contact two granules will approximately intersect over the rim thickness of ~1μm as indicated in Fig 3.14. With this assumption the contact area between two spherical granules can be estimated to be about 1600μm^2. For 1μm (radius) dust particles this corresponds to $n = 400$ particles in contact if we assume the particles to be arranged in a chess board like manner over the cross section. It has to be noted that this is only a rough estimate, which will vary by a significant factor depending e.g. on the size distribution of the used dust particles, granule size, or porosities (Wurm, Paraskov, & Krauss 2005a).

The energy needed to separate two dust particles in contact is $E_{br} = 10^{-15}$ J (Blum & Wurm 2000). For 400 contacts energy on the order of 4 x 10^{-13} J is dissipated in breaking up the contacts of a single granule. Compared to the kinetic energy of 8 x 10^{-10} J of the granule after ejection this is a factor 2000 less energy.

However, the wave will depend on the parameters of the impacting projectile and target (mass, velocity, size, porosity). Thus there might be a lower limit in projectile size and impact velocity, e.g. of *mm* particles impacting at less than a few *m/s*, where the energy needed to break up the contacts would be larger than provided by the wave and no ejecta should be produced.
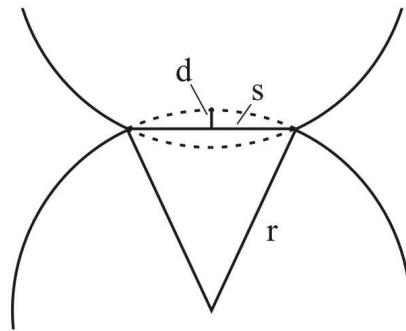
Fig. 3.14 Granule support model to estimate the number of contacts between dust particles at the intersection of two granules. If the rim thickness d is taken to be d = 1µm (dust particle radius) for an r = 250µm radius granule the radius of the cross section is s = 22.3µm. Thus the cross section is about 1600µm². For 1µm radius dust particles distributed in a chess board like manner on this area these are about 400 dust particles in contact.

Only the experiments with a well confined projectile are shown in Fig 3.13. Images for dispersed projectiles can be interpreted less unanimously and are not shown but there is evidence that if a collective behaviour of the surface can be detected at all, the motion is much slower in agreement with the arguments given before. To determine if a significant part of fragments can be ejected at much lower impact energies microgravity experiments have to be carried out. As mentioned above microgravity experiments have been carried out recently by Wurm, Paraskov and Krauss but a more detailed analysis of those still has to be carried out. A preliminary result is that the impact energy needed to eject a granule from the target surface in microgravity is actually much lower as could be detected in our ground based experiments.

If a wave reflected on the bottom is responsible for ejection, then ejection at distances of 10*cm* (two times the height of the target) or more from the point of

impact is possible. If no target tray would support the dust, ejecta might be observed on the opposite side of the impact. This is supported by tests of an impact-like impulse generated at the bottom of a dust target.

A first look at the microgravity experiments, using essentially the same dust targets and projectiles, shows a more complicated picture. The amount of ejecta on the front (impact) side of the target is depending on the impact energy. At equal projectile mass the impact energy is proportional to the impact velocity. Impacts carried out at 20*m/s* showed a very destructive behaviour. A large amount of ejecta is observed on the front side of the target. The surface is lifted but also deeper layers are involved. Depending on the impact energies and projectile type, the back side of the target survives the impact intact or gets eroded as well. Obviously the target has very good damping characteristics and the energy densities of the impact waves are below the necessary threshold needed to break the contacts between the particles. The elastic wave ejection mechanism might be restricted to the upmost layer of dust granules with additional effects changing the structure of the whole target but this has to be seen in a forthcoming analysis and is beyond the scope of this thesis.

If the target would be much larger, e.g. meter-sized, then no ejecta at all would be produced at the bottom side. Already dilution of the energy density of a spherical wave would be a factor of 100 scaling from 10*cm* to 1*m* in size. To study the effect of dust unit (granule) size, which is determined by the sieving mesh, we also prepared targets by sieving through a mesh of 90*µm* and 25*µm*. These targets consisted of much smaller dust units. The targets consisting of 90*µm* dust units were the most porous targets we prepared with P = 88%. A few of them already collapsed due to the launch vibrations as mentioned before. Due to the time consuming process of sieving we filled the 25*µm* targets on a base of 0.5*mm* sieved targets with the top layer of 25*µm* units being about 1*cm* in height. Fig. 3.12 actually is one of the 25*µm* targets. As can be seen in Fig. 3.13 the ejecta velocities are comparable to the velocities of the larger dust units within the variations between individual experiments. Obviously there is little or no dependence of the ejection velocity on the granular size of the dust units if varied by a factor of 20. In general less massive (smaller) fragments will have fewer contacts. Under the same assumptions as given above a 25*µm* granule would have n = 20 contacts. The number of contacts is thus approximately increasing linearly with size. If the whole upper layer lifts off, the momentum transferred to the ejected particles at a given ejection velocity is also depending linear on the size of the granule. Thus, if the total momentum distributed to the next upper layer is constant, so will be the ejection velocity, which is qualitatively in agreement with the observation.

3.2.5. Discussion

An impact of a ~ 1*cm* projectile into a highly porous dust target at 16.5 to 37.5*m/s* produces a crater. No significant ejecta from the crater can be found after the impact, but a large amount of material of at least 10 times the projectile mass is ejected over the whole surface of the target. These ejecta are very slow with velocities between 0.09 and 0.20*m/s* in different experiments, or typically 0.5% of the impact velocity. This is in agreement with the microgravity experiments to be analyzed in detail, though here some fragments emerge from the crater and the mass loss seems to be somewhat larger.

The upper limits for projectile (impact) and ejecta velocities are of primary importance to answer if planetesimal formation by growth can occur. In this manner it is often argued that impacts of millimetre- to centimetre-sized objects at several tens

of *m/s* cannot lead to growth. Indeed our experiments show that an impact ejects more mass than the projectile adds. The ejection of particles from the whole surface can be explained by elastic waves launched at impact and reflected at the bottom of the target tray. Further mass loss is depending on the morphology of the target and the drop tower experiments show that slightly more compact targets are resisting further impact erosion. Here we have to note that impact velocities for a 10*cm* body (as our target) are most probably below 10*m/s* in laminar protoplanetary disks and projectiles might on average be smaller (Weidenschilling & Cuzzi 1993). As mentioned before for smaller projectiles, in a slower collision a plausible explanation of our data would imply that no ejecta at all might be visible. Our impact velocities are more appropriate for a collision with the target being larger than about 50*cm* in size. If ersosion takes place, growth can still occur under conditions typical for protoplanetary gas-dust disks if we combine the experimental outcome of the impact with the effect of gas flow around and through these porous dusty bodies (Chapter 4). In Chapter 4 we discuss how gas flow can return ejected particles if they are slow enough. In our calculation we assumed fragments to be *μm*-size dust particles slower than 0.5*m/s*. The speed of fragments ejected by elastic waves found in our impact experiments here is typically much below this threshold. Thus a small fragment could be reaccreted by the gas flow. There should be no doubt though that collisions of the type studied here are critical for protoplanetary disks. Not all of them will lead to the formation of a larger body.

3.3 Experiments with compact dust targets

3.3.1 Target

The target is placed in the same aluminum tray with 6*cm* diameter and 5*cm* depth. The dust is compressed manually into the target tray. The target has a very smooth surface. Although the surface seems to be very compact (Fig. 3.15), the porosity of the whole target is still 65.7 ± 1.0%.

Fig. 3.15 *Compact target. A compact target prepared by manually compressing the dust in the target tray. Target porosity is 65.7 ± 1.0%.*

This value is in perfect agreement with the measurements carried out by Blum & Schräpler (2004). For a compressed dust aggregate consisting of $1.5\mu m$ SiO_2 dust spheres, they find a maximum volume filling factor of about 33%, at pressures higher than $10^5 Pa$. This maximum factor is independent on a further increase in pressure and stays constant (Fig. 3.16). The maximum filling factor of 33% corresponds to a porosity of 67%.
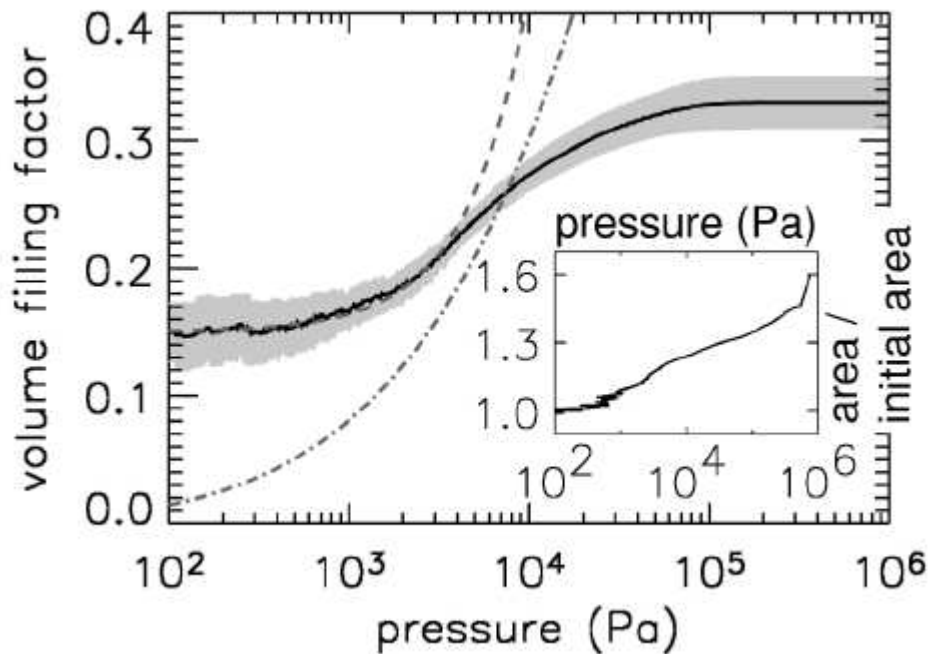
Fig 3.16 *The volume filling factor of an agglomerate consisting of SiO₂ spheres with 1.5μm diameter as a function of the unidirectional pressure. The gray-shaded area represents the standard-deviation error of the measurements.Taken from (Blum & Schräpler 2004).*

3.3.2 Low velocity impacts

In a small number of experiments the projectile was free falling without initial acceleration. At a fall height of about $2m$ this resulted in impact velocities, v_{imp}, of $v_{imp} = 6.7m/s$. The dust was compacted within the projectile holder for these experiments. Therefore, more individual dust particles get in contact with the walls of the holder, which increases the friction between projectile dust and holder. Due to this high friction the projectile strongly breaks up during launch. This results in a large number of smaller individual projectiles. Since these projectiles are also slightly dispersed in the horizontal direction they do not interact with each other further on and we get a large number of independent impacts distributed over the whole target surface in a single experiment. In these experiments the illumination was placed in a way to provide a bright field image in green and red. An image showing a section of a slow velocity impact is seen in Fig. 3.17.

We compare these impacts with experiments by Blum & Münch (1993), which had similar (somewhat smaller) impact velocities. In their experiments (among others) individual compact *mm*-sized dust aggregates collided with each other. Our projectiles were also compact *mm*-sized dust aggregates though consisting of different dust samples. With our target being large compared to the projectiles the

collisions might be comparable to the case of aggregates with large size difference as measured by Blum & Münch (1993).
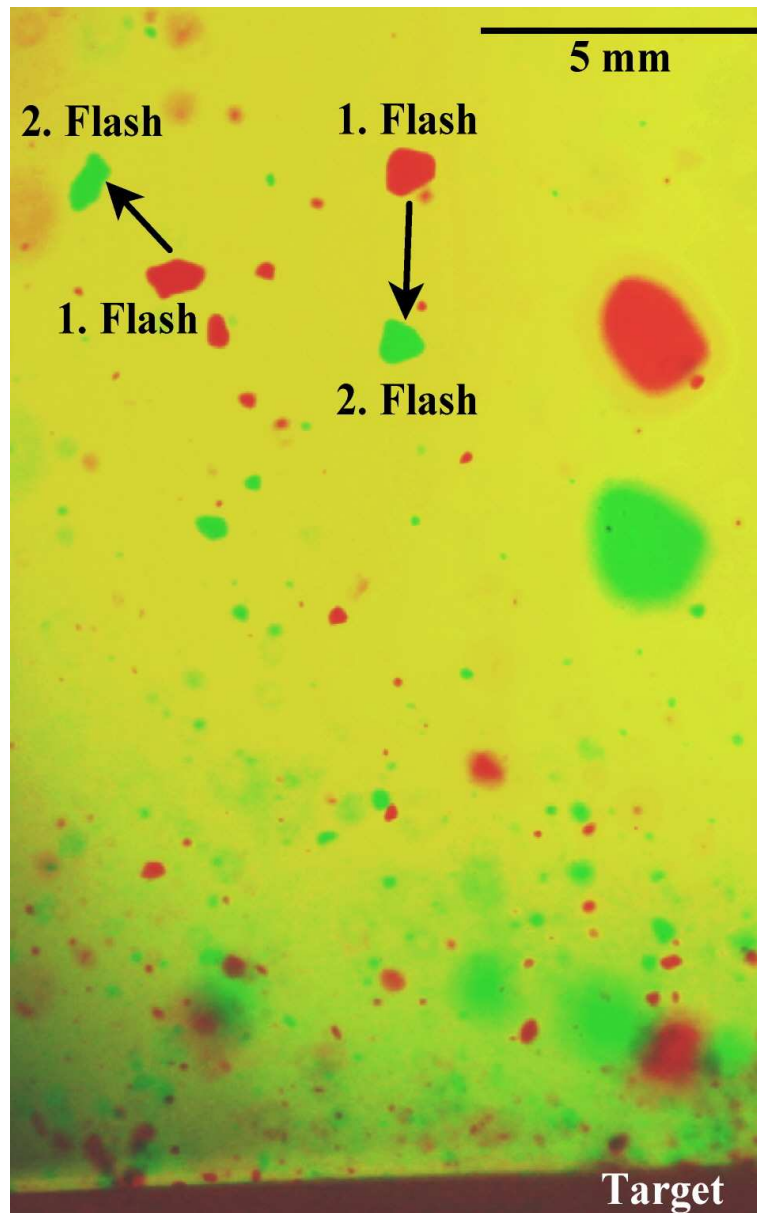
***Fig. 3.17** Contrast and color balance enhanced section of an image with slow velocity impacts (6.7m/s) of a number of projectiles onto a compact target. Bright field illumination is used with a red and a green flash lamp. The red flash is triggered later than the green flash, so the green particles correspond to later times on their trajectories. While impacting particles essentially have to move on straight lines toward the target (down in the image), ejected particles are heading away from the target in arbitrary directions. Two examples for an impacting (right) and ejected particle (left) are marked. Taken from Wurm, Paraskov, & Krauss (2005b).*

     While we cannot distinguish the individual collisions and ejecta of one projectile, we have a large number of projectiles impacting. One image thus gives an average for many individual collisions. We determined the sizes of the particles on one of the images in more detail. A histogram is shown in Fig. 3.18.
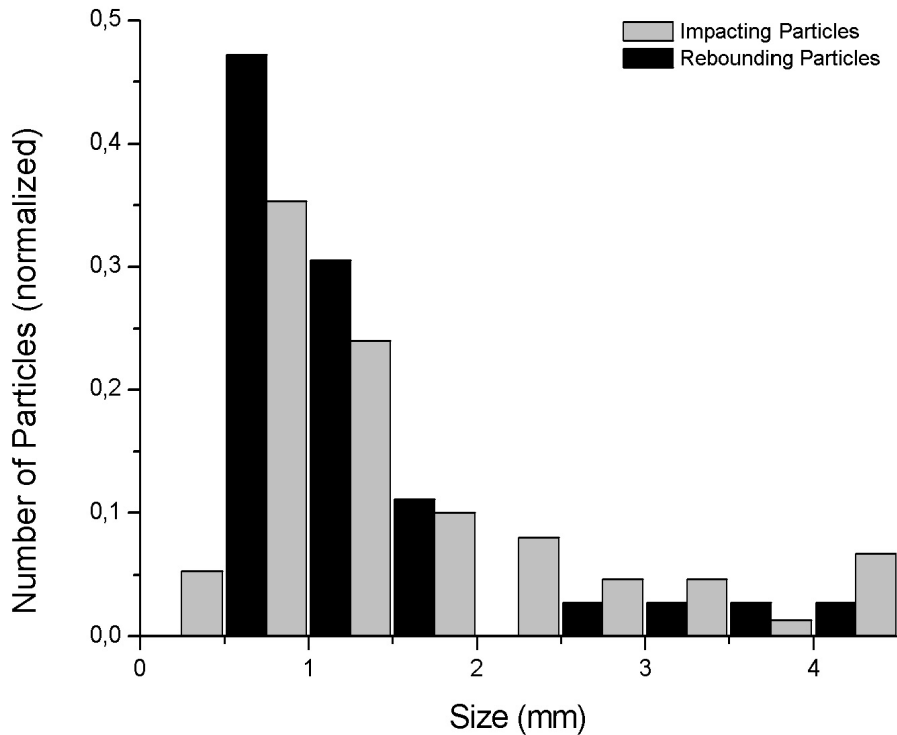
***Fig.* 3.18** *Size distribution of impacting (gray) and ejected (black) particles normalized to a total sum of 1. A total number of 36 ejected and 150 impacting projectiles were measured. Only particles, which could clearly be identified twice (imaged at different times) on Fig. 3.17 (whole image of the section shown), were counted. Ejected particles can move in different directions, which produce more ambiguity in matching particles. Impacting particles, which have to move down, can be matched more easily. Therefore, a smaller total number of particles could be identified as ejected. No ejecta could be identified unambiguously in the smallest size bin. The largest size bin includes all particles larger than 4mm. The two distributions are similar with a tendency of the ejected particles to be slightly smaller. This implies a small degree of fragmentation during impacts.*

Ejecta sizes are comparable to the incoming projectile sizes so fragmentation of the projectiles is not very effective. There is a tendency that ejected particles are slightly smaller though. Small fractal aggregates would be completely destroyed at these velocities (Blum & Wurm 2000). The compact dust aggregates are rather stable. This is probably due to a much larger number of contacts between dust particles, which have to be broken to separate parts of the projectile or target. However, the projectiles do not show a large affinity to stick to the target in contrast to the high velocity impacts reported later. All particles that eventually settle on the target due to gravity can easily be dropped or blown off (under atmospheric pressure) leaving a target surface, which looks much the same as before the impacts on a macroscopic scale (for the naked eye). This behavior is used in the high speed impacts described below to remove fragments from the target, which only return to the target due to gravity, but do not stick there, and marks them as returning ejecta of the primary collision.

We analyzed the velocities of all particles counted in Fig. 3.18. A histogram

of these velocities for the projectiles and the ejected particles is shown in Fig. 3.19.
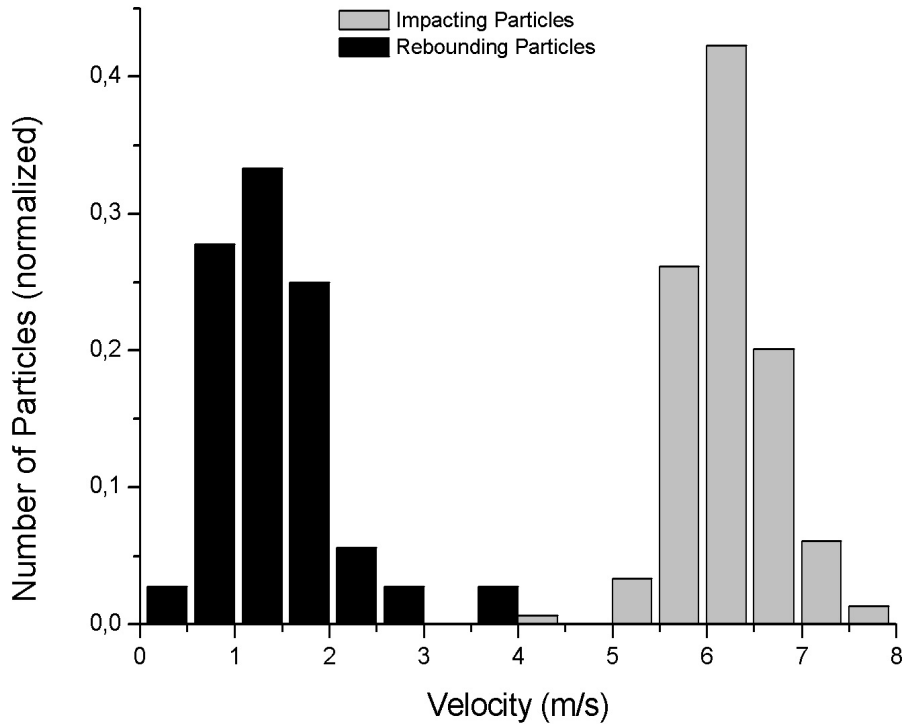
Fig. 3.19 *Velocity distribution of particles for impacting (gray) and ejected (black) particles normalized to a total number of 1 for each distribution. The average velocities are v_{imp} = 6.7m/s for the impacting particles and v_{eject} = 1.4m/s for the ejected particles. v_{eject} is the absolute value of the velocity of the fragments in the given direction. The average ejecta velocity coefficient is R = 0.21 ±0.08.*

An average value for the ejecta velocity coefficient (eq. 3.2) is $R = 0.21 \pm 0.08$. This is somewhat smaller than the values found in the work by Blum & Münch (1993). For the case of colliding particles with large size difference they get $R_N = 0.36 \pm 0.03$, where R_N is the coefficient of restitution with respect to the velocity components in the impact direction. Blum & Münch (1993) varied the impact velocity in a range from $v_{imp} = 0.15 - 4m/s$ and found only 2 cases (out of 24 collisions) of fragmentation at the highest impact velocities. This is comparable to our observation of only a small degree of fragmentation at 6.7m/s (see Fig. 3.18). It has to be considered that Blum & Münch (1993) used a different material (ZrSiO$_4$). The individual particle sizes are comparable though to our SiO$_2$ particles. The lower ejecta velocity coefficient found in our experiments might be due to the difference in particle powder or due to the somewhat higher impact velocities. Overall our results are comparable to their findings.

It should be noted that these results suggest that this kind of slow collision might not be very favorable for growth of a larger object or eventually planetesimals. However, increasing the impact speed yields a completely different picture as seen in the following subsection.

3.3.3 High velocity impacts

We conducted a total of 27 experiments with impact velocities from 6*m/s* up to 25*m/s*. Fig. 3.20 shows a typical impact with a compact target.
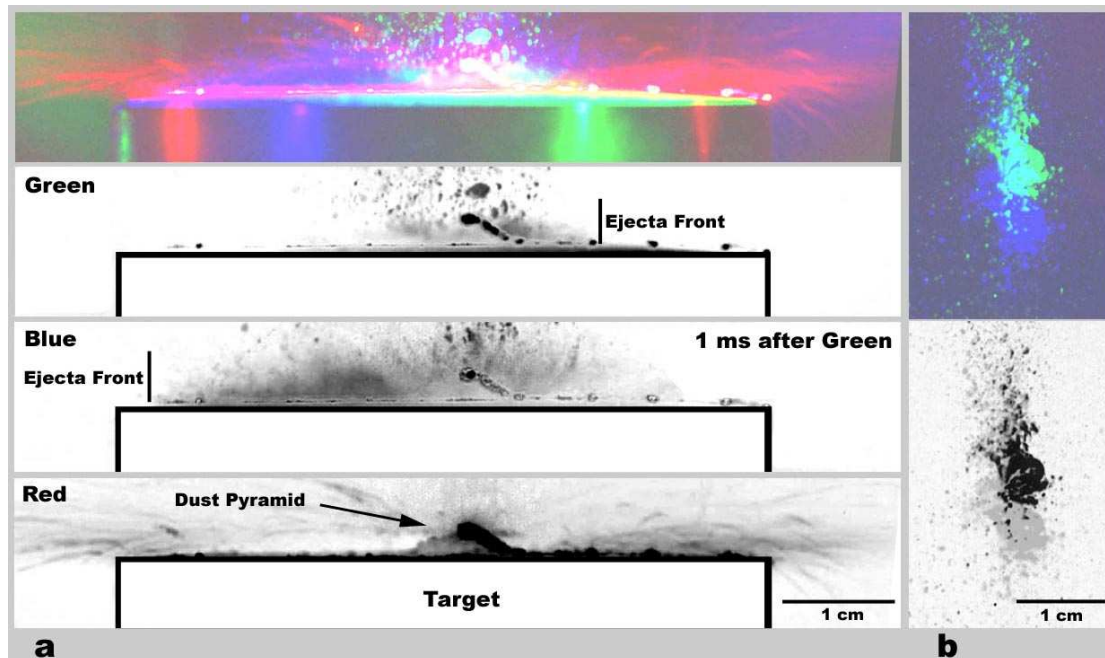
Fig. 3.20 *Impact with a compact target at 23.7m/s. Taken from Wurm, Paraskov, & Krauss (2005b) The high velocity impact at 23.7m/s is imaged on one color frame (a)(top). The individual color channels are shown below on a grayscale. Here, the target outlines are marked. The target surface is perpendicular to the image plane. The projectile moved from top to bottom. Therefore, the impact is seen from the side. Two flashes with a time difference of 1ms in green and blue are fired shortly after the impact. A diffuse dust cloud can be seen spreading to the side. From the ends of this cloud (ejecta front) the maximum ejecta velocities can be estimated to be 9.8m/s. With particles moving in all directions no restrictions on the lower velocity end of the ejected fragments can be taken from the diffuse cloud. Also visible in red light are slower ejecta illuminated by the laser sheet (see Fig. 3.2), which is on for the whole time, during which the camera aperture is open (4s). A pyramid like dust pile that forms due to the impact can be seen in the center of the target and is marked on the red channel. Shown on the right is a projectile as imaged at two different times.*

There is a tendency that impacts at high velocities of 20–25*m/s* resulted in a pyramid-like structure with a base comparable in size to the original size of the projectile (approximately 1*cm* in diameter). The pile's height is between 3*mm* and 5*mm*. A typical image of a pile resulting from a high velocity impact is shown in Fig. 3.21. The pile constitution qualitatively shows a similar resistance to force as the rest of the target. It is in firm contact to the target surface and it cannot be dropped or brushed off easily.

Besides the pile a number of fragments are found to be only lying on the target after an experiment rather than being rigidly stuck to it. These particles can easily be dropped off just by tilting the target more than 90°. It has to be noted that the original target – though porous – is a strongly cohesive compound of dust

particles in our experiments. No dust is removed from the original target if it is tilted 90° or more.

The low velocity impact analysis presented above shows that the pile (or the projectile fraction strongly connected to the target surface) must have resulted from the original impact and not from any ejecta returning to the target or from secondary collisions. This is because any material falling back to the target after an initial ejection would strike at a much lower speed, comparable to the experiments described in the previous subsection. Such returning ejecta would not stick rigidly and would easily drop off after tilting the target. This is the case with the particles surrounding the pile. The particles are only lying on the surface, reaccreted due to gravity. Therefore, in the pile we do not see accretion, which must be attributed to gravity but results from the impact itself. The recent microgravity experiments carried out by Wurm, Paraskov and Krauss confirm these observations. A similar impact in microgravity conditions results just like in our ground based experiments in a pile formation.

Only very small ejecta with a large (contact) surface to mass ratio are able to rigidly stick to the target after returning due to gravity and to withstand tilting of the target. In fact a few percent of mass is almost always accreted due to this effect as quantified below and seen in Fig. 3.23. This fraction would not be accreted under microgravity but is small compared to the mass of the main part of the sticking projectile.
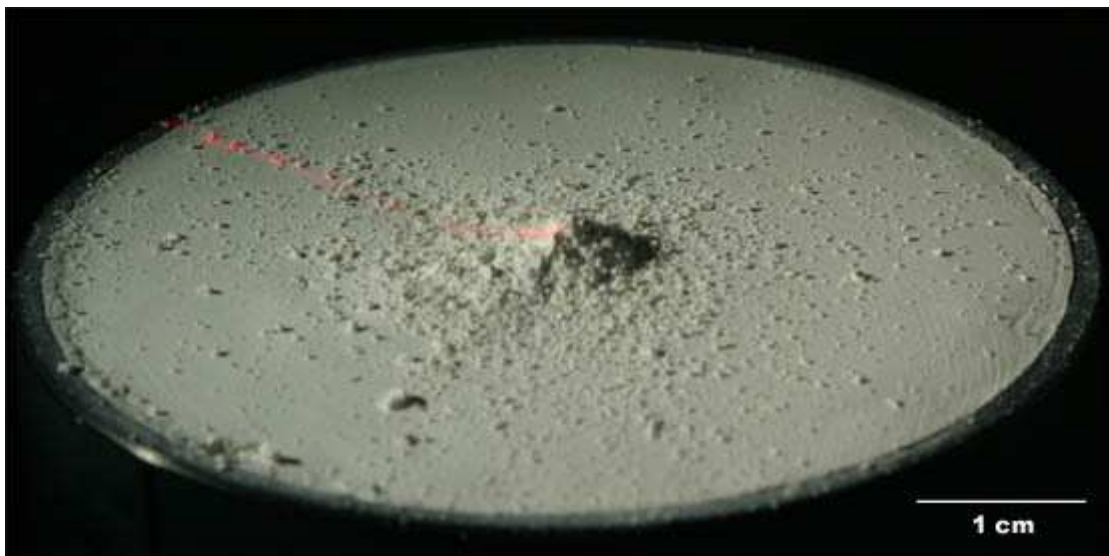
Fig. 3.21 Impact with a compact target at 22m/s. The impact resulted in pile formation. The pile is comparable in size to the original size of the projectile (~1cm), is in firm contact to the target surface, and shows a similar resistance to force as the rest of the target. Besides the pile a number of fragments are found after an experiment on the target surface. They do not stick rigidly to it.

With decreasing impact velocity the pile changes its structure. Impacts at 15-20*m/s* resulted in a less compact pile structure. It can be found that projectile fragments, which surround the pile, are getting larger at intermediate and smaller speeds. At 12-13*m/s* we observed a transition. An impact below this velocity doesn't give rise to a pile, but the projectile survives the collision or breaks up into 1-2 big pieces (Fig. 3.22). These large aggregates can be found bouncing off, but leaving an

imprint into the target surface, which can be several *mm* deep. Therefore, the target is not behaving like a solid surface but actively takes part in the impact even if it is compact. There is currently no experimental implementation to resolve the inner structure of the target, though this would be important for further studies and is planned for the future. We observed an impact at 12.7*m/s* where the projectile survived the impact and got stuck in the surface. We removed the projectile and measured a hole with depth approximately 50% of the projectile diameter. The surface structure changes have to be the focus of future studies.

Fig. 3.22 *Impact with a compact target at 11m/s. Impacts at this velocity don't give rise to a pile. The projectile survives the impact (or breaks up into 2-3 big pieces) and stays lying on the target surface. This will be not the case in microgravity.*

3.3.3.1 Accretion efficiency

One of the most important quantities for an impact with respect to the question if planetesimals can form is the mass gain/loss during a collision. The *accretion efficiency* for the experiments as a function of the impact velocity is shown in Fig. 3.23. Accretion efficiency as defined in the previous section is the mass difference of the target after an impact with respect to the projectile mass. An accretion efficiency of 1 (100%) thus means that the whole projectile mass has been added to the target, which would be the maximum achievable.

We observed that the accretion efficiency depends on the impact speed. At the highest velocities (25*m/s*) a large part of the projectile sticks to the target, which can be as much as 50% of the projectile mass, and forms a pyramid-like structure as mentioned before. This value can vary for an individual collision from about 30% to 70% but on average is constant down to impact velocities of about 13*m/s*. As the impact velocity decreases below this threshold only a little mass sticks to the target. The accretion efficiency is less than 10% on average. This is consistent with the slow collisions described above. The remaining few % sticking to the target might be very small fragments, which would indeed be able to stick to the target at low impact velocities after one or several rebounds. Under microgravity this fraction of sticking dust might be reduced but this has to be studied further. We observed one impact (labeled no 83) just on the edge of sticking. The projectile was essentially intact and

stuck to the target; it remained stuck while the target was tilted, but a mild knock loosened it. In another case, some mass from the target was observed to be stuck to an ejected projectile, which would lead to a slight mass loss of the target.
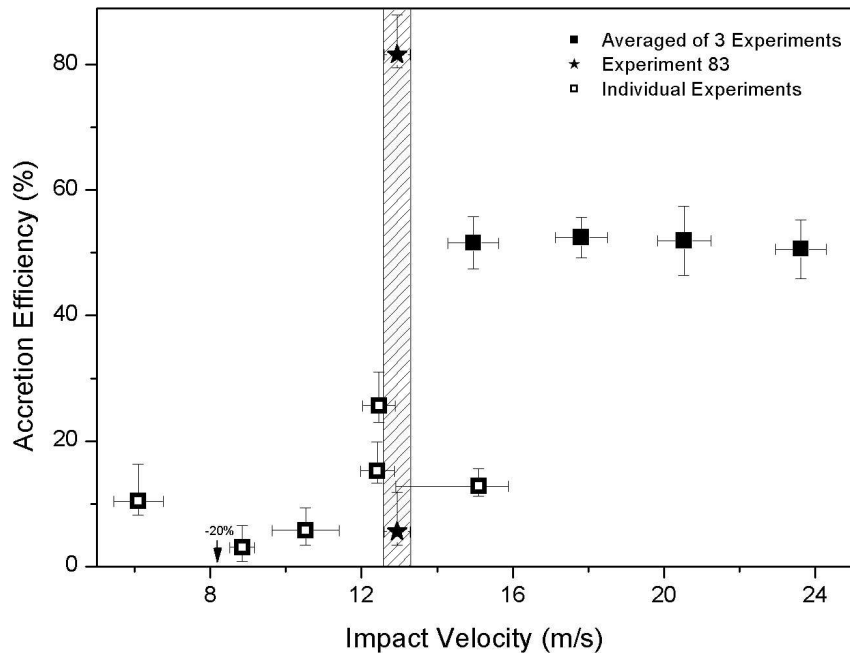
Fig. 3.23 Accretion efficiency over impact velocity. Accretion efficiency refers to the mass gained by the target with respect to the projectile mass in %. The target mass is measured after the free particles, which are not bound to the surface, have been dropped off by tilting the target. These particles in general would not be on the surface in microgravity. They are slow ejecta that return to the surface due to gravity. In the case of experiment 83 the projectile remained stuck after tilting the target but fell off after applying a slight manual impulse to the target. The filled squares are values averaged over three individual experiments each with accretion efficiency much larger than 30%. Due to a larger deviation of individual experiments at high velocities and the larger number of high speed impacts this visualizes the whole data best. The open squares are individual experiments at the lower impact velocities with accretion efficiency below 30%. In one case material from the target was sticking to a fragment leaving, which resulted in mass loss of the target of 20%. Taken from Wurm, Paraskov, & Krauss (2005b).

The experiments show that the fragments become larger at intermediate and low speeds, approaching the original size of the projectile for the slow velocities, in agreement with the results given above for the free fall experiments. For intermediate speeds large aggregates can be found bouncing off but leaving an imprint into the target surface, which can be several *mm* deep.

3.3.3.2 Chamber wall observations

At the high velocity impacts (over 20*m/s*) large parts of the projectile (average 50%) sticks to the target surface, but the remaining part of the projectile is ejected after the

impact. The result is a cloud of fast fragments, which escape quickly from the impact side. This cloud can be seen very well on the images taken during the impact (for example on Fig. 3.20). From the outer extent of the dust cloud in different colors corresponding to different times the maximum fragment velocity is determined to be 40% ± 10% of the impact velocity, which is an ejecta velocity coefficient $R = 0.4 \pm 0.1$ for collisions faster than $20 m/s$. Due to the two dimensional imaging no limit on the smaller fragment velocities can be taken from the clouds. Ejecta velocity coefficient $R = 0.4$ for these high speed collisions correspond to ejecta velocities greater than $9 m/s$. The particle trajectories ejected within a 32-cm chamber ($16 cm$ from the center to the walls) are almost straight lines. It is interesting to note what happens when the fragments hit the wall of the chamber. An image of particles at the chamber wall can be seen in Fig. 3.24.
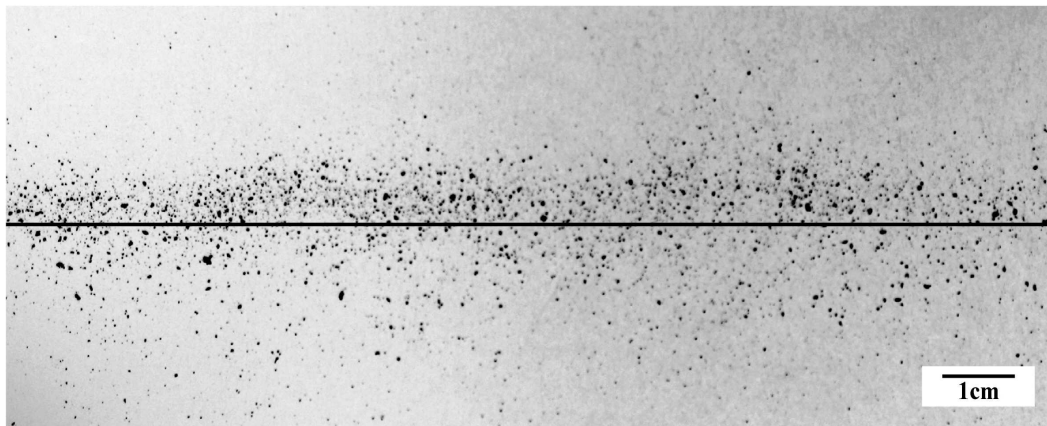
Fig. 3.24 Chamber wall image. Image of particles at the inner chamber wall (inverted for visibility here). The solid line marks the approximate position of the target plane.

Most of the particles ejected during fast impact stick to the wall. There is a rather sharp line of particles at target height. This implies that the ejection angles with respect to the target surface are rather flat in qualitative agreement with the images of the impacts. To quantify the distribution of particles in height over the plane of impact we summed up the intensity (pixel brightness) for a given height in image Fig. 3.24. The resulting height profile of fragments is shown in Fig. 3.25.

Particles are essentially limited in height to $1 cm$ above the target surface with a strong concentration towards smaller heights. There are a number of particles below the target plane. These particles are probably indeed heading downwards with respect to the target plane and originate at locations of the sticking projectile above the target. The lower limit is roughly in agreement with straight trajectories from the top of the sticking projectile to the wall. In detail there is ambiguity if particles on the wall originate e.g. at the bottom of the projectile (target surface) and move slightly upwards or if they move horizontally but originate further upwards on the projectile pile. Assuming the majority of fragments originating at the target level a maximum ejection angle can be estimated to be 3° with respect to the target plane. While we marked the plane of the surface by a laser tangential to the upper target end the dust plane is e.g. never completely flat. We estimate an error of 1° for the angular scale in Fig. 3.25, which is included in the maximum ejection angle of 3°.
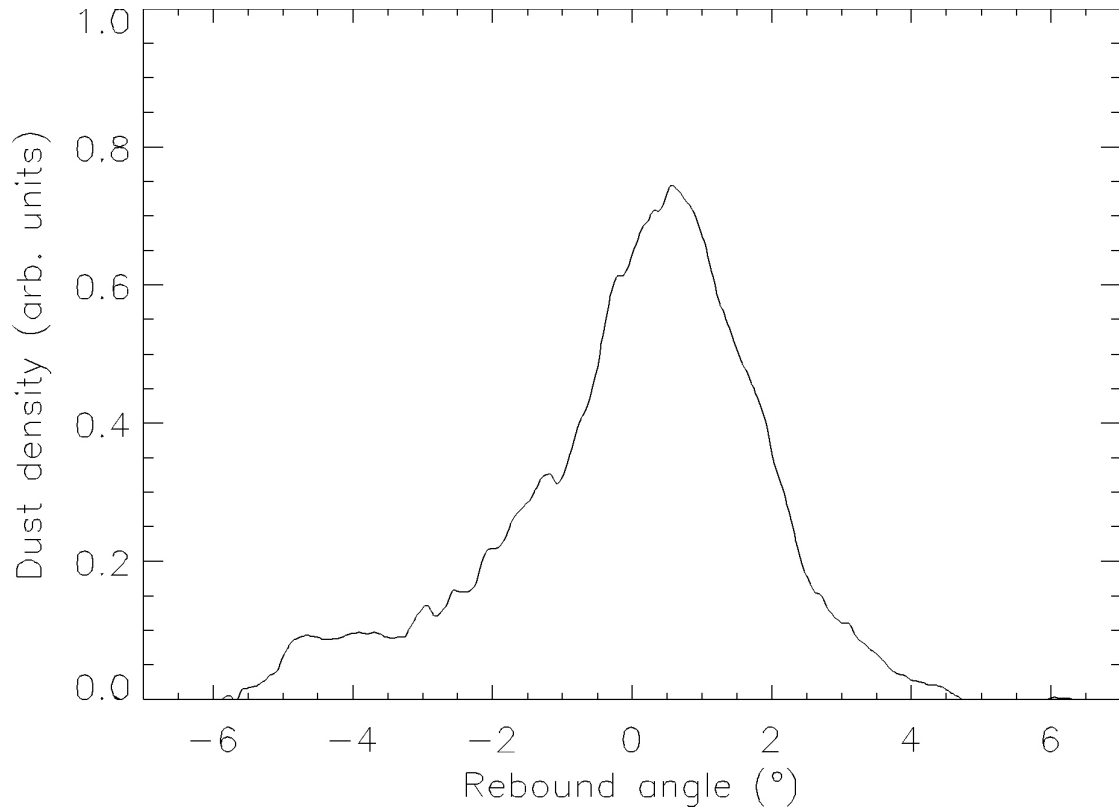
Fig. 3.25 *Distribution of dust particles with height over the plane of impact. The height profile is the sum of intensities (pixel brightness) for a given height averaged over 25 horizontal pixel lines taken from the image in Fig. 3.24. The height has been transformed to angles with respect to the target surface and through the target center, keeping in mind that the actual headings of fragments might be smaller if they do not lift off at the target surface but rather at the upper parts of the pile created by the projectile. We estimate the systematic error of the angular scale to be 1°.*

The ejection angle is a very important parameter, which might determine the fate of the fragments in protoplanetary disks. In Chapter 4 we will see that gas flow through a porous body can return fragments after a collision. To be reaccreted by gas flow a fragment has to stay close to the surface. If ejection angles are extremely small even high speed fragments stay close to the surface and might be reaccreted. Also on a rough target surface such fragments might hit a bump on the target again at high velocities, which leaves more material sticking.

The analysis of the wall fragments assumes that particles hitting the wall are actually sticking there and that no major part is ejected from the walls. However, this is very plausible. No significant amount of dust could be found falling down on a sheet of black paper that was put under the target over the whole chamber cross section. Here, mostly dust is seen that is slowly ejected and falls down close to the target. This slow dust is responsible for numerous parabolas imaged in the laser as seen in Fig. 3.20. The total dust mass of these slow fragments is small (about 10% or less of the projectile mass) for the high speed impacts and increases in mass for the slow impacts where eventually it makes up the entire fragment mass. For the high speed impacts the slow fragment fraction is clearly separated from the fast fraction sticking to the wall and we only consider the high speed fraction here further. The

main impacts onto the target suggest that a large amount of dust should stick to a compact target at velocities of 13*m/s* or higher. For the high speed collisions the fragments reaching the wall still have high velocities though with 9*m/s* the lower limit might be significantly slower. This actually gives another set of data for high velocity impacts of smaller dust aggregates. We note that the wall is a solid surface rather than consisting of dust. Since the main impacts onto the target show that the target material takes part in the collision the impacts onto the wall are fundamentally different.

Particles sticking to the wall unambiguously show sticking without influence of gravity since the dust would fall down otherwise if it was ejected. From earlier experiments we know that aggregates consisting of irregular *µm*-sized particles and grown in a cluster-cluster aggregation process would not stick to the wall above ~3*m/s* velocity (Blum & Wurm 2000). The small dust aggregates hitting the wall thus have to be (more) compact and their sticking behavior can be compared to the collisions of the primary large projectiles. In both cases sticking of a large fraction of the projectile at high velocities occurs. Thus, for projectiles in the range from ~50*µm* (see next subsection about size distribution) to ~1*cm* net growth at collision velocities larger than 9*m/s* ± 1*m/s* or 13*m/s* ± 0.5*m/s* respectively seems possible.

3.3.3.3 Ejecta size distribution

Most of the mass of an ejected dust aggregate, which hits the wall in the high speed collisions sticks there. We could only see a minor amount of dust on the cardboard below. We thus regard it as an appropriate assumption that the sizes of dust aggregates on the wall closely resemble the sizes of ejecta generated in the main impact. For the small and intermediate impact velocities size distributions are not as straightforward to obtain. However, we measured three size distributions of fragments for three successive experiments carried out at velocities above 20*m/s* shown in Fig. 3.26.

Fig. 3.26 Size distribution of fragments for three successive experiments at high

collision velocities. Shown is the number of particles per size bin (dN/ds) over the size of the fragments. A total of 989, 1512, and 847 particles were measured for experiments 68, 69, and 70 respectively. For comparison all size distributions were adjusted in height by a factor (manually chosen iterative) as to qualitatively give the best match with each other. All size distributions essentially follow the same functional behavior. For small particles the size distribution is constant. For larger sizes the size distribution follows a power law with power –5.6 ± 0.2. The transition occurs at a size of about s = 0.5mm. There is a sharp cut-off at 1mm size. Only very few fragments can be found, which are (slightly) larger.

The size distribution has two regimes. For small particles the size distribution is flat and might be described by a constant. For larger particles the size distribution follows a power law with index –5.6 ± 0.2. The transition between both regimes is at about s = 0.5*mm* in size. There is a cut-off for large particle sizes at about 1*mm* for the given impact parameters. Only very few larger fragments are found. As far as the mass is concerned the maximum is at about 550*μm* ± 50*μm*. Thus, the mass of a projectile of 1*cm,* which is redistributed to the dust phase in a protoplanetary disk after a collision, could be found in dust aggregates of more than one order of magnitude smaller in size. This also shows that larger dust particles observed in protoplanetary disks are not necessarily just grown but might be debris particles from collisions of bodies, which are already much larger.

3.3.4 Discussion

It has to be noted that our target size is limited and confined by a solid aluminum tray. If a target of the same size (6*cm*) were used without supporting tray, effects might be visible, which cannot be seen within the tray. For the experiments with highly porous targets, reported in the previous section, effects like ejection of dust at the backside indeed were observed in the drop tower experiments. However, the microgravity experiments also showed that for compact targets no effects can be seen on the backside. It is also thinkable that still smaller compact targets without tray would be cracked or fragmented. Considering, that very compact bodies and the high velocities might only show up in protoplanetary disks for bodies of size much larger than 10*cm* (Weidenschilling & Cuzzi 1993), our supporting tray might be regarded as merely a substitute to simulate the inertial mass of a larger compact body. So far we only see very local effects on the target morphology at the target surface. We thus regard the experiments with compact targets and supporting tray as good analog for targets of larger sizes.

The high speed impacts into targets of different morphology, e.g. for very porous targets (previous section), and compact targets reported here clearly show that the make up of the target is one of the major parameters determining the outcome of a collision. Impacts of the compact type are one possible complementary scenario for subsequent collisions of larger bodies in protoplanetary disks after high speed collisions have compacted the porous dust aggregates more and more.

We can summarize the main results of our experiments as follows:

• If a large compact dust aggregate of *mm-* to *cm*-size collides with a compact target between 13*m/s* and 25*m/s*, the aggregate will partly stick to the target. A fraction of about 50% of the mass will be added to the target on average independent

of the speed as long as it is above the threshold of 13m/s ± 0.5m/s.

• Smaller particles from 50μm to 1mm also stick to a large degree to a solid target above 9m/s ± 1m/s. Probably much more than 50% of the mass is added and the threshold for sticking is shifted a little bit to smaller velocities, compared to the values for larger aggregates. This might be due to the different physics of impacts onto a solid surface compared to impacts onto a dusty surface.

• A projectile of *mm*- to *cm* size colliding with a compact target at speeds below 13m/s ± 0.5m/s will not stick but be ejected or essentially rebound again.

• Fragments in a high speed collision of *mm*- to *cm*-size projectiles at 25m/s typically are one order of magnitude smaller in size. At smaller impact speeds fragments get larger. The fragment size for high speed collisions follows a flat distribution for small particles up to 500μm and a power law with power –5.6 ± 0.2 for larger particles with a cut-off at 1mm.

• Fragments of a high speed collision are fast with 40% ± 10% of the impact velocity or an ejecta velocity coefficient of R = 0.4 ± 0.1. This is much higher than in our low speed collisions or in the low speed collisions by Colwell (2003), where the ejecta speeds are typically below 10% of the impact speed. It is also different from high speed impacts into highly porous targets where ejecta speeds are below 1% of the impact speed (previous section).

• The fragments from a high speed collision at normal incidence are ejected very flat with respect to the target surface at ejection angles below 3°.

With the assumption that these collisions can occur in protoplanetary disks it might be that even though a rather spectacular shower of fragments is observed to be ejected, a net growth of a more massive body in a high velocity impact can immediately occur. This is the first time that net growth in collisions that fast has been observed and studied for dusty bodies (Wurm, Paraskov, & Krauss 2005b).

CHAPTER 4

GAS FLOW THROUGH POROUS DUST AGGREGATES

It is often argued, that growing planetesimals through sticking collisions does not work. Collision velocities in protoplanetary disks can reach more than 60*m/s* (Sekiya & Takeda 2003). Our recent impact experiments (presented in Chapters 3) have shown that planetesimal growth by mutual sticking collisions at high collision velocities is possible. But we have also observed that the growth was accompanied by fragmentation. In some impacts at 25*m/s* more than 50% from the projectile was fragmented and initially not sticking to the target. Even if larger bodies in protoplanetary disks grow in collisions of smaller dust bodies, fragmentation is very likely an unavoidable process.

We consider here a slightly more sophisticated growth model as a refinement. Assuming that meter-size bodies can grow, gas drag might still continue to aid in growing even larger bodies if we introduce the concept of the porosity of an object to the gas flow around, or rather, through it.

Porous flow seems to be a common field of study for engineers, hydrologists, and geologists, since, e.g., it determines the flow of water, oil, and gas in Earth's surface layers (Bear 1972). It is also of importance in describing phenomena related to comets (e.g., Skorov et al. 2001; Grün et al. 1993). However, as far as we know, the concept has never been applied to planet formation. Our calculations based on the physics of porous flows, which are outlined below, suggest that a porous flow might be one more leap forward to close the gap between 1*m* and 1*km* for the growth of planetesimals (Wurm, Paraskov, & Krauss 2004).

4.1 Flow through a porous medium

There is little doubt that growing planetesimals are very porous. Even the most compact aggregates to build the first generation of planetesimals have porosities of 67% (Chapter 3). Most likely they are typically much more porous up to more than 90% initially (Blum 2004). This inevitably means that there is a gas flow through these bodies if they are subject to an external gas flow. The body that we consider here is the larger of two bodies colliding with each other. In view of the fragments originating from its surface, we term it the "parent body" of the fragments, including even fragments of the smaller projectile.

The flow of gas through a porous object can be described by Darcy's law,

$$q = -\frac{k}{\mu}\nabla p, \tag{4.1}$$

where q is the flow velocity, k is the permeability of the object, μ is the viscosity of the gas, and p is the gas pressure. The pressure gradient depends in detail on the shape of the body. For simplicity, we treat a growing body as spherical with radius R for the moment. The pressure difference between the front side of a sphere that faces a gas flow and the back side can be expressed as

$$p_v = C_D \frac{\rho}{2} v^2 \,, \tag{4.2}$$

where C_D is the drag coefficient, v is the velocity of the free flow with respect to the body, and ρ is the density of the gas. As the pressure gradient, we take

$$\Delta p = \frac{p_v}{(4/3)R} \,, \tag{4.3}$$

which is the pressure drop over the thickness of the body. It has to be noted that with respect to a given flow direction, a spherical body is thicker in the center than at the edges. The gas flow through the edges will be much faster than the gas flow through the center. Thus, more gas can flow through this outer rim. To account for the change in thickness of the sphere, we calculate an average thickness by considering the thickness of a cylindrical body with the same circular cross section and the same volume as the sphere. This gives the factor of 4/3 instead of 2 in equation (4.3).

For the permeability k we refer to simulations by Cancelliere et al. (1990). They simulate the permeability of a medium of overlapping spheres. Koponen, Kataja, & Timonen (1997) carried out similar simulations for rectangular shaped obstacles. Either way, the permeability can be expressed as

$$k = c_k r^2 \,, \tag{4.4}$$

where r is the so called hydraulic radius. In the case of spherical constituent particles, r is the radius of these spheres. c_k is a dimensionless permeability, which depends on the porosity of the body. An effect that has to be considered at low pressure is slip flow, which for porous bodies is sometimes called the Klinkenberg effect (Bear 1972; Klinkenberg 1941). As the gas pressure under consideration is very low and the mean free path of the molecules is larger than the pores, the permeability has to be modified by a factor. The permeability is then given by

$$k_p = k(1 + 4Kn) \,, \tag{4.5}$$

where Kn is a dimensionless number, the so called Knudsen number (eq. 2.6). Kn is defined here as the ratio of the mean free path of the gas molecules to the pore size of the dusty body. Permeability is certainly one major aspect that has to be considered in more detail in the future. However, because of the lack of knowledge about the inner morphology of the growing bodies, we regard the given description as sufficient for the model presented here. Putting equations (4.2)–(4.5) together in equation (4.1), we get the flow velocity

$$q = -\frac{3}{8} \frac{c_k r^2}{\mu} (1 + 4Kn) \frac{C_D \rho v^2}{R} \,. \tag{4.6}$$

From experiments as well as simulations, Blum et al. (2000) suggest porosities Φ for growing bodies of 80% and more. With this porosity we get $c_k \approx 1$ (Cancelliere et al. 1990; Koponen, Kataja, & Timonen 1997). For the disk parameters, we take values from Sekiya & Takeda (2003) that refer to the minimum-mass nebula by Hayashi,

Nakazawa, & Nakagawa (1985). The gas density is given by $\rho = 1.4$ x $10^{-6} kg/m^3$ at 1AU. The mean free path of the gas molecules at $1AU$ is $\lambda = 0.01\ m$. For the free flow velocity v, we use $60m/s$.

For a spherical body, the drag coefficient C_D depends on the Reynolds number Re. For an $R = 1m$ body at a $1AU$ distance, the Reynolds number is 15. The corresponding drag coefficient is $C_D = 5$. For viscosity we take the usual value of $\mu = 1.0$ x $10^{-5} Pa\ s$. The smallest particles of interstellar origin are smaller than $1\mu m$. However, half of the material found in primitive meteorites is millimeter-size chondrules. Here, we assume $r = 1mm$. It should be noted that this does not necessarily mean that the particles have to be individual solid particles (e.g., chondrules) of that size. Dense agglomerations of much smaller particles will probably work as well and serve the same purpose as do large solid units for an otherwise porous body. On one hand, e.g., impacts might create such dense agglomerations, while on the other hand, the recollection of fragments would rebuild very porous parts. Dilatancy as indicated by the impact experiments into porous targets and found in the drop tower experiments (not reported here) would also shape larger pores. A real mixture of chondrules and (sub-) micron-size dust particles might be plausible as well. Therefore, although we consider micron-size fragments below, we still consider this to be selfconsistent with assuming $r = 1mm$ here.

Placing all these values into equation (4.6), we get a flow velocity of $q = 0.04m/s$. This is a small number compared to the velocity of the undisturbed gas flow of $v = 60m/s$. As is shown below, it might nevertheless be very effective.

4.2 Reaccretion layer, limiting tube streamline

Gas flow through a porous body results in a reaccretion layer in front of the body, in which the gas motion is (slow but) directed toward the surface. No matter how slow this flow is, a fragment of a collision that is stuck in the reaccretion layer will inevitably return to the parent body if this is the only motion forced on the fragment. Therefore we call it reaccretion layer. The collision velocity of the second collision will approximately be the flow velocity. Since this is small, even a somewhat larger fragment will stick. No more rebounds need to decrease the collision velocity further in order for sticking to occur. The continuous rebuilding of a very porous body will thus be self-perpetuating.

If a fragment leaves the reaccretion layer, the flow will carry it around, and the particle will be lost. Therefore, it is important to know how thick the reaccretion layer might be. We know that gas is flowing through the body and that the velocity of this flow on average is given as $q = 0.04m/s$ for a $1m$ body. For reasons of mass conservation, the volumetric flow through the body has to equal a certain part of the free flow. Streamlines that surround the body cannot cross each other. Thus, the flow through the (spherical) body has to originate in a cylinder centered over the front side (see Fig. 4.1).
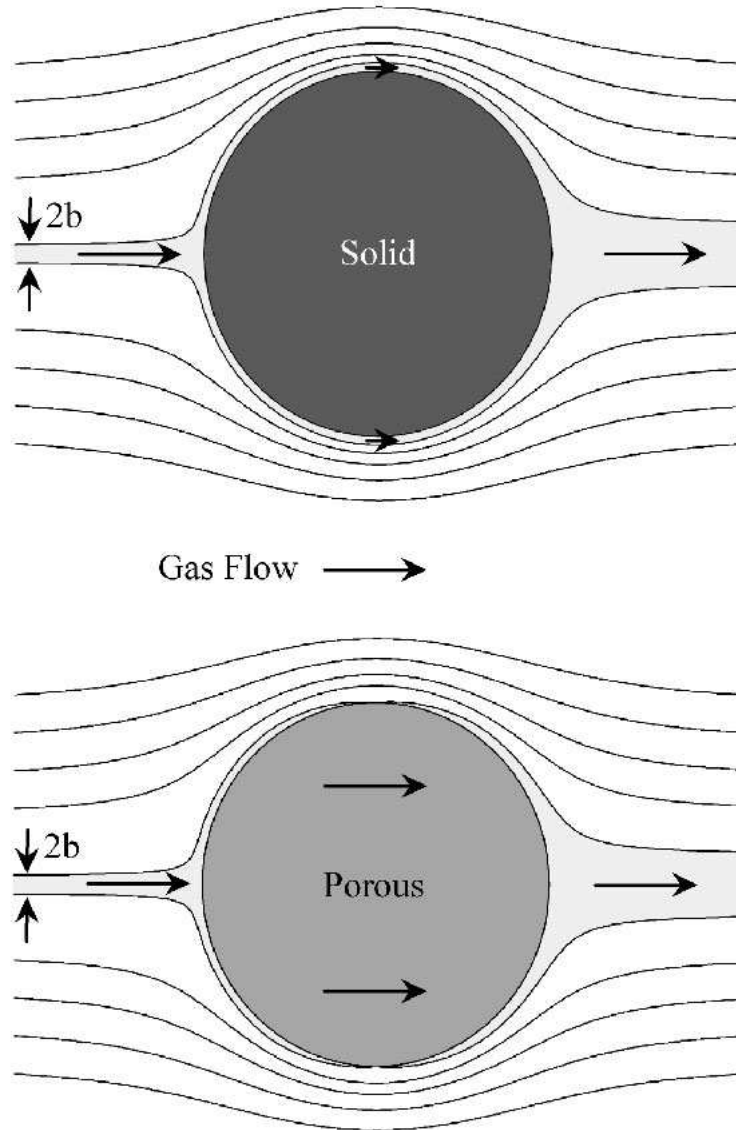
Fig. 4.1 Gas flow around porous and nonporous bodies. Comparison between the gas flow around a nonporous (solid) and a porous sphere. This sketch is for illustrative purposes only. It is not on scale and should not be taken quantitatively. The part of the gas that flows through the body is shaded light grey. On the front side, this region is equivalent to the reaccretion layer. Sufficiently far away from the surface, the region marks a cylindrical part of the flow with radius b. As outlined in the text, this is also an estimate for the thickness of the reaccretion layer.

As the flow approaches the body, it gets wider until it covers the whole front side of the sphere. As mentioned before, mass conservation requires that the volumetric flows be the same. The radius of the cylindrical part of the free flow, *b* (see Fig. 4.1), is

$$b = R\sqrt{\frac{q}{v}} \qquad (4.7)$$

The free flow has a speed of $v = 60 m/s$. The flow through the body is $q = 0.04 m/s$. For

$R = 1m$, this yields $b \approx 0.03m$. To estimate the thickness of the reaccretion layer, one might consider a streamline on the surface of the cylinder and how close this streamline would pass to a nonporous sphere. Streamlines get somewhat compressed as they pass an obstacle. Therefore, as can be seen in e.g., the figures shown in Sekiya & Takeda (2003), the nearest point of the limiting tube streamline (for the porous body) is a little closer to the surface (in the non porous case) than is the radius of the cylinder. This is also consistent with flow patterns around bodies of different shapes, such as plates. However, there is already a net growth if the mechanism works on a sufficiently large impact area. Considering the fact that the reaccretion layer is thicker in the center of the front side of the body, a plausible estimate for the thickness of the reaccretion layer is thus the radius of the cylinder with the same volumetric flow. Therefore, we get a reaccretion layer thickness $b = 0.03m$. We note that this is only a first estimate. It might be worthwhile to visualize the thickness of this reaccretion layer in comparison to a body $1m$ in radius. Being $\approx 1\%$ of the size of the body, it is very thin.

4.3 Ejecta trajectories

We assume a small compound dusty aggregate (projectile) that collides with a larger parent body (target). The projectile is assumed to fragment into much smaller pieces. In addition, parts of the target are eroded. At high impact speeds, a total mass in fragments larger than the projectile mass is ejected from the surface (Blum & Wurm 2000; Wurm, Blum & Colwell 2001a, 2001b; Colwell 2003).

To see the response of a fragment to the gas flow, we calculate fragment trajectories for different parameters. Here we assume the front of the parent body to be a plane and, in general, assume a fragment from the collision to be ejected at a 45° angle to the plane. We consider a vertical straight gas flow with velocity q toward the plane. For different flow speeds, q, gas grain friction times, τ_f, and rebound (ejection) speeds, v_{reb}, we calculate the maximum height of the fragments above the plane and the distance from the ejection point, at which the fragment hits the plane again. These two values approximate the necessary height of the reaccretion layer and the minimum size of the body (e.g., see Fig. 4.2). The motion for the given case is, e.g., given by (Wurm, Blum & Colwell 2001b)

$$x = v_{reb} \sin(\alpha) \tau_f (1 - e^{-t/\tau_f}), \tag{4.8}$$

$$y = [v_{reb} \cos(\alpha) - q] \tau_f (1 - e^{-t/\tau_f}) - qt \tag{4.9}$$

The distance from the ejection point along the plane of the body is denoted by x. The height above the plane is y. The time is given by t. The initial angle with respect to the y-axis is given by α. Two example trajectories can be seen in Fig. 4.2.
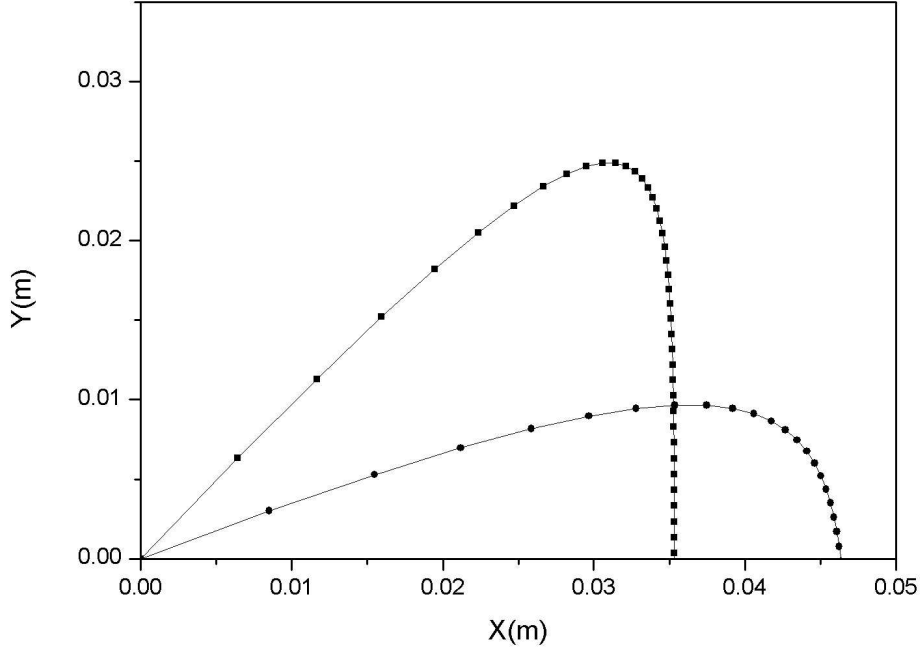
Fig. 4.2 *Trajectories of particles that are subject to a gas flow of q = 0.05m/s. Initial speeds are v_{reb} = 0.5m/s. Gas-grain friction times are τ_f = 0.1s. Points are equally spaced, with an interval of 0.02s. The upper curve corresponds to an initial heading of 45°, and the lower curve to 20°, from the x-axis. The flow is directed in the negative y-direction. The x-axis marks the surface of the body. Note that the particles are essentially stopped first before the flow slowly returns them to the parent body.*

For the given parameters (ratio between the porous flow and the rebound velocity ≤1), a particle is stopped before it slowly returns to the target. The data points in Fig. 4.2 are at equal time intervals. For the calculations, we assume a flow velocity of $q = 0.05m/s$. However, it turns out that the actual number for the flow velocity is of minor importance, as long as it is smaller than or comparable to the rebound velocity. The turnover points of the trajectories in Fig. 4.2 shift only slightly for different flow velocities. Fig. 4.3 shows the maximum heights and widths for different particle trajectories. The value for a typical $1\mu m$ dust particle is marked by a star. In the disk model considered above the particle's friction time is $\tau_f = 0.1s$. For the rebound velocity, we take $v_{reb} = 0.5m/s$, which is approximately 1% of the impact velocity of a small body. It should be noted that compared to solid-solid collisions, in which rebound velocities of several tens of percent are common, the value given here looks rather low. However, for very inelastic collisions with dusty bodies, experiments (including ours) indicate that 1% is a typical number (Colwell 2003; Wurm, Paraskov, & Krauss 2005a, Chapter 3.2). Values of height and width for other parameters are also shown in Fig. 4.3.

There will likely be a distribution of ejecta velocities, so that some particles may be lost through the reaccretion layer while others are returned to the parent body. Understanding the ejecta velocity distribution, and whether it is correlated to particle size, is therefore critical in determining the efficiency of this mechanism.
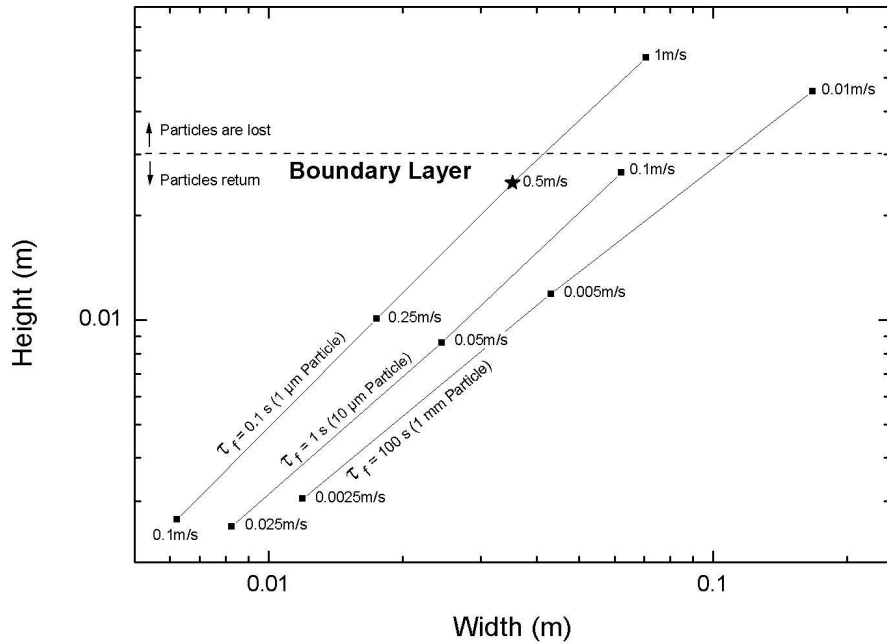
Fig. 4.3 *Calculated widths and maximum heights of trajectories for a flow velocity of q = 0.05m/s for particles ejected from a plane surface at a 45° angle (see Fig. 4.2). Each data point corresponds to a pair of numbers, the initial particle velocity and the gas-grain friction time. The initial parameters are labeled individually next to the data points. Data points with the same gas grain friction time are connected by lines. For a given dust density (amount of material) at a given gas density, the friction times are related to a certain particle size. Approximate sizes for silicate-like particles are given in brackets next to the friction times. An initial size frequently used in protoplanetary disks is 1μm. If such a particle were ejected after a collision with approximately 1% of the impact speed in a typical model disk, the value marked with a star in the plot would result. As can be seen, the height is within the reaccretion layer (dashed line). Particles within the reaccretion layer (below the dashed line) will return to the target. Particles above the line will be swept away by the gas flow and be lost. For particles that are aggregates of smaller particles, the sizes labeled on the lines have to be increased, since friction times for aggregates can be significantly lower than for compact particles.*

4.4 Discussion

One first thing to note is that trajectories are only slightly influenced by the actual flow velocities. The calculations show that only for the faster flows that are comparable in speed to the speed of an ejected particle does the maximum height above the plane change slightly, while the influence on the width of the trajectory can be neglected in all cases.

A dust particle that we consider as typical will return to the target only 3.5*cm* away from its impact/ejection point and it will gain a maximum height over the surface of only 2.5*cm*. This is the highlighted data point (*star*) in Fig. 4.3. The width of the trajectory is much smaller than the size of the body. Therefore, the width is not critical with respect to missing the parent body. More important, however, is that the

maximum height can be smaller than the reaccretion layer thickness calculated above. The calculations therefore indicate that the particle would indeed return to its parent body.

Thus, it is possible that a body of $1m$ in size can still grow in mass. As the body grows, the flow velocity q will decrease, as can be seen from equation (4.6). Besides the direct dependence of q on R, the drag coefficient C_D will also decrease slightly less than linearly with R. However, according to equation (4.7), the reaccretion layer thickness will stay more or less constant or even increase slightly at the same time. Therefore, if an $R = 1m$ body can grow, so can a 10 or $100m$ body. Changes in the flow pattern at increasing Reynolds numbers would probably have to be considered.

Our calculations are restricted to laminar flow thus far. If the disk itself is turbulent, the mechanism might still work. On average, turbulence probably increases the gas flow velocity v. Therefore, the flow velocity q and the reaccretion layer thickness b would increase (equations (4.6) and (4.7)). If the fraction of impact energy that is dissipated decreases with increasing impact velocity, reaccretion might work even better, but this needs further study. If turbulent eddies were much smaller than the large target body, the dynamics of the gas flow would change, and the details of the particle motion close to the target would very likely look different. However, in the next Chapter we will discuss that in a turbulent protoplanetary disks a smallest size scale for eddies exists. The smallest eddies at $1AU$ distance from the star are typically $1km$ in size. Therefore, the flow around a $1m$ body might locally be regarded as laminar even in turbulent disks.

Nonsphericity of the growing bodies would also influence the gas flow and thus the outcome of a collision. If the target, e.g., has thin extensions or bumps, these might be of minor resistance to the gas and might reach into heights above the reaccretion layer. These would catch particles that would otherwise be lost. On the other hand, crater-like pockets might not be reached by the main gas flow and might act like lee sites, while there is still flow through the body. This would effectively increase the height of the reaccretion layer, and ejected particles would return more easily into the crater. The mechanism thus will probably work better for nonspherical bodies.

One more parameter which influences the reacreation of fragments is the ejection angle. In the impact experiments with compact targets reported in Chapter 3 approximately 50% of the projectile mass was ejected after the impact. The ejected particles have a very flat ejection angle (lower than 3° with respect to the target plane). These particles stay close to the surface and can be reaccreted easily by the gas flow. If the ejection angles are extremely small even high speed fragments stay close to the surface and might be reaccreted. Also on a rough target surface such fragments might hit a bump on the target again at high velocities, which leaves more material sticking. In recent experiments Blum and coworkers find (personal communication) that such small ejection angles might also be typical also for porous dust aggregates colliding at much lower velocities (less than a few m/s). The lower impact velocities result in lower ejection velocities (cm/s), which benefit the sticking of the particles to the target surface in secondary collisions.

The model is moderate in the sense of assuming a minimum disk mass. Higher masses and therefore higher gas pressures would be beneficial for the mechanism. The flow velocity would increase as a pressure, at which the mean free path of the molecules is on the order of the pore size is reached (see equation (4.6)), but even if the flow velocity would not change significantly otherwise, an increase in pressure

would induce a linear decrease in gas-grain friction times. Our calculations show that this would also reduce the maximum heights and widths of trajectories approximately linearly. Even fragments ejected faster would then be confined to the reaccretion layer and return to the parent body. This would increase the recollection efficiency of the mechanism.

It has to be anticipated that simple models cannot account for the growth of planetesimals from dust, which spans more than 9 orders of magnitude in size. Refinements are mandatory along the way. However, our calculations for rather typical and, in some respects, moderate model parameters show that the growth of planetesimals in collisions aided by gas drag is one likely ingredient. Therefore, with the modification of taking porosity into account, the basic idea of planetesimal growth is strongly supported (Wurm, Paraskov, & Krauss 2004).

CHAPTER 5

EOLIAN EROSION OF DUSTY BODIES

In Chapter 2 we discussed the similarities between the eolian erosion on Mars and in the protoplanetary disks. Nevertheless there are also basic differences. Wind eroding a dust or sand surface on Mars is turbulent on small scales. Experiments in wind tunnels usually take care to have a fully developed turbulent flow (Bagnold 1954). Protoplanetary disks might be laminar or turbulent depending on the place and time. We consider laminar flows here for several reasons. The experiments reported below are carried out for dust aggregates up to about $1dm$ in size and are immediately applicable to bodies of this size. In turbulence, energy is dissipated most efficiently by smaller eddies. Thus, a smallest size scale exists. In turbulent protoplanetary disks this is about a factor 10^{-7} smaller than the largest eddy (Supulver & Lin 2000). The largest eddy in turn is essentially determined by the scale height of a protoplanetary disk. Thus, if we assume a typical scale height of $0.1AU$ at $1AU$ distance from the star, the smallest eddies are $1km$. Therefore, the flow around a small dusty object might locally be regarded as laminar even in turbulent disks and our results are immediately applicable to small objects in protoplanetary disks.

As to continue the list of differences to Mars bound erosion, a major mechanism for motion of solids by wind on planets with atmosphere is saltation (Bagnold 1954). A large particle that is lifted only jumps a certain distance and then impacts again onto the surface. This impact elevates new particles and so on. Avalanches of particles are the result providing a constant source of airborne (sand) particles. Such a mechanism would not work on small bodies in space since they only have a negligible self gravity. If a particle is freed by gas drag the same gas flow will inevitably transport the particle away but the process will *not* lead to an avalanche of new particles. Gravity, in general, does not have to be overcome on a forming planetesimal. The role of gravity is replaced by cohesion. Unfortunately, this complicates things since cohesion is a highly complex problem of its own compared to gravity. One possible consequence of the role of cohesion is that eolian erosion might be an effective selection mechanism to promote survival of more sticky dusty bodies.

In contrast to Mars material lifted from a planetesimal does not return and is lost for the planetesimal. It has to be noted that the lift happens in different regions than the reaccretion layer discussed in the last chapter. If planetesimals are loose aggregates of dust and if eolian erosion is a significant process, it eventually destroys planetesimals. To be more quantitative we studied the interaction between gas flow and dusty bodies in protoplanetary disks in more detail. We carried out a series of wind tunnel experiments and numerical calculations, which we report on here (Paraskov, Wurm, & Krauss 2006).

5.1 Experimental setup

A sketch of the experiment setup is shown in Fig. 5.1. The experiments are conducted in a circular closed wind tunnel with a pipe diameter of $32cm$. The overall height is about $2m$, the width is ~$1.5m$. Fig. 5.1 is idealized in the sense that the ring is consisting of curved sections (90°) at the four corners and straight sections in between. The straight section at the top and bottom (test section) is about $50cm$ wide.

The gas flow is generated by a roots pump. The pump provides high flow rates at low pressure. The pressure within the wind tunnel can be adjusted from about $10^{-3}mbar$ to 10mbar. The flow rate of the pump is also adjustable. The maximum gas velocity in the center of the wind tunnel is 100m/s. In the application described here we used a fixed flow rate of 3.14m^3/s or a gas speed *averaged* over the cross section of 39m/s.
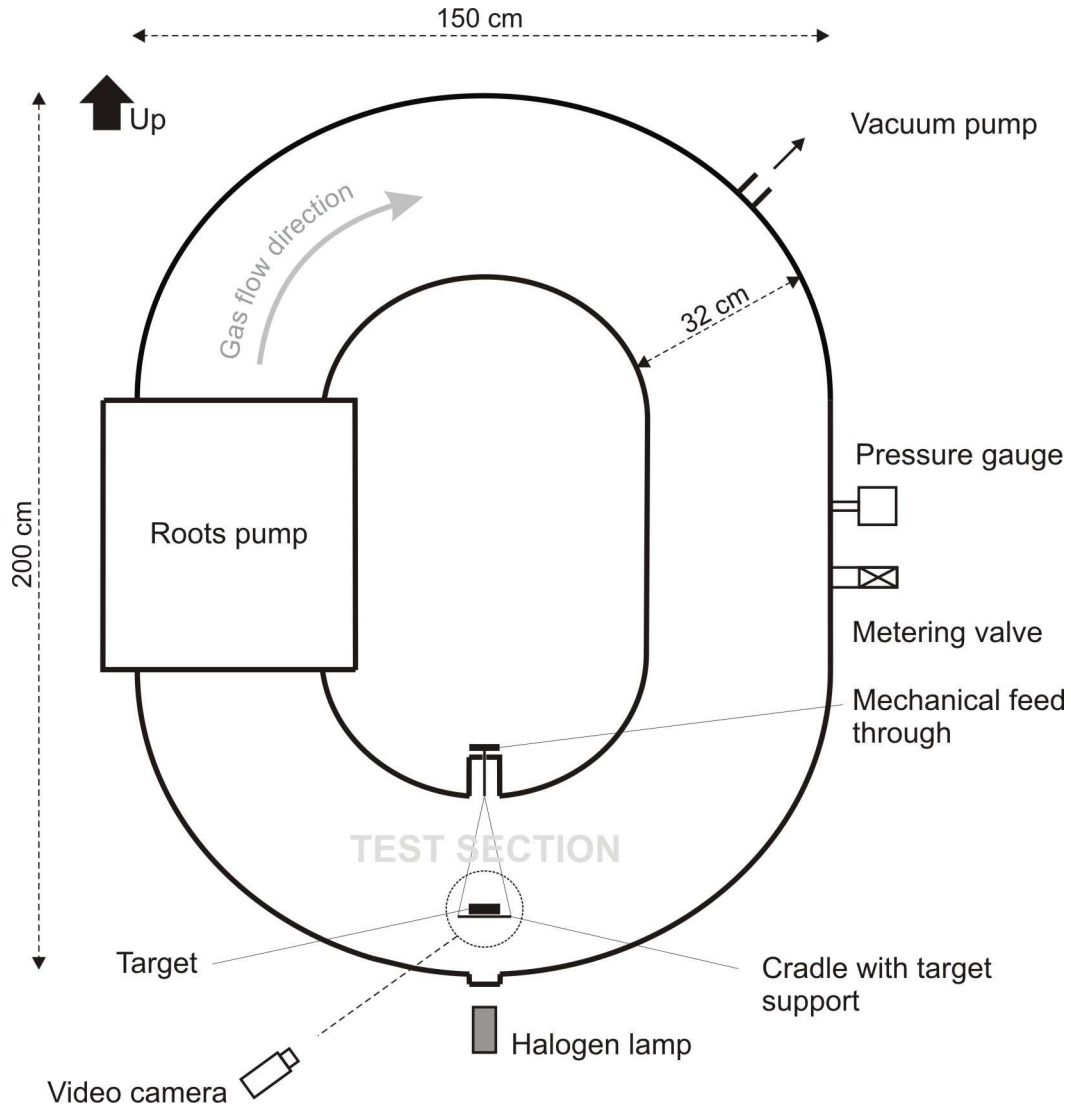
Fig. 5.1 *Sketch of the experiment setup (side view). A dust target is placed in a string cradle in the test section of the wind tunnel. The gas flow is driven by a roots pump. The cradle is adjusted in height by a mechanical feed through. The wind tunnel is 2m high and 1.5m wide. Pressure can be varied from about 10^{-3} to 10mbar. The maximum wind speed can range up to 100m/s but was constantly set to 63m/s for the experiments reported here.*

5.1.1 Gas flow in the wind tunnel

The gas flow in the wind tunnel is not homogeneously distributed throughout the cross section. To quantify the spatial distribution of the gas flow we measured the velocity profile across the center of the wind tunnel in the test section in vertical direction. As indicated in Fig. 5.1 the test section is the lower part of the wind tunnel.

The velocity profile can be seen in Fig. 5.2. These measurements were obtained at a static pressure of $p_{stat} = 0.0165 mbar$ ($\pm 0.0015 mbar$) by observing the deflection of a pendulum. As pendulum we used a paper sphere of $10mm$ diameter with a mass of $190mg$. The drag force on the sphere is given by

$$F_D = \frac{C_D \rho v^2 \pi r^2}{2 C_{Kn}}$$ (5.1)

Here ρ is the gas density, v is the gas velocity, r is the sphere radius and C_D is the drag coefficient. C_D depends on the Reynolds number Re, and for intermediate Reynolds numbers can be approximated by (Crowe et al. 1998)

$$C_D = \frac{24(1 + 0.15 \, Re^{0.687})}{Re}$$ (5.2)

C_{Kn} in equation (5.1) is the Cunningham correction factor for rarefied gas flow and can be expressed as

$$C_{Kn} = 1 + Kn \left(\lambda_1 + \lambda_2 e^{-\frac{\lambda_3}{Kn}} \right)$$ (5.3)

where the Knudsen number Kn is the ratio of the mean free path of the gas molecules to the sphere radius, and $\lambda_1 = 1.231$, $\lambda_2 = 0.470$, and $\lambda_3 = 1.178$ are empirical constants (Hutchins et al. 1995).

The mean gas velocity obtained from the measured velocity profile is 39.5 ($\pm$ 2.0)m/s, which is in excellent agreement with the average gas speed of $39m/s$ calculated from the flow rate. It has to be noted that there are vertical extrusions (flanges) at the top and bottom in the test section which explain that the velocity does not drop to 0 at $0cm$ or $32cm$ height which otherwise is coincident with the walls. The maximum velocity is $63m/s$.

The measurements show that the maximum gas velocity is located below the tunnel center, where it stays almost constant over a height of several cm. The targets were placed inside this zone of constant gas velocity. We regard the results as equivalent to a target in an unbound system with a wind speed at infinity of $63m/s$. The presence of the target in the confined tunnel influences the overall gas flow in the test section. Also the velocity profile changes somewhat as some of the experiments were carried out at a higher gas pressure. However, within the scheme of this work we consider this to be of minor importance.

As outlined above, it is an important difference whether the gas flow is laminar or turbulent. Turbulent flow (in the experiments) might lead to locally varying drag forces on particles which might remove dust from the surface of a body differently from a laminar flow. The flow regime can be estimated by the Reynolds number which for a tube is given as

$$Re = \frac{v_m \rho d}{\eta},$$ (5.4)

where in our case $v_m = 39m/s$ is the mean fluid velocity, $d = 32cm$ is the tube diameter

and $\eta = 1.84 \times 10^{-5} Pa \cdot s$ is the dynamic viscosity of air. It is ρ the mass density of the gas which is the only parameter varied in our experiments as we adjust the static pressure p_{stat}. The onset of turbulent flow in tubes occurs at approximately $Re_{krit} \approx$ 2300. Fully developed turbulence is only expected for Reynolds numbers larger than $Re \sim 10.000$. The critical value Re_{krit} is reached in our experiments at $p_{stat} = 2.9mbar$. We varied the pressure in the range between 0.1 to 4.5$mbar$ and the highest Reynolds numbers were $Re = 3645$. This is still far from being a fully developed turbulent flow. While the gas flow at the highest pressures used probably is no longer perfectly stationary, we still regard it to be close to the laminar conditions locally at the position and size of the target. As seen in section 5.2 erosion thresholds are already reached at pressures of 2mbar so turbulence is not of major concern here and we regard the full range of experiments as analog to a small body moving in a laminar protoplanetary disk.
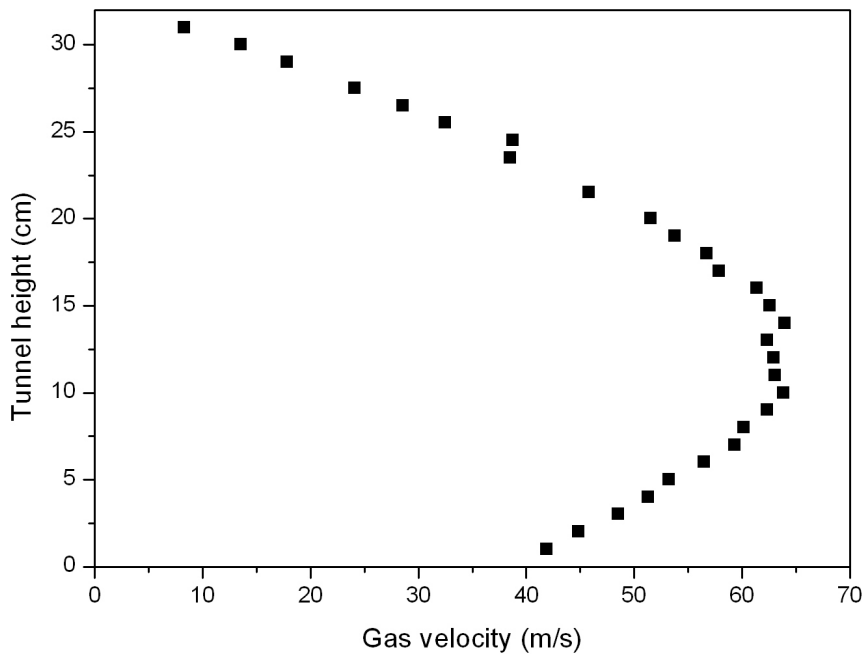
Fig. 5.2 *Gas velocity profile measured at a static pressure of $p_{stat} = 0.0165mbar$. The wind tunnel is divided in 1cm thick layers. For each layer the gas velocity is measured by the deflection of a 10mm diameter paper sphere. Errors of the velocity measurements, mostly due to the static pressure uncertainties, are below 5%. The dust targets were placed inside the zone of highest flow velocity.*

5.1.2 Dust targets

As dust sample we chose a commercial SiO_2 powder with a broad size distribution which we have used before in the impact experiments described above (Wurm et al. 2005a, 2005b). The targets were prepared by manually sieving the dust through a mesh with approximately 500μm openings. Thus, the targets consisted of individual, rather compact dust granules which were up to 500μm in size and sticked loosely together by cohesion forces.

Three different target shapes were used in the experiments: piles, cuboids and spheres. The piles were cone shaped with $\sim$ 50mm base diameter and $\sim$ 15mm height

(Fig. 5.3a) and were placed on a plastic half sphere of 80*mm* diameter. The cuboids had a base of ~ 30*mm* x 50*mm* and heights of 6*mm*, 9*mm* and 12*mm* (Fig. 5.3b). They were placed on a 3*mm* thick metal plate. These two target types had rough granular surfaces. Their average porosity was about 84% (± 2%) (Wurm et al. 2005a). The dust half spheres had 80*mm* diameter. The dust half spheres were placed on 80*mm* plastic half spheres (Fig. 5.3c). Their internal structure was also granular. However, with the same porosity as for piles and cuboids the spheres were too large to be stable and broke up due to their own weight. In order to avoid this, they were very slightly compressed. Their porosity was still about 80%. The cohesion for these compressed dust half spheres was strong enough to support their own weight. With respect to the internal gas flow we regard the permeability of all targets to be similar.

In order to simulate a dust sphere with uncompressed granular dust surface, we also sieved a few layers of dust granules onto some of the compressed spheres. An image of such an aggregate can be seen in Fig. 5.3d.
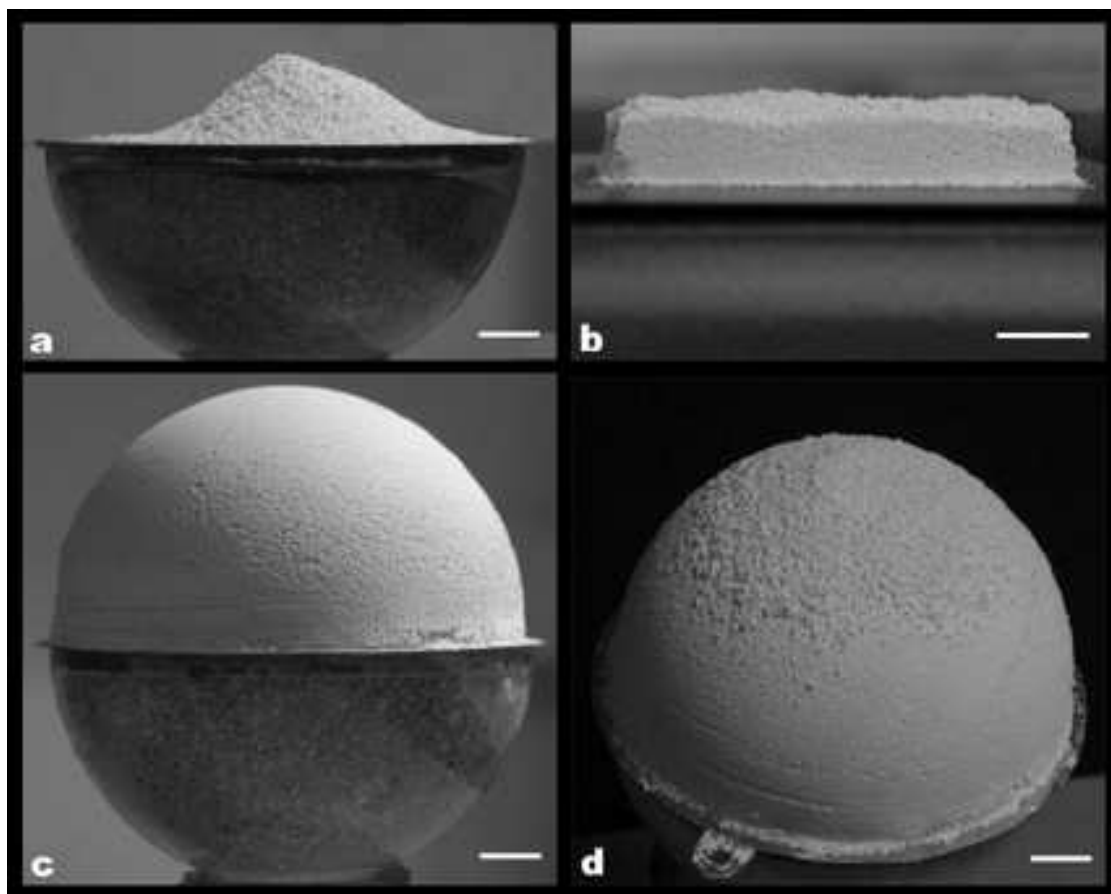
Fig. 5.3 Dust aggregates (targets). The scale bar is 1cm. a: Dust pile, 50mm in diameter, 15mm high and consisting of 500μm dust granules loosely sticking to each other. b: Dust cuboids, 50mm long and 30mm wide. For various experiments we used cuboids with 6, 9, or 12mm height. The surface structure was similar to the pile-type targets. c: Dust hemisphere, 80mm in diameter with more compact surface structure. d: Dust hemisphere powdered with thin layer of dust granules.

5.1.3 Experiments description

In the experiments a dust target was placed in the test section of the wind tunnel. It

was free midair supported by a string cradle. The support had no point of contact with the tunnel walls except at the mechanical feed through where the strings are fixed. This target support was needed to avoid vibration effects caused by the roots pump. A digital video camera was used to observe the target. Illumination was provided by a halogen lamp.

Two base parameters were measured during the experiments: the *erosion threshold* and the *erosion rate*. We define erosion threshold as the gas pressure at which, at a default wind speed, the gas drag is strong enough to *continuously* remove dust granules from the target. With erosion rate we denote the dust mass eroded from the target in a certain time at a given gas pressure and at constant gas speed. All experiments were carried out with air at room temperature.

In the first series of experiments we detected at which minimum pressure dust is picked up by the gas flow. A target was placed in the wind tunnel and the tunnel was evacuated to about $10^{-2}mbar$ pressure. The roots pump was started and the wind speed adjusted to ~63m/s (39m/s average gas flow). The air pressure was gradually increased until dust motion from the target was observed.

The erosion rate was measured as follows. Before we placed the target in the wind tunnel, we determined it's mass. The tunnel was evacuated and the roots pump was started. We kept the pump running for a certain time (60min in most experiments) at a given pressure. After that the wind tunnel was slowly filled with air again. The target was removed and weighed a second time.

5.2 Experimental results

5.2.1 Erosion threshold

We measured the erosion threshold for all target types with exception of the cuboid targets.

Piles: Initially, for the pile-type targets (Fig. 5.3a), individual granules got entrained in the gas flow at a pressure of $p_{stat}≈0.4mbar$, but the number of particles strongly decreased with time. Also, a number of particles only moved down the pile without really being entrained in the gas flow. Particles that get entrained in the gas flow are lifted from different positions on the pile surface. As the pressure was further increased, more granules were lifted. No quantitative statements with respect to the erosion threshold can be made for the pile targets at higher pressures since no reliable mass flux can be determined from the video images. An image of the gas flow at about 3mbar and the entrainment of particles are seen in Fig. 5.4.

Powdered spheres: Dust half spheres powdered with a layer of granules (Fig. 5.3d) behaved similar to the piles. Particles are lifted from the whole surface and their motions start at a static pressure of $p_{stat}≈0.2-0.4mbar$.

Compact spheres: We also determined the threshold of particle movement for compact sphere targets without granule coating (Fig. 5.3c). Here, individual particles also leave the target at low pressures (about 0.4$mbar$), but they seem to originate only from cracks on the surface and not from the main intact part of the surface. Otherwise, massive particle motion sets in at 4.5$mbar$.

Fig. 5.4 *Video image of trajectories of dust entrained in the gas flow. The dust pile is placed in a gas flow at 3mbar and 63m/s. The direction of the gas flow is from right to left. Individual trajectories are marked by arrows. The vertical line is one of the strings of the supporting string cradle. The top of the pile is already eroded and therefore the pile is more flat with a less pronounced tip.*

5.2.2 Erosion rate

The erosion rate was measured for the pile- and cuboids-type targets (Fig. 5.3a and 5.3b). We carried out approximately 40 experiments with both types. In the experiments with pile-type targets we varied the pressure between 0.3*mbar* and 4*mbar*, whereas the cuboids have been used only for the pressure range between 2mbar and 4mbar. In most experiments the targets are left for 60*min* in the gas flow.

Low pressure experiments: At the beginning up to 0.7*mbar* the initial erosion rates, as can be seen from Fig. 5.5, are within the limits of the measurements and do not show a significant mass loss with time. Above ~0.7*mbar* the amount of dust eroded increases to a measurable level but does not change systematically up to 1.4*mbar*. The mass loss was between 20*mg/h* and 50*mg/h* and the erosion rate does not show dependence on the increasing gas pressure. The piles do not change their shape.

High pressure experiments: With pressure increase above 2*mbar* the erosion changes its functional behaviour. At about 2*mbar* a strong increase in erosion rate occurs as seen in Fig. 5.6. The erosion rates for the dust piles are certainly well approximated by an exponential increase with pressure, whereas the cuboids results would equally well fit other laws. Here, dust piles were measured for 60*min*, and dust cuboids were measured for 30*min*. The results for the cuboids were scaled by a factor of 1.33 because two subsequent measurements of 30*min* for the same target showed a decrease in erosion in the second run to only 33% of the first run.

In order to study the dependence of the erosion rate on the target surface we changed the target geometry of the cuboids in a few experiments. The target marked as star in Fig. 5.6 was half as long as the other cuboids. It showed the same erosion rate. We also studied the erosion rate variation with height. The measurements on erosion rate of cuboids with different heights showed a strong increase in erosion as the thickness increases. We carried out experiments with 6*mm*, 9*mm* and 12*mm* high cuboids. As the thickness is increased from 6*mm* to 9*mm* the erosion rate increases by a factor 6. Thickness of 12*mm* corresponded to erosion rate increase by a factor 11

compared to erosion rates at *6mm* height.
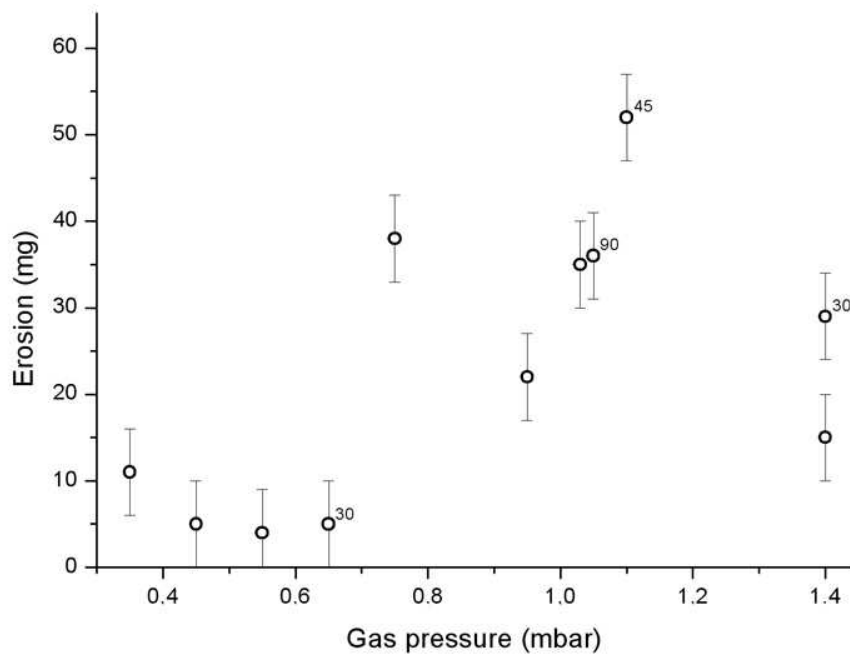
Fig. 5.5 *Measured erosion for dust pile targets up to static pressures of 1.4mbar. Each measurement represents a new target. Most targets were placed in the gas flow for 60min. Except for a few targets that were measured for different times as indicated. The error bars reflect a typical mass difference mostly due to humidity. We estimate the error to be constant 5mg.*
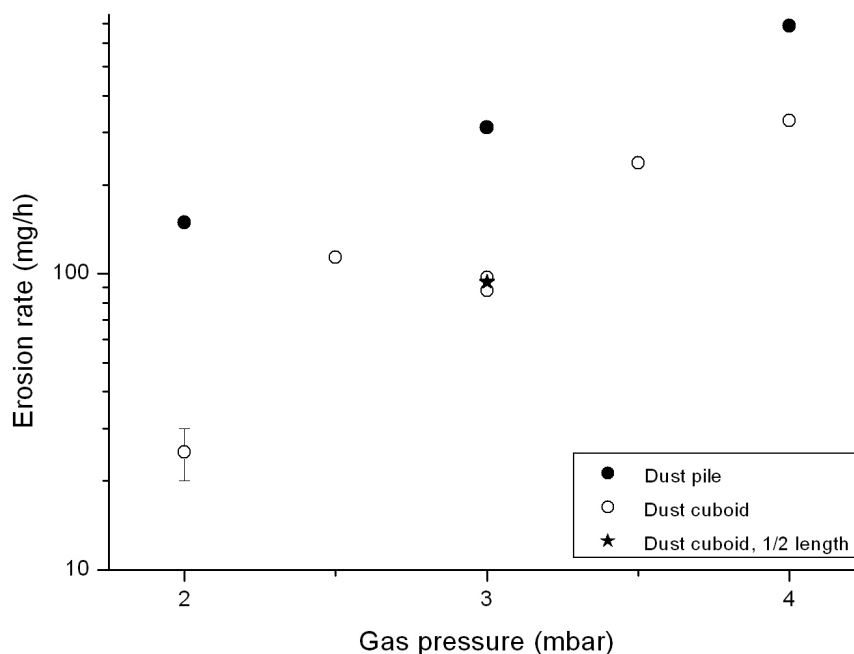
Fig. 5.6 *Erosion rate over gas pressure for piles and cuboids. Filled circles are for piles. Open circles are for cuboids of 50mm length, 30mm width and 12mm height with the short side facing the gas flow. The star symbol at 3mbar marks a cuboid target with half the length, but with the same width.*

5.3 Gas flow numerical calculations

To quantify the gas flow at the surface of our targets we carried out numerical calculations in 2d, using a commercial software package (FEMLAB 2004). Our model consists of a tube section (rectangle) and the target. The tube section is 48*cm* long and 32*cm* wide and corresponds to the test section in our laboratory experiments. The model target is placed in the center of the tube. Initial condition is an inflow at 60*m/s* across the whole inlet side. At low pressure the model results in a speed at the center of the tube (with no target) of 63*m/s*. Therefore, we regard the numerical model as a suitable analog to the experimental conditions described in section 5.1. We note that the velocity profile across the test section in the laboratory experiments and the numerical model are slightly different. Within the numerical limitations and experimental uncertainties of determining the erosion threshold this still allows a quantitative comparison between numerical model and experimental results.

For the numerical model we assume no slip conditions at the walls of the tube though this assumption is not influencing the inner flow much at low pressures. We solve the stationary Navier-Stokes equation within the tube according to (Femlab 2004)

$$\rho\left(u \cdot \nabla\right)u + \nabla p - \eta \nabla^2 u = 0$$

$$\nabla \cdot u = 0.$$
(5.5)

Here, η is the dynamic viscosity, ρ is the air density, p is the static pressure, and u is the velocity field. It is important to note that our dust targets are highly porous and gas flows through them. Within the porous target the flow is modelled by the Brinkman equation according to (Femlab 2004)

$$\frac{\eta}{k}u + \nabla p - \eta \nabla^2 u = 0$$

$$\nabla \cdot u = 0.$$
(5.6)

The permeability of the porous structure is denoted k. As boundary conditions for the target we assume no slip conditions at the solid target support and the pressure to be continuous through the dusty surfaces otherwise. The permeability is given by eq. 2.4 as

$$k = c_k r^2,$$
(5.7)

where r is the typical pore size of the target. According to Cancelliere et al. (1990) we assume $c_k = 1$ at our porosities. At the given high porosities of 84% for the target the pore volume is more than 5 times the volume of solids. Therefore, the pore size will be larger than the typical granule size. As the granule size is about 0.5*mm* we assume a pore size of $r = 1mm$.

Fig. 5.7 shows the simulated flow outside a pile-type target at 2*mbar*. The calculations show that the highest velocity at the target surface is reached at the top of the pile with $v = 25m/s$. As can be seen the flow is laminar. There is a stable stationary eddy in front of the pile. In our laboratory experiments we sometimes observed

particles that lift off on the right (wind side) of the target and move initially towards the gas flow. The closed vortex in front of the pile explains these observations.
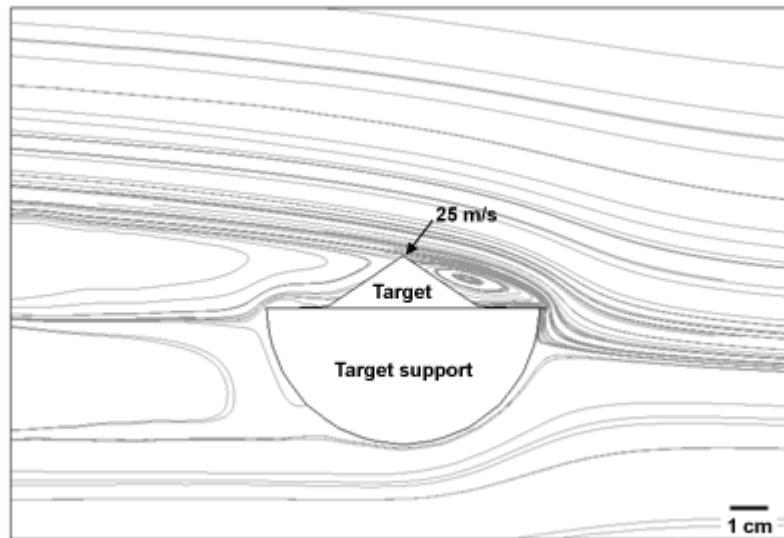
Fig. 5.7 Numerical 2d calculation of the gas flow around (and through) a dust pile. Shown is a streamline plot. In the calculation we use a cross-section through the middle of the target and the target support. We simulated similar conditions as in the experiments: tunnel gas velocity at the target position without target is 63m/s and static gas pressure $p_{stat} = 2mbar$. The arrow marks a streamline which corresponds to $v = 25m/s$ flow velocity at the surface. This is the peak velocity on the target surface entering at the top of the dust pile.
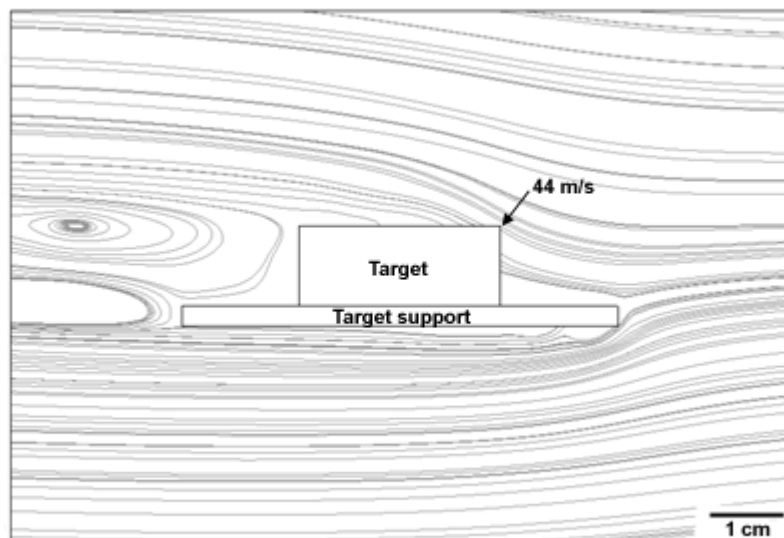
Fig. 5.8 Numerical 2d calculation of the flow around a dust cuboid (streamlines) similar to Fig. 5.7. The plot shows the cross-section through the target and the supporting plate. The calculations use gas velocity of 63m/s and static gas pressure $p_{stat} = 2mbar$. A maximum gas velocity of $v = 44m/s$ is reached on the front top edge of the cuboid and is marked by the arrow.

The numerical calculation in Fig. 5.8 shows the gas flow around a cuboids-type target. At the predefined conditions of $2mbar$ static gas pressure and $63m/s$ initial gas velocity, the calculation results in a laminar flow outside the target. The flow through the $12mm$ high cuboid has a maximum gas velocity on the front edge of the target surface, equal to $v = 44m/s$.

5.4 Discussion of the results

As expected the numerical simulations of the gas flow through a porous dust pile in the previus section result in the highest gas velocity at the tip of the pile. According to equation (5.1) the drag force on a particle should be largest at the top of the pile and particles should be picked up by the gas flow at the top of the pile first. In contrast to that the first particles observed to move in the laboratory experiments (sect. 3.1) are not necessarily originating at the top. Some particles which get entrained in the gas flow are lifted from there but other particles only roll down the pile from different positions on the surface. Several experiments on pile-type targets prepared the same way each time show that these motions start at a static pressure of $p_{stat} \approx 0.4mbar$. We also simulated the gas flow through a pile target at this pressure. According to the numerical simulations the gas flow speed at the top of the target is then $v = 13.5m/s$. If we assume that the topmost particles would be within a free gas stream of velocity v we can calculate the force on a particle according to equation (5.1). Since the Reynolds numbers are below 1 we use $C_D = 24/Re$ instead of equation (5.2). The resulting force on a dust granule of $500\mu m$ in diameter is $F_{gas} = 6 \cdot 10^{-8}N$.

Cohesive forces within dust aggregates can vary in a wide range. The sieved granules with a maximum size of $500\mu m$ in the experiments might be regarded as individual units. On one side they are very compact and dust particles within are strongly sticking together. If we assume a porosity of 70% for the granules, the typical mass is $m = 0.05mg$. On the other side a pile built from these units is just loosely bound since individual granules have only a restricted number of contacts to other granules. If we neglect cohesion, granules will continuously be picked up by the gas flow if the gas drag can compensate gravity, which for the granules used is $F_g = 5 \cdot 10^{-7}N$. At $p_{stat} = 0.4mbar$ gravity is larger than the gas drag force. Obviously the dust granules removed first are not typical dust granules, but rather individuals that are either smaller or more porous than the average, or both. Particles only moving downhill also show that the drag force obviously is not larger than gravity on average. Thus we do not regard the static pressure $p_{stat} \approx 0.4mbar$ as real erosion threshold. This is also in agreement with the fact that the erosion rate does not show significant erosion below $2mbar$ as seen in Fig. 5.5. The erosion rate at pressures between $0.7mbar$ and $1.4mbar$ fluctuates strongly, but we cannot find a clear tendency for erosion increase. A strong increase of the erosion rate occurs first at about $2mbar$. Obviously, up to this pressure there is still a selection effect, which removes particles which are more susceptible to gas drag than the majority of the dust. Thus, we regard the erosion threshold for dust pile targets to be reached at about $2mbar$. The numerical calculations of the gas flow through the pile at $2mbar$ show that at this pressure the gas velocity at the top of the pile is $25m/s$, which corresponds to a gas drag force of $F_{gas} = 1 \cdot 10^{-7}N$. This is still somewhat smaller than the gravitational force on a $500\mu m$ granule. We have to consider that the numerical calculations are only a 2d approximation. A 3d treatment would increase the velocity at the top of the pile. Also the average granule might be somewhat smaller than $500\mu m$, which is only the maximum size (sieve opening) of the particles in our targets. Higher gas velocity and

smaller particles would increase the ratio between gas drag and gravity. An erosion threshold at 2*mbar* is thus plausible. Above 2*mbar* the erosion rates for the dust piles increase exponential with pressure. Obviously the gas drag at these pressures is strong enough to erode all particles on the target surface, regardless of their size.

In the experiments the erosion for cuboids targets above 2*mbar* shows similar behaviour as for the piles (Fig. 5.6). The erosion rate increases strongly with pressure. The numerical simulation of gas flow through cuboids at 2*mbar* shows maximum gas velocities on the top front edge of the target of $v = 44$*m/s* (Fig. 5.8). This velocity corresponds to a gas drag force of $F_{gas} = 3 \cdot 10^{-7} N$. Because our cuboids-type targets have the same cross-section on their whole extent, we regard the 2d calculations as better analogue to 3d calculations. The gas drag is comparable to the gravitational force for a dust granule.

The erosion rate of cuboids showed a significant decrease with time. As mentioned in section 5.2, every second run (30*min*) with a target resulted in an erosion rate of only 33% of the first run. In view of numerical calculations of the gas flow this is plausible though. The height of the target changes upon erosion and the gas flow changes due to shadowing effects by the supporting structure. Numerical calculations of the cuboids in 2d show that the support structure has a significant influence on the gas flow. The calculations also explain the strong increase in erosion rate for 12*mm* high cuboids in comparison with the 6*mm* high cuboids, as the area on top of the target where the flow velocities are large enough to pick up particles changes significantly. Due to the fragile nature of the dust targets the support structure was chosen to be somewhat larger to allow a secure handling and accurate weighing. However, for an unbound cube the erosion rate should be proportional to the target dimensions width and height in a first approximation.

The target marked as star in Fig. 5.6 was only half as long as the other cuboids but shows the same erosion rate. Obviously the target length plays no role for the erosion. This is in agreement with the assumption that gas drag through the front part of the top layer is responsible for erosion. It also proves that saltation is not important here. All particles entrained at the front pass the target and do not return to the target at another position again and do not free new particles.

Certainly as the sizes vary strongly, the Reynolds numbers change and the flow characteristics also vary. At a certain size a dusty object embedded in a laminar flow will produce its own turbulence and erosion rates and thresholds might also change by this. Therefore, it has to be noted that the applicability of our results gets qualitative as we move away from the parameters studied in our experiments. However, in view of the experiments and numerical calculations we find the following:

Erosion threshold: The experiments and calculations suggest that erosion of a dusty surface of a porous body in a laminar gas flow occurs as soon as the gas drag on a surface particle is stronger than the forces keeping the particle attached to its inner neighbours either gravity or cohesion. If a dusty body is 1*dm* in size, consists of compact dust aggregates of about 0.5*mm* in size, and moves through air at about 63*m/s* it starts to get eroded at 2*mbar*.

Our experiments are very different to erosion experiments in turbulent flows. Nevertheless, it is worth to compare the conditions for the erosion threshold we find to the conditions which other researchers find for erosion in turbulent flows over a dusty surface. This gives a qualitative argument how a turbulent flow would change the erosion threshold as follows. Greeley et al. (1980) studied the erosion of a surface

consisting of 212μm diameter walnut shell particles in a turbulent flow. While walnut shell particles are denser than our dust aggregates they are smaller and the gas drag needed to pick up the walnut shell particles should be similar to the gas drag needed to pick up the dust granules which we use. Greeley et al. (1980) find that the threshold to initiate *saltation* on a dusty surface is only depending on the dynamical pressure of the gas flow and is $p_{dyn} = 0.15mbar$, independent of the static gas pressure ranging from $p_{stat} = 4mbar$ to 1000$mbar$. The dynamic pressure is defined as

$$p_{dyn} = \frac{1}{2} \rho v^2 , \qquad (5.8)$$

where v is the free gas velocity, which in our case is 63m/s. For our experiments the dynamic pressure needed to initialize *erosion* is $p_{dyn} = 0.05mbar$. Our dynamic pressure to initiate erosion is a factor 3 smaller than in the work by Greeley et al. (1980) to initiate saltation. It is not clear if both thresholds (for erosion and saltation) can be compared. In general fewer particles are needed to be picked up by saltation to result in erosion due to the avalanche of new particles. It is possible that the particles which lead to saltation rather relate to the first particles in our experiments which get entrained into the gas flow at pressures much below the erosion threshold. In this case turbulent flow would be much less capable of eroding a body in a microgravity environment (without saltation) than a laminar flow.

Erosion rate: Erosion of a cuboid takes place at the front edges. It depends linearly on size as long as the gas flows are similar. If a dusty body is 1dm in size, consists of compact dust aggregates of about 0.5mm in size and moves through air at about 63m/s the erosion rate at the erosion threshold of 2$mbar$ is about 100mg/h.

5.5 Application to protoplanetary disks

Our results can immediately be applied to small bodies in protoplanetary disks moving on circular orbits. The maximum drift velocity in a typical model of the solar nebula is about 60m/s for m-size bodies (Sekiya & Takeda 2003; Weidenschilling & Cuzzi 1993). Our experimental settings were chosen to match these conditions. Erosion in our experiments occurred at 2$mbar$. The drag force (eq. 5.1) depends on the gas density. Since protoplanetary disks consist mostly of hydrogen – we assume a molar mass of 2.34g/mol – the drag force is a factor 12.4 smaller at a given pressure compared to the values for air used in our experiments. Erosion of a small body in a protoplanetary disk would only occur at 25$mbar$. This is on the edge of even the most massive disk models (Papaloizou & Terquem 1999; Wood 2000). Small bodies might lose particles under the most extreme conditions close to the star inside of Mercury's orbit but typically they are safe against erosion.

Protoplanetary disks might be turbulent on a size scale of 1km. As seen in section 5.4 the erosion threshold in turbulent flows over dusty surfaces is higher than in the laminar case. Therefore, even if we would assume that the gas flow on the surface of km-size planetesimals is turbulent, they would be safe against erosion on a circular orbit.

It has to be noted that our dust granules as well as the walnut particles used by Greeley et al. (1980) have rather low cohesion forces. Stronger cohesion of smaller dust particles is e.g. found in wind tunnel experiments by White et al. (1997). Heim et

al. (1999) measured the force necessary to separate two spherical $1\mu m$ particles to be on the order of $10^{-7}N$. According to equation (5.1) the aerodynamic force acting on a dust particle at $25m/s$ and $p_{stat} = 2mbar$ is $6 \cdot 10^{-11}N$. This is orders of magnitude less than the cohesive force and individual dust particles cannot be picked up by the gas flow. Only if the same gas flow acts on a few 1000 dust particles, the total force will be large enough to pick up an aggregate of dust that has just one contact with the underlying surface. Therefore, there is a minimum size of aggregates that can be picked up.

Eccentric orbits: Relative velocities between a solid (dusty) body and the gas strongly increase as soon as the orbits slightly deviate from circular orbits. We have seen in Chapter 2 that an eccentricity of only $e = 0.017$ would accelerate the body to about $500m/s$ relative to the gas at perihelion. The 10 times increase in velocity corresponds to 100 times increase in the drag force on a particle (eq. 5.1). As the drag force at the threshold of erosion remains the same, the gas density or pressure at which a body starts to get eroded is a factor of 100 lower. Above, we estimated the gas pressure at the threshold of erosion of to be $25mbar$ on a circular orbit. On an eccentric orbit it would only be $0.25mbar$. This is given even in the minim mass nebula by Hayashi et al. (1985), where larger pressures are reached inside of $0.3AU$. Therefore, as soon as orbits of planetesimals are only slightly disturbed they easily move faster than the threshold needed to initiate erosion at least at the pericenter of an orbit in the dense part of a disk. Erosion by gas flow is an important mechanism for loosely built dusty planetesimals.

A crude estimate of possible mass loss would be as follows: We consider a cube shaped planetesimal and the mass loss occurring at the edges, thus being proportional to 4 times its length. We further assume that the side of the planetesimal is $1km$ long and that the planetesimal moves with about $600m/s$ through the gas at 1mbar. The drag force (eq. 5.1) depends on the gas velocity squared and linearly on the gas density. The conditions in the protoplanetary disk therefore correspond to results of our laboratory experiments ($60m/s$, air) at $10mbar$ and we apply our measured erosion rates extrapolated to $10mbar$. This is about $1kg/hm$ mass loss or $4000kg/h$ for a $1km$ body. On an Earth orbit, for which 1mbar assumes a rather dense disk model, this is $35 \cdot 10^6 kg$ per orbit, which is 3.5% of the mass of the km dust cube (density $1g/cm^3$). Since we assume erosion to be linear with size but as the total mass varies with the third power, smaller bodies are eroded more efficiently. E.g. a $100m$ size body at otherwise same parameters is eroded within a single orbit.

We note that this is only a very rough estimate. Erosion rates for large bodies might not be scaled 1:1 from our experiments. It also has to be considered that dusty bodies might be more cohesive. If cohesion is stronger by a factor of 10 at the surface, only weak parts get eroded. This might lead to a selection effect where more cohesive dusty bodies survive best. We only assumed a small eccentricity (Earth orbit). Only slightly larger eccentricities would lead to supersonic relative velocities between a body and the gas of up to tens of km/s. How a supersonic gas flow would erode a dusty body is beyond the scope of this paper. If not eroded a body might melt at the surface and get ablated. This has e.g. been considered as possible formation mechanism for chondrules (Genge 2000). However, the dynamic pressure on the surface increases strongly behind a bow shock and it is likely that even very cohesive dusty surfaces are immediately eroded by the gas drag without melting first.

CHAPTER 6

CONCLUSION & OUTLOOK

So far it is often argued, that planetesimals cannot grow through collisions in protoplanetary disks. However, our recent impact experiments, reported here, indicate indisputably that a collision between two dusty bodies at typical (for a protoplanetary disk) velocities can result in net growth of a larger body (Wurm, Paraskov, & Krauss 2005b). With respect to the results from our impact experiments with compact targets, growth might be obviously the immediate result of an impact. But we have seen also that an impact with a more porous target might result in mass loss (Wurm, Paraskov, & Krauss 2005a).

The high speed impacts into targets of different morphology (very porous targets and compact targets) clearly show that the make up of the target is one of the major parameters determining the outcome of a collision. The impacts that we studied here, are only two possible scenarios for collisions in protoplanetary disks. A little variation in target porosity and morphology will probably change the outcome of the impact.

The second major parameter determining the outcome of a collision is the impact velocity. Our experiments showed that higher impact velocites are preferable for the net growth for compact targets. This is remarkable and was completely unexpected. For the compact targets the threshold speed is $13 m/s \pm 0.5 m/s$. A projectile colliding with a compact target at speeds below this threshold will not stick, but be ejected or essentially rebound again. Because of the narrow velocity range in our experiments, we cannot say yet where the upper threshold for the net growth is. Another set of experiments, that will give an answer to this question, is currently in preparation. The new developed set-up at the Institute for Planetology in Münster will further alow to study collisions between dust projectiles and targets up to $100 m/s$.

In our experiments we studied so far only single collisions. It is interesting how the target evolves after many collisions - if several consecutive impacts will lead to a more compact body on average or will crack and subsequently erode the target. This has to be studied eventually in future experiments.

Impacts with porous targets eject more mass than the projectile adds. The amount of fragments might be larger than 10 times the projectile mass. We recently conducted a drop tower campaign, where we studied the same collision in microgravity conditions. The data are currently analyzed and we will publish the results in the near future, but the first impressions are that the results from the microgravity experiments and the ground based experiments are in perfect agreement.

Even if the collisions would indeed be erosive, growth can still ocuur in secondary collisions by reaccreting the ejected dust. In Chapters 2 and 4 we discussed how gas flow can return the ejected particles if they are slow enough. And in fact the ejecta generated in the collisions with porous targets are very slow. Ejecta velocities are typically 0.5% of the impact velocity, or between $0.09 m/s$ and $0.20 m/s$. These velocities are much below the calculated reaccretion threshold (for μm-sized particles $0.50 m/s$). This growth mechanism is not dependent on the target size (large body) and will work also for larger objects, m- and km-sized bodies. The fraction of ejecta mass that is recreated by this mechanism will depend on the porosity of the body, the gas parameters, and the ejecta parameters.

We observed that the net growth in the collisions with a compact target was

also accompanied by fragmentation. In some impacts at $25m/s$ more than 50% from the projectile was fragmented and initially not sticking to the target. The ejecta of a high speed collision are fast with $40 \pm 10\%$ of the impact velocity. It is also different from the impacts into highly porous targets. Nevertheless, also at these conditions the fragments that are small enough could be still recreated by gas flow. The fragments in our experiments are ejected very flat with respect to the target surface at ejection angle below $3°$. Most of the fragments are $500\mu m$ in size or smaller and couple very well to the gas. If the collision takes place in a gas flow, the large body (target) is large enough and still relatively porous, then a large number of the fragments could be recreated to the target surface and stick to it in secondary collisions.

Returning to the application in protoplanetary disks a further comment would be that the fragments that do not stick will feed the dust reservoir of the disk again. Observations of disks a few million years old still show evidence of small dust particles (Beckwith et al. 1990; Haisch et al. 2001). Our results can easily explain the existence of dust particles even after a few million years. It would be possible that half of the mass of solids evolves to planetesimals but the other half stays recycled as dust. This would be a change, which would hardly be noticeable in observations.

The size distribution of solids will strongly depend on the impacts. This will determine the overall growth as part of an ongoing collisional evolution. Details about collisions at different target porosities and for different morphological parameters are needed to be able to model this evolution self consistently. The present work is one step more to provide the necessary parameters for further modeling. There are still numerous parameters which can be changed and which will influence the outcome of a collision. Most important though is that this is the first time that net growth in high-speed collisions has been observed and studied for dusty bodies. If planetesimals do not form any other way quicker their formation by collisional growth is very likely.

We have seen that gas drag and head wind play an important and constructive part for the growth of planetesimals. In Chapter 5 we described a series of wind tunnel experiments. The obtained results show clearly that the gas flow can be also very destructive. If the gas flow is strong enough, the drag could destroy the larger objects formed in an earlier collision growth phase. Dusty objects on circular orbits are not significantly eroded by gas flow independent of the disk model and the distance to the star. This does not apply to dusty objects on eccentric orbits. Because of their higher velocities relative to the gas and the gas pressure increase in the inner parts of the disk, they are almost certainly subject to substantive eolian erosion. For example a $100m$ size body on a slightly eccentric orbit might be destroyed in only one orbit. It has to be noted that these numbers depend strongly on the morphology and the structure of the eroded body, as well as on the gas flow parameters.

These results have strong implications on the evolution of solids in protoplanetary disks. Erosion will redistribute matter from larger objects on eccentric orbits to smaller erosion fragments which can then be added to larger bodies on circular orbits again in collisions. Thus the eolian erosion, together with the later collisions, provides an effective mechanism to recycle material and takes an active part in planet formation. Thereby it leads to the preferential survival of larger bodies on orbits with no or only small eccentricities, at least in the inner part of the early Solar System.

REFERENCES

1. Adams, F., & Lin, D., Transport Processes and the Evolution of Disks, Protostars and Planets III, Univ. of Arizona Press, Tucson, 1993, 721
2. Andre, P., Ward-Thompson, D., & Barsony, M., From Prestellar Cores to Protostars: the Initial Conditions of Star Formation, Protostars and Planets IV, Univ. of Arizona Press, Tucson, 2000, 59
3. Bagnold, R. A., The Physics of Blown Sand and Desert Dunes, Methuen and Co. Ltd., London, 1954
4. Bear, J., Dynamics of Fluids in Porous Media, Elsevier, Dover Publications Inc., New York, 1972
5. Beckwith, S. et al., A Survey for Circumstellar Disks around Young Stellar Objects, Astron. J. 1990, 99, 924
6. Beckwith, S. V. W., Henning, T., & Nakagawa, Y., Dust Properties and Assembly of Large Particles in Protoplanetary Disks, Protostars and Planets IV, Univ. of Arizona Press, Tucson, 2000, 533
7. Blum, J., & Münch, M., Experimental Investigations on Aggregate-Aggregate Collisions in the Early Solar Nebula, Icarus 1993, 106, 151
8. Blum, J., et al., The Brownian Motion of Dust Particles in the Solar Nebula: An Experimental Approach to the Problem of Pre-planetary Dust Aggregation, Icarus 1996, 124, 441
9. Blum, J. & Wurm G., Experiments on Sticking, Restructuring, and Fragmentation of Preplanetary Dust Aggregates, Icarus 2000, 143, 138
10. Blum, J. et al., Growth and Form of Planetary Seedling: Results from a Microgravity Aggregation Experiment, PRL 2000, 85, 2426
11. Blum, J. et al., First Results from the Cosmic Dust Aggregation Experiment CODAG, Adv. Space Res. 2002, 29, 497
12. Blum, J., Astrophysics of Dust, ASP Conference Series, ASP, San Francisco, 2004, 309, 369
13. Blum, J. & Schräpler, R., Structure and Mechanical Properties of High-Porosity Macroscopic Agglomerates Formed by Random Ballistic Deposition, Phys. Rev. Lett. 2004, 93, 115503
14. Bonanno, A., Schlattl, H., & Paterno, L., The age of the Sun and the relativistic corrections in the EOS, Astron. and Astrophys. 2002, 390, 1115
15. Boss, A. P., Formation of Gas and Ice Giant Planets, EPSL 2002, 202, 513
16. Cancelliere, A., et al., The Permeability of a Random Medium: Comparison of Simulation with Theory, Phys. Fluids A 1990, 2, 2085
17. Colwell, J. E., Low Velocity Impacts into Dust: Results from the COLLIDE-2 Microgravity Experiment, Icarus 2003, 164, 188
18. Crowe, C., Sommerfeld, M., & Tsuji, Y., Multiphase Flows with Droplets and Particles, CRC Press, Boca Raton, 1998
19. Da Silva, R. et al., Elodie Metallicity-biased Search for Transiting Hot Jupeters. II. Two Hot Jupiters Orbiting the Slightly Evolved Stars HD118203 and HD149143, Astron. & Astrophys. 2005, 446, 717
20. Dominik, C., & Tielens, A. G. G. M., The Physics of Dust Coagulation and the Structure of Dust Aggregates in Space, ApJ 1997, 480, 647
21. Dominik, C. et al., Growth of Dust as the Initial Step Toward Planet Formation, Protostars and Planets V, 2006, in press
22. Extrasolar Planets Encyclopaedia, www.exoplanet.eu
23. FEMLAB 3.0 Release Notes, © Copyright 1994 – 2004 by COMSOL AB

24. Garaud, P., & Lin, D. N. C., On the Evolution and Stability of a Protoplanetary Disk Dust Layer, ApJ 2004, 608, 1050

25. Goldreich, P. & Ward, W. R., The Formation of Planetesimals, ApJ 1973, 183, 1051

26. Greeley, R., Leach, R., White B., Iversen, J., & Pollack, J., Threshold Windspeeds for Sand on Mars – Wind Tunnel Simulations, Geophys. Res. Lett. 1980, 7, 121

27. Grün, E., et al., Development of a Dust Mantle on the Surface of an Insolated Ice-Dust Mixture – Results from the KOSI-9 Experiment, J. Geophys. Res. 1993, 98, 15091

28. Haisch, K., Lada, E.A., & Lada, C.J., Disk Frequencies and Lifetimes in Young Clusters, ApJ 2001, 553, 153

29. Hayashi, C., Nakazawa, K., & Nakagawa, Y., Formation of the Solar System, Protostars and Planets II, Univ. of Arizona Press, Tuscon, 1993, 1100

30. Heim, L., Blum, J., Preuss, M., & Butt, H., Adhesion and Friction Forces between Spherical Micrometer-Sized Particles, Phys. Rev. Lett. 1999, 83, 3328

31. Hood, L. L., Thermal Processing of Chondrule and CAI Precursors in Planetesimal Bow Shocks, Meteoritics Planet. Sci. 1998, 33, 97

32. Hutchins, D. K., Harper, M. H., & Felder, R. L., Slip Correction Measurements for Solid Spherical Particles by Modulated Dynamic Light Scattering, Aerosol Sci. Technology 1995, 22, 202

33. Kempf, S., Pfalzner, S., & Henning, T., N-Particle-Simulations of Dust Growth: Growth Driven by Brownian Motion, Icarus 1999, 141, 388

34. Kerridge, J. F., & Chang, S., Survival of Interstellar Matter in Meteorites: Evidence from Carbonaceous Material, Protostars and Planets II, Univ. of Arizona Press, Tuscon, 1993, 738

35. Kerridge, J. F., What Can Meteorites Tell Us about Nebular Conditions and Processes during Planetesimal Accretion?, Icarus 1993, 106, 135

36. Klahr, H. H., & Bodenheimer, P., Turbulence in Accretion Disks: Vorticity Generation and Angular Momentum Transport via the Global Baroclinic Instability, ApJ 2003, 582, 869

37. Klinkenberg, L. J., The Permeability of Porous Media to Liquids and Gases, Am. Petrol. Inst. Drilling Prod. Pr. 1941, 200

38. Kokubo, E. & Ida, S., On Runaway Growth of Planetesimals, Icarus 1996, 123, 180

39. Kokubo, E. & Ida, S., Formation of Protoplanet Systems and Diversity of Planetary Systems, ApJ 2002, 581, 666

40. Koponen, A., Kataja, M., & Timonen, J., Permeability and Effective Porosity of Porous Media, Phys. Rev. E 1997, 56, 3319

41. Kouchi, A. et al., Rapid Growth of Asteroids Owing to Very Sticky Interstellar Organic Grains, ApJ 2002, 566, 121

42. Krause, M. & Blum, J., Growth and Form of Planetary Seedlings: Results from a Sounding Rocket Microgravity Aggregation Experiment, Phys. Rew. Lett. 2004, 93, 021103

43. Lee, D-C. et al., Age and Origin of the Moon, Science 1997, 278, 5340

44. Lissauer, J. J., Planet Formation, Annu. Rev. Astron. Astrophys. 1993, 31, 129

45. Lugmair, G. W., & Shukolyukov, A., Early Solar System Timescales According to ^{53}Mn-^{53}Cr Systematics, Geochim. Cosmochim. Acta 1998, 62, 2863

46. Mayor, M., & Queloz, D., A Jupiter-Mass Companion to a Solar-Type Star, Nature 1995, 378, 355

47. Mayer, L. et al., Formation of Giant Planets by Fragmentation of Protoplanetary

Disks, Science 2002, 298, 1756

48. Meakin, P., Fractal Aggregates in Geophysics, Rev. Geophysics 1991, 29, 317
49. Murray, C. D., & Dermott, S. F., Solar System Dynamics, Cambridge Univ. Press, Cambridge, 1999
50. Papaloizou, J. C. B., & Terquem, C., Critical Protoplanetary Core Masses in Protoplanetary Disks and the Formation of Short-Period Giant Planets, ApJ 1999, 521, 823
51. Paraskov, G. B., Wurm, G., Krauss, O., Eolian Erosion of Dusty Bodies in Protoplanetary Disks, ApJ 2006, 648, 1219
52. Paszun, D. & Dominik, C., The Influence of Grain Rotation on the Structure of Dust Aggregates, Icarus 2006, 182, 274
53. Pepe, F. et al., The CORALIE Survey for Southern Extra-solar Planets VII. Two Short-period Saturnian Companions to HD108147 and HD168746, Astron. & Astrophys. 2002, 388, 632
54. Poppe, T., Blum, J., Henning, T., Analogous Experiments on the Stickness of Micron-sized Preplanetary Dust, ApJ 2000, 533, 454
55. Sablotny, R., Über den Einfluß der Koagulation von Staubteilchen auf die Chemie in kalten Molekülwolken, PhD thesis, Friedrich-Schiller-University Jena, 1996
56. Sekiya, M., & Takeda, H., Were Planetesimals Formed by Dust Accretion in the Solar Nebula?, Earth Planets Space 2003, 55, 263
57. Sekiya, M., & Takeda, H., Does the Gas Flow through a Porous Dust Aggregate Help its Growth in a Protoplanetary Disk?, Icarus 2005, 176, 220
58. Supulver, K. D. et al., The Sticking Properties of Water Frost Produced under Various Ambient Conditions, Icarus 1997, 129, 539
59. Supulver K. D., & Lin D. N. C., Formation of Icy Planetesimals in a Turbulent Solar Nebula, Icarus 2000, 146, 525
60. Skorov, Y. V., et al., A Model of Heat and Mass Transfer in a Porous Cometary Nucleus Based on a Kinetic Treatment of Mass Flow, Icarus 2001, 153, 180
61. Wadhwa, M. & Russell, S. S., Timescales of Accretion and Differentiation in the Early Solar System: the Meteoritic Evidence, Protostars and Planets IV, Univ. of Arizona Press, Tucson, 2000, 995
62. Weidenschilling, S. J., Aerodynamics of Solid Bodies in the Solar Nebula, Royal Astron. Soc., Month. Notices 1977, 180, 57
63. Weidenschilling, S. J., Donn, B., Meakin, P., The Physics of Planetesimal Formation, The Formation and Evolution of Planetary Systems, Cambridge Univ. Press, Cambridge, 1989,131
64. Weidenschilling, S. J. & Cuzzi, J.N., Formation of Planetesimals in the Early Solar Nebula, Protostars and Planets III, Univ. of Arizona Press, Tucson, 1993, 1031
65. Weidenschilling, S. J., The Origin of Comets in the Solar Nebula: A Unified Model, Icarus 1997, 127, 290
66. Weidenschilling, S. J., Formation of Planetesimals and Accretion of the Terrestrial Planets, Space Science Reviews 2000, 92, 295
67. Wetherill, G. W. & Stewart G. R., Accumulation of a Swarm of Small Planetesimals, Icarus 1989, 77, 330
68. White, B. R., Lacchia, B. M., Greeley, R., & Leach, R. N., Aeolian Behavior of Dust in a Simulated Martian Environment, J.Geophys. Res. E 1997, 102, 25629
69. Wood, J. A., The Beginning: Swift and Violent, Space Sci. Rev. 2000, 92, 87
70. Wurm, G., & Blum, J., Experiments on Preplanetary Dust Aggregation, Icarus 1998, 132, 125

71. Wurm, G., Blum, J., & Colwell, J. E., NOTE: A New Mechanism Relevant to the Formation of Planetesimals in the Solar Nebula, Icarus 2001a, 151, 318

72. Wurm, G., Blum, J., & Colwell, J.E., Aerodynamical Sticking of Dust Aggregates, Phys. Rev. 2001b, E64, 046301

73. Wurm, G., The Formation of Terrestrial Planets, Proceeding of the Conference on Towards Other Earths: DARWIN/TPF and the Search for Extrasolar Terrestrial Planets 2003, 151

74. Wurm, G., Paraskov, G. B., & Krauss, O., On the Importance of Gas Flow through Porous Bodies for the Formation of Planetesimals, ApJ 2004, 606, 983

75. Wurm, G., Paraskov, G. B., & Krauss O., Ejection of Dust by Elastic Waves in Collisions between Millimeter- and Centimeter-Sized Dust Aggregates at 16.5 to 37.5 m/s Impact Velocities, Phys. Rev. 2005a, E71, 021304

76. Wurm, G., Paraskov, G. B., & Krauss O., Growth of Planetesimals by Impacts at ~25 m/s, Icarus 2005b, 178, 253

77. Youdin, A. N. & Shu, F. H., Planetesimal Formation by Gravitational Instability, ApJ 2002, 580, 494

Table 1

Impact experiments with porous targets

Exp. N	Mass before (g)	Mass after (g)	Target mass (g)	Porosity (%)	Projectile mass (g)	Mass gain (g)	Mass gain (%)	(-) Error (%)	(+) Error (%)	Pressure (mbar)	Vimp (m/s)	Comment
1	229,534	229,892	36,235	84,11	0,35	0,358	100	-2,79	0,00	0,0045	n.a.	Porous
2	237,947	238,189	44,648	80,42	0,363	0,242	n.a.	-4,13	n.a.	0,0008	n.a.	Porous
3	228,094	228,395	34,795	84,74	0,295	0,299	100	-3,34	0,00	0,0061	n.a.	Porous
4	233,752	234,023	40,453	82,26	0,306	0,275	89,87	-3,64	10,13	0,0022	n.a.	Porous
5	229,732	229,952	36,433	84,02	0,247	0,22	89,07	-4,55	10,93	0,0035	n.a.	Porous
6	230,864	231,043	37,565	83,53	0,2	0,179	89,5	-5,59	10,50	0,0012	n.a.	Porous
7	230,588	230,93	37,289	83,64	0,336	0,348	100	-2,87	0,00	0,0118	n.a.	Porous
8	230,911	231,201	37,612	83,50	0,303	0,29	95,7	-3,45	4,30	0,011	n.a.	Porous
9	232,959	233,163	39,66	82,60	0,255	0,204	80	-4,90	9,90	0,012	23	Porous
10	236,022	236,353	42,723	81,26	0,331	0,331	100	-3,02	0,00	0,0088	24	Porous
11	239,063	239,255	45,764	79,93	0,216	0,192	88,88	-5,21	10,21	0,0007	22	Porous
12	235,877	236,079	42,578	81,33	0,233	0,202	86,69	-4,95	9,95	0,0009	25	Porous
14	237,022	237,289	45,636	79,98	0,353	0,267	79,62	-3,75	8,75	0,0091	22	Porous
15	243,173	243,524	51,787	77,29	0,387	0,351	90,69	-2,85	9,31	0,0009	n.a.	Porous
16	232,467	232,85	41,103	81,97	0,399	0,361	90,48	-4,99	9,52	0,0015	25,7	Porous
18	237,242	237,47	42,03	81,56	0,151	0,228	n.a.	-5,00	n.a.	0,0006	16,8	Porous
20	252,209	252,811	56,997	75,00	0,576	0,602	100	-5,00	0,00	0,0011	25,2	Porous
21	250,985	251,41	55,773	75,54	0,55	0,425	81,34	-2,35	7,35	< 0,0001	26	Porous
22	172,82	173,552	46,984	83,47	0,749	0,732	99,72	-0,68	0,28	0,0009	16,5	Porous
23	183,992	184,388	58,289	79,49	0,394	0,396	100	-5,00	0,00	0,001	37,4	Porous
24	178,146	178,549	52,31	81,59	0,41	0,403	98,29	-6,24	1,71	0,0019	36,1	Porous
25	199,52	199,78	73,817	74,02	0,38	0,26	68,42	-1,92	6,92	0,0014	30,6	Porous
32	187,038	187,27	61,202	78,47	0,301	0,232	78,65	-2,15	7,15	0,0028	33	Porous
33	180,28	180,385	54,577	80,79	0,125	0,105	84	-4,76	9,76	n.a.	26,8	Porous
34	178,101	178,19	52,265	81,60	0,104	0,089	85,58	-5,62	10,62	0,008	25,1	Porous

Exp. N.	Mass before	Mass after	Target mass	Porosity	Projectile mass	Mass gain	Error	Pressure	Vimp	Mass gain 2		
35	175,501	175,707	49,798	82,48	0,269	0,206	85,08	-2,43	7,43	0,018	22	WKP 27Hz (P)
36	199,45	199,574	73,614	74,09	0,163	0,124	84,53	-4,03	9,03	0,0137	25	Porous
37	200,93	201,086	75,227	73,52	0,199	0,156	80	-3,21	8,21	0,0031	21,6	Porous
38	171,813	171,97	45,977	83,82	0,153	0,157	100	-3,18	0,00	0,0018	24,5	Porous
39	206,957	207,222	81,254	71,41	0,275	0,265	98,33	-1,89	1,67	0,0018	25,5	Porous
40	207,002	206,986	81,166	71,43	0,186	-0,016	-9,05	-31,25	36,25	0,71	27,5	WKP 27Hz (P)
41	175,685	175,829	49,982	82,41	0,146	0,144	98,63	-3,47	1,37	0,019	n.a.	Porous
42	171,829	172,048	45,966	83,82	0,245	0,219	89,39	-2,28	7,28	0,0018	24,6	Porous
43	199,03	199,305	73,327	74,19	0,337	0,275	81,6	-1,81	6,81	0,95 (+ -0,05)	24,3	WKP 35Hz (P)
44	159,483	159,614	33,647	88,16	0,131	0,131	100	-3,82	0,00	0,0048	26,2	0,09 mm
45	162,546	162,693	36,843	87,04	0,163	0,147	90,18	-3,40	8,40	0,0148	28	0,09 mm
46	159,827	159,955	33,991	88,04	0,142	0,128	90,14	-3,91	8,91	0,0164	25,9	0,09 mm
47	161,054	161,265	35,351	87,56	0,229	0,211	92,14	-2,37	7,37	0,016	28,7	0,09 mm
48	166,568	166,728	40,732	85,67	0,178	0,16	89,88	-3,13	8,13	0,0164	27,9	0,025 mm 14mm
49	168,653	168,768	42,95	84,89	0,13	0,115	88,46	-4,35	9,35	0,017	n.a.	0,025 mm 7mm
50	166,8	166,878	40,964	85,58	n.a.	0,078	n.a.	n.a.	n.a.	0,003	25	0,025 mm 10mm
51	172,265	172,319	46,403	83,58	0,065	0,054	92,3	-9,26	7,70	0,0158	n.a.	0,025 mm 10mm
52	430,866	430,946	270,572	82,01	0,138	0,08	57,97	n.a.	n.a.	0,00196	22,8	Target 120mm
53	450,321	450,428	290,304	81,63	0,217	0,107	49,31	n.a.	n.a.	< 0,0001	23,7	Target 120mm
54	172,249	172,368	46,386	83,68	0,235	0,119	50,64	n.a.	n.a.	0,0017	n.a.	0,025 mm 10mm
55	450,524	n.a.	290,507	81,61	0,065	n.a.	n.a.	n.a.	n.a.	0,0158	n.a.	Target 120mm

Legend (Tables 1 and 2)

Exp. N. – Experiment number
Mass before – Target mass (with target tray) before the impact
Mass after – Target mass (with target tray) after the impact
Target mass – Target mass (without target tray)
Porosity – Target porosity
Projectile mass – Mass of the projectile
Mass gain – Accretion efficiency (projectile mass added to the target)
Error – Measuring error
Pressure – Ambient gas pressure during the impact
Vimp – Impact velocity
Mass gain 2 – Projectile mass remained on the target surface after target tilting

Table 2

Impact experiments with compact targets

Exp. N	Mass before (g)	Mass after (g)	Target mass (g)	Porosity (%)	Projectile mass (g)	Mass gain (g)	Mass gain (%)	(-) Error (%)	(+) Error (%)	Pressure (mbar)	Vimp (m/s)	Mass Gain 2 (%)
27	217,811	217,98	92,108	67,58	0,373	0,169	46,23	-2,96	7,96	0,0016	28,3	n.a.
31	217,833	218,027	92,13	67,57	0,369	0,194	52,57	-2,58	7,58	0,0044	n.a.	n.a.
56	221,264	221,388	95,428	66,42	0,211	0,124	58,77	-4,03	9,03	0,0033	n.a.	n.a.
57	228,965	229,058	103,979	63,41	0,13	0,093	71,54	-5,38	10,38	0,0036	24,2	66,15
58	221,3	221,403	95,464	66,4	0,139	0,103	74,1	-4,85	9,85	0,0027	21,7	69,06
59	228,864	228,975	103,878	63,44	0,202	0,111	54,95	-4,50	9,50	0,0046	23,6	50
60	221,323	221,411	95,487	66,39	0,278	0,088	31,65 ?	-5,68	10,68	0,001	n.a.	n.a.
61	226,327	226,334	101,341	64,34	0,153	0,007	4,57 ?	-71,43	76,43	0,0058	n.a.	n.a.
68	224,246	224,393	99,26	65,07	0,25	0,147	58,8	-3,40	8,40	0,0117	22,5	n.a.
69	221,221	221,338	95,358	66,44	0,209	0,117	55,98	-4,27	9,27	0,0117	20	33,01
70	224,199	224,296	99,213	65,08	0,185	0,097	52,43	-5,15	10,15	0,0177	23,2	35,66
71	221,025	221,183	95,189	66,5	0,224	0,158	70,54	-3,16	8,16	0,0169	n.a.	56,70
72	221,074	221,137	95,238	66,48	0,125	0,063	50,4	-7,94	12,94	0,014	n.a.	16,8
73	224,108	224,233	99,122	65,12	0,167	0,125	76,38	-4,00	9,00	0,0136	18,4	49,5
74	220,765	220,928	94,929	66,59	0,236	0,163	69,07	-3,07	8,07	0,0159	18,2	63,56
75	224,095	224,225	99,109	65,12	0,189	0,13	68,78	-3,85	8,85	0,0102	14,5	59,26
76	220,632	220,774	94,796	66,64	0,216	0,142	65,74	-3,52	8,52	0,0141	19,7	53,7
77	224,145	224,262	99,154	65,11	0,201	0,117	58,21	-4,27	9,27	0,0153	16,6	44,28
78	221,297	221,413	95,461	66,41	0,226	0,116	51,33	-4,31	9,31	0,0137	16,2	35,4
79	224,127	224,273	99,141	65,11	0,218	0,146	66,97	-3,42	8,42	0,018	13,5	60,09
80	220,11	220,21	94,274	66,82	0,187	0,1	53,48	-5,00	10,00	0,0149	7,9	25,67
81	220,031	220,108	94,195	66,85	0,172	0,077	44,77	-6,49	11,49	0,0074	12,9-15,2	12,79
82	224,351	224,402	99,365	65,03	0,209	0,051	24,4	-9,80	14,80	0,0088	10,8	5,74
83	219,887	220,083	94,051	66,9	0,234	0,196	83,76	-2,55	7,55	0,0111	12,7	81,62(5,55)
84	224,433	224,563	99,447	65	0,249	0,13	52,21	-3,85	8,85	0,0049	11,1	15,26
85	219,893	219,945	94,057	66,9	0,221	0,052	23,53	-9,62	14,62	0,0084	8,9	-23,08
86	224,271	224,433	99,285	65,06	0,221	0,162	73,3	-3,09	8,09	0,0134	6,1	10,41

Table 3

Wind tunnel experiments

Exp. №	Target	Run	Erosion threshold (mbar)	Pump (Hz)	Pressure (mbar)	Erosion rate (gr)	Erosion rate (gr/h)	Time (min)	Comment
502	Hemisphere (G)	First run	0,1	35	*	*	*	*	*
	Hemisphere (G)	Rerun	0,13	35	*	*	*	*	*
503	Hemisphere	First run	> 1	35	*	*	*	*	*
	Hemisphere	Rerun	> 1	35	*	*	*	*	*
504	Pile	First run	0,46	35	*	*	*	*	*
	Pile	Rerun	0,8	35	*	*	*	*	*
505	Pile	First run	0,5	35	*	*	*	*	*
	Pile	Rerun	0,94	35	*	*	*	*	*
	Pile	Rerun (2)	0,8	40	*	*	*	*	*
	Pile	Rerun (3)	> 1,1	30	*	*	*	*	*
506	Pile	First run	0,27	40	*	*	*	*	*
	Pile	Rerun	0,32	35	*	*	*	*	*
	Pile	Rerun (2)	0,58	30	*	*	*	*	*
507	Hemisphere	First run	> 2	40	*	*	*	*	*
508	Hemisphere	First run	> 4,5	35	*	*	*	*	*
509	Hemisphere (G)	First run	0,22	35	*	*	*	*	*
	Hemisphere (G)	Rerun	0,7	35	*	*	*	*	*
	Hemisphere (G)	Rerun (2)	0,46	40	*	*	*	*	*
510	Pile	First run	0,5	40	*	*	*	*	*
	Pile	Rerun	0,9	35	*	*	*	*	*
	Pile	Rerun (2)	1,22	30	*	*	*	*	*
511	Pile	First run	0,5	35	0,56-0,59	0	0	60	*
512	Pile	First run	0,46	35	0,8-0,9	0,011	0,01	90	*
513	Pile	First run	0,6	35	1,1	0,022	0,025	45	*
514	Hemisphere (G)	First run	< 0,005	35	*	*	*	*	*
	Hemisphere (G)	Rerun	0,46	35	*	*	*	*	*
515	Hemisphere (G)	First run	0,5	35	*	*	*	*	*
	Hemisphere (G)	Rerun	0,3	40	*	*	*	*	*

	Hemisphere (G)	Rerun (2)	1,48	30	*	*	*	*	*
516	Hemisphere	First run	4,4	35	*	*	*	*	*
517	Pile	First run	0,38	35	1,1	0,052	0,058	45	*
518	Hemisphere (G)	First run	0,42	35	*	*	*	*	*
	Hemisphere (G)	Rerun	0,3	35	*	*	*	*	*
519	Pile	First run	n.a.	35	0,9-1	0,022	0,022	60	*
520	Pile	First run	n.a.	35	0,95-1,1	0,035	0,034	65	*
521	Pile	Target 519	n.a.	35	1,25-1,35	0,006	0,006	60	*
522	Pile	Target 520	1	35	unsuccessful	unsuccessful	unsuccessful	120	*
523	Pile	First run	*	35	1-1,1	0,036	0,031	90	*
524	Pile	First run	*	35	0,5-0,6	0,004	0,004	60	*
525	Pile	First run	*	35	0,7-0,8	0,038	0,038	60	*
526	Pile	First run	*	35	unsuccessful	unsuccessful	unsuccessful	60	*
527	Plane	First run	*	35	1,05-1,2	0	0	20	160 µm
528	Plane	First run	*	35	1,05-1,2	0,007	0,011	20	*
529	Pile	First run	*	35	0,65	0,005	0,007	30	*
530	Pile	First run	*	35	0,6-0,65	0,01	0,01	60	160 µm
531	Pile	First run	*	35	0,43-0,46	0,005	0,005	60	*
532	Pile	First run	0,31	40	0,63-0,66	0,023	0,031	30	*
533	Pile	First run	*	35	0,53-0,56	0,007	0,007	60	160 µm
534	Pile	First run	*	35	1,03-1,06	0,007	0,007	60	160 µm
535	Pile	First run	*	35	< 0,1	0,018	*	*	T1
536	Pile	First run	*	40	0,63-0,65	0,019	0,019	60	*
537	Pile	First run	*	35	< 0,1	0,01	*	*	T2
537a	No dust	*	*	35	< 0,1	0	*	*	T2
538	Pile	First run	*	35	< 0,1	0	*	*	T3
539	Pile	First run	*	35	0,33-0,37	0,011	0,011	60	*
540	Pile	First run	*	35	< 0,1	0,012	*	*	T2
541	Pile	First run	*	35	1,4	0,029	0,039	30	*
542	Pile	First run	*	35	1,4	0,015	0,015	60	*
543	Pile	First run	*	40	0,48-0,52	0,009	0,012	30	*
544	Pile	First run	*	35	0,43-0,46	0,022	0,03	30	160 µm
544a	Pile	Rerun	*	35	0,43-0,46	0,008	*	30	160 µm
545	Pile	First run	*	35	0,98-1,02	0,022	0,022	60	160 µm
548	Pile	First run	*	35	2	0,149	0,149	60	*

Exp. N.	Target	Run	Erosion threshold	Pump	Pressure	Erosion rate		Time	
549	Pile	First run	*	35	3	0,312	0,312	60	*
550	Pile	First run	*	35	4	0,687	0,687	60	*
551	Cuboid (C)	First run	*	35	2	0,006	0,008	30	*
552	Cuboid	First run	*	35	2	0,019	0,025	30	*
553	Cuboid	First run	*	35	3	0,066	0,088	30	*
554	Cuboid	First run	*	35	4	0,247	0,329	30	*
555	Cuboid	First run	*	35	3,5	0,178	0,237	30	*
556	Cuboid	First run	*	35	2,5	0,086	0,114	30	*
557	Cuboid	First run	*	35	3	0,071	0,094	30	*
558	Cuboid	First run	*	35	3	0,073	0,097	30	*
558a	Cuboid	Rerun	*	35	3	0,024	*	30	*
558b	Cuboid	Rerun	*	35	3	0,012	*	30	*

Legend (Table 3)

Exp. N. – Exreriment number
Target – Target shape
Run – Run number (first run – new target, rerun – used target)
Erosion threshold – The gas pressure at which the dust target begins to be eroded
Pump – Pump operating frequency
Pressure – Ambient gas pressure during the experiment
Erosion rate – The dust mass eroded in a determined time
Time – Experiment duration

DANKSAGUNG

LEBENSLAUF

Name:		Georgi Bozhidarov Paraskov
Geburtsdatum:	**06.09.1978**	in Sliven, Bulgarien
Schulbildung:	**1985 – 1992**	Grundschule in Sliven, Bulgarien
	1992 – 1996	Gymnasium für Naturwissenschaften und Mathematik Sliven, Bulgarien *Hauptfach:* Physik und Mathematik
	1996	Abschluss mit Abitur
Studium:	**1996 – 2001**	Universität für Bergbau und Geologie Sofia, Bulgarien *Fach:* Geologie und Lagerstättenforschung
	2001	Abschluss mit Diplom
Promotionsstudiengang:	**2002 – heute**	Doktorand an der Westfälische Wilhelms-Universität Münster *Fach:* Planetologie
Tätigkeiten:	**2002 – 2003**	Wissenschaftliche Hilfskraft am Institut für Planetologie Münster
	2003 – heute	Wissenschaftlicher Mitarbeiter am Institut für Planetologie Münster

Münster, 24.07.2006